MUONIUM DIFFUSION IN ICE

by

Siu-keung Leung

B.Sc., Simon Fraser University, 1982

THESIS SUBMITTED IN PARTIAL FULFILLMENT OF

THE REQUIREMENTS FOR THE DEGREE OF

MASTER OF SCIENCE

in the Department

of

Chemistry

SIMON FRASER UNIVERSITY

August, 1985

APPROVAL

Name: Siu-keung Leung

Degree: Master of science

Title of thesis: Muonium Diffusion in Ice

Examining Committee:

Chairperson: T. N. Bell, Professor

Senior Supervisor: P. W. Percival, Associate Professor

E. J. Wells, Associate Professor

K. E. Newman, Assistant Professor

Internal Examiner: G. L. Malli, Professor

Date Approved: 1st August 1985

PARTIAL COPYRIGHT LICENSE

I hereby grant to Simon Fraser University the right to lend my thesis, project or extended essay (the title of which is shown below) to users of the Simon Fraser University Library, and to make partial or single copies only for such users or in response to a request from the library of any other university, or other educational institution, on its own behalf or for one of its users. I further agree that permission for multiple copying of this work for scholarly purposes may be granted by me or the Dean of Graduate Studies. It is understood that copying or publication of this work for financial gain shall not be allowed without my written permission.

Title of Thesis/Project/Extended Essay

"Muonium Diffusion in Ice"

Author: _____
(signature)

Siu-keung Leung
(name)

Aug. 5/85
(date)

ABSTRACT

Muonium (μ^+e^-) is generally regarded as a light isotope of hydrogen. It has been detected in single crystals of ice from 8 K to 263 K using the muon spin rotation (μSR) technique at TRIUMF. Hydrogen atoms have never been observed in ice for much of this temperature range. Transverse spin relaxation rates of muonium in single crystals of H_2O- and D_2O-ices have been measured over a wide temperature range. The dominant relaxation mechanism is shown to be modulation of the dipolar interaction between muonium and the lattice nuclei by diffusion of muonium through the lattice. Contrary to previous findings, muonium is found to be diffusing at temperatures as low as 8 K.

A classical model has been used to represent the intermolecular interactions between muonium and the lattice. Calculations show that muonium preferentially diffuses along channels parallel to the *c*-axis. The potential energy function for motion along such a channel gives an activation energy of $\simeq$ 35 meV. An activation energy of 40 $\pm$ 4 meV is obtained by fitting the experimental relaxation rates above 128 K to an Arrhenius expression. Curvature of the Arrhenius plot at lower temperatures can be explained by tunnelling, in accord with the theoretical prediction that the tunnelling rate exceeds activated diffusion at temperatures below 100 K.

ACKNOWLEDGMENTS

I am very much indebted to Professor Paul W. Percival, my senior supervisor, for his endless patience and guidance which have been a source of encouragement and inspiration throughout the course of the research. The author would also like to express gratitude to Professor Kenneth E. Newman for his numerous interesting and helpful suggestions in the theory of magnetic resonance and relaxation phenomena. Doctor Jean-Claude Brodovitch is thanked for his ingenious knack in designing special apparatus. I am also grateful to Professor E. J. Wells for helpful discussions.

Miss Julie Bartlett is thanked for her assistance in some of the calculations. Mr. Kevin Brown is acknowledged for his "presence" during some of the beam periods.

I would like to thank everyone in the SFU nuclear suite for creating an enthusiastic atmosphere for scientific research with their **"LOUD"** (≥ **120 dB**) rock 'n' roll music . Thanks go to all the helping hands of beam line M20 in **TRIUMF**. Without their expertise, the experiments would not have been done as easily as they have been.

Very special thanks go to Bosco, my brother; and Manny, my sister; for supporting me financially as well as spiritually. Last but not least, I will not forget all the interesting conversations that Brent, my brother-in-law, and I had over coffee.

To my Mother

"The ice was here, the ice was there,

The ice was all around:

It cracked and growled, and roared, and howled,

Like noises in a swound!"

-Samuel Taylor Coleridge 1772-1834,

in "Ancient Mariner" stanza 15.

TABLE OF CONTENTS

LIST OF TABLES

LIST OF FIGURES

I. Introduction

1. General background

In 1954, Livingston *et al* [1] reported the detection of trapped hydrogen atoms, formed by gamma irradiation, in acidic ices at 77 K. It was further reported by Piette *et al* [2] in 1959 that H atoms, also formed by γ-irradiation, are stably trapped in pure ice at 4.2 K. Fluornoy *et al* [3] discovered that these trapped H atoms disappear rapidly around 50 K. It was deduced that this thermal decay is caused by diffusion of the H atoms through the lattice. Subsequent studies on the thermal decay of these H atoms were mainly concerned with the deviation of decay kinetics from simple rate laws.

Thus, despite its fundamental importance, little was known about the diffusional process and the chemical reactions of trapped H atoms until Shiraishi *et al* [4] published their report in 1976. They investigated the electron spin resonance (ESR) spectra of trapped H atoms, formed by continuous electron irradiation, in neutral and acidic ices from 160 K up to the melting point. They utilized motional line narrowing and chemically induced electron polarization (CIDEP) [5,6] effects to enhance the ESR signal intensities. In the range of approximately 50 K to 160 K, it has not been possible to detect

H atoms in pure ice by conventional ESR methods.

However, it is a relatively simple procedure to observe muonium [7] in ice using the Muon Spin Rotation (μSR) [8] technique. Muonium, μ^+e^-, is an exotic atom. It is formed by stopping high energy muons in matter. μSR is the experimental technique employed to observe the muon spin precession and the rate its spin depolarizes (relaxes) in matter. Muonium has long been regarded as a light isotope of hydrogen. Since the ionization potential and Bohr radius of muonium are very close to those of hydrogen, it is expected to behave similarly to hydrogen. Therefore, it is not unreasonable to study muonium in ice in place of hydrogen in view of the difficulties encountered as stated previously. The behaviour of hydrogen atoms in ice can then be inferred from muonium results.

Ice was one of the first condensed substances in which muonium was directly observed by means of its triplet precession signal in low transverse field [57]. In 1973, Gurevich *et al* [9] reported measurements of the relaxation rates of muonium in H_2O- and D_2O-ices at 77 K. Discrepancy between the relaxation rates predicted by dipolar interactions and experimental results led them to conclude that muonium does not diffuse in ice at that temperature. In 1978, Percival *et al* [10] presented a study of muonium in ice over a range of temperatures. Their results indicated in addition to dipolar broadening there was another relaxation mechanism which was of unknown origin. Recently, Percival *et al* [11] reported a study of muonium in single

crystals of ice. The relaxation rates they obtained were less than those for polycrystalline ice as reported in [10]. They also observed a splitting at low field where Zeeman splitting is insignificant. This splitting was shown to be isotope and temperature independent but dependent on the orientation of the crystal with the applied field. In single crystals of quartz, the same phenomenon had been observed by Brewer *et al* [12,13,14]. The origin of the splitting has been attributed to an anisotropy in the hyperfine tensor of the spin Hamiltonian of muonium in quartz.

The most common crystalline form of ice is ice **Ih**. In ice **Ih**, the oxygen nuclei are set in a tetrahedral environment. A hydrogen nucleus is situated between each pair of oxygen nuclei. The crystal is said to have a wurtzite structure with the oxygen nuclei arranged in a hexagonal close packed manner. The crystal structure of ice **Ih** has a very striking semblance to that of quartz - they both have hexagonal channels parallel to the *c*-axis of the crystal. According to Brewer *et al*, muonium diffuses along these channels in quartz.

In analogy to the results obtained by Brewer *et al*, Percival *et al* [11] concluded that the hyperfine tensor of muonium in ice **Ih** is also anisotropic. The spectra of muonium in polycrystalline ice are inhomogeneously broadened because of this anisotropy. The relaxation rates obtained for muonium in polycrystalline ice will be characteristic of the powder line width. This explains the discrepancy of experimental results

with theoretical predictions cited by Gurevich *et al*. Hence, it seems imperative to undertake a study of muonium in single crystals of ice **Ih** in order to characterize its relaxation behavior and from that, the diffusion parameters.

In order to characterize the diffusion of a hydrogen atom in ice, it is necessary to determine the potential energy experienced by the hydrogen atom as a function of its location along the diffusion path. This in turn involves the calculation of the total intermolecular energy between the hydrogen atom and the lattice nuclei. Eisenberg and Kauzmann [16] have presented a set of Buckingham potential functions describing the interatomic interactions between two water molecules. Benderskii *et al* [17], approximated the potential energy of a hydrogen atom diffusing in ice through the channel parallel to the *c*-axis of the crystal by treating the water molecules in the lattice as single entities. They combined the oxygen-hydrogen potential function as given by Eisenberg and Kauzmann and the results from *ab initio* calculations obtained for the reaction:

$$H\cdot + H_2O \rightarrow H_3O\cdot \qquad (1.1)$$

as calculated by Niblaeus *et al* [18]. The *ab initio* calculations were made to estimate the stability of the radical $H_3O\cdot$. However, the assumption taken by Benderskii *et al* that the interactions between the diffusing hydrogen atom and the lattice nulcei can be approximated by treating the water molecules as

single entities is debatable.

As the hydrogen atom is diffusing through the channel, it is always closer to the hydrogen nuclei in the lattice than to the oxygen nuclei because of the lattice geometry. The *ab initio* calculations of Nibleaus *et al* were made for the hydrogen atom approaching the water molecule along a line bisecting the H-O-H angle, *i.e.*, the hydrogen atom is farther away from the hydrogen nuclei than the oxygen nucleus of the water molecule. The intermolecular force is either r^{-6} or exp(-r) dependent, depending on the distance separating the two molecules in question. It is questionable whether the procedure taken by Benderskii *et al* to describe the potential of a hydrogen atom in an ice lattice is correct. Hence, it seems quite important to undertake an investigation of the potential energy experienced by the hydrogen atom as it diffuses through the channel to clear up the question.

2. Aims of this research

Gurevich *et al* [9] proposed that muonium does not diffuse in ice at 77 K. On the other hand, Percival *et al* [11] pointed out that the hyperfine tensor of the spin Hamiltonian for muonium in ice is anisotropic and the relaxation rate of muonium in polycrystalline ice is characteristic of the powder line width. This explained the discrepancy between experimental results and theoretical predictions cited by Gurevich *et al*.

However, the question regarding the mobility of muonium in pure ice at 77 K still remains.

It is the purpose of the present research to investigate the mobility of muonium in single ice crystals as a function of temperature. It involves both theoretical modelling and experimental work. Experimentally, the relaxation rates of muonium in single crystals of H_2O- and D_2O-ices are measured using conventional μSR methods. From the experimental results, the mobility of muonium in ice can be inferred. Theoretical modelling involves the estimation of the intermolecular potential between the muonium and the lattice nuclei. From this potential, both the thermally activated and the quantum tunnelling diffusion rates are calculated. Results from these calculations are compared to the experimentally obtained data.

Hopefully, the question of the mobility of muonium in ice can be answered by this investigation. In addition, it is hoped that the doubt about the intermolecular potential experienced by the diffusing muonium can be cleared up.

II. Crystal structure of Ice Ih

1. Geometrical arrangements of the oxygen nuclei

The geometrical arrangement of oxygen nuclei in crystalline ice **Ih** can be determined from analyses of the x-ray diffraction pattern of the solid. Early studies of ice **Ih** by x-ray diffraction were made by Rinne, St.John, and Dennison [19,20,21]. From these results, Bragg [22] deduced that each oxygen nucleus in ice **Ih** is situated in a tetrahedral environment and is approximately at the center of mass of its four neighbouring oxygen nuclei. The arrangement of the oxygen nuclei is shown in Figure II.1 [23]. The tetrahedral co-ordination of the oxygen nuclei gives rise to a crystal structure possessing hexagonal symmetry. The crystal is said to have a wurtzite structure with the oxygen nuclei arranged in a hexagonal close packed (**HCP**) lattice with successive layers arranged in a sequence of **AABBAABB**...*etc.* The layers of oxygen nuclei are called the "basal planes" of the lattice where all the molecules are concentrated. The normal to these basal planes is referred to as the *c*-axis of the crystal and can be seen in Figure II.1. This wide open structure of the crystal explains the lower density of ice when compared to liquid water. Of most relevance to the present research is the existence of channels

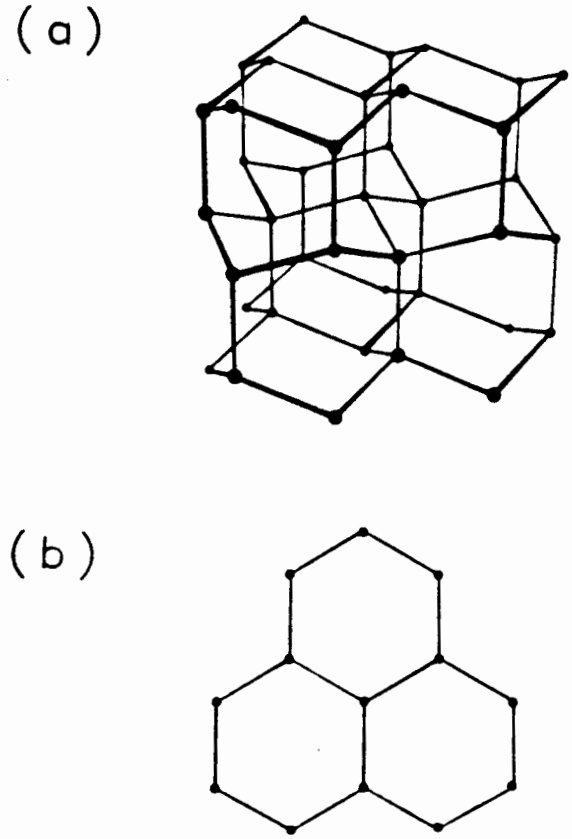

Figure II.1. The arrangement of oxygen atoms in ice Ih:
(a) view perpendicular to the *c*-axis.
(b) view along the *c*-axis.

parallel to the *c*-axis which will serve as the diffusion channel for muonium/hydrogen atom.

The unit cell is the fundamental building block of the crystalline structure of ice **Ih**. The complete crystallographic structure can be constructed by stacking identical unit cells face to face in perfect alignment in three dimensions. The total number of oxygen nuclei in a unit cell is four with the tetrahedral angle at 109°28'. The various symmetry elements exhibited by the complete lattice of oxygen nuclei in ice **Ih** are represented by the Hermann Mauguin space group symbol $P6_3/mmc$.[1]

Finally, it should be noted that the molecular structure of ice **Ih** is centrosymmetric, *i.e.*, a point can always be located within the lattice such that every molecule which occurs at a distance from this point in one direction has a corresponding molecule at the same distance from the point in the opposite direction. This characteristic has been utilized in simplifying computer programs.

---

[1] Most crystals of ice **Ih** show hexagonal morphology appropriate to this space group. Some rare crystals showing trigonal (*3/mm*) or polar hexagonal (*6mm*) symmetry have been observed [24]. These crystals suggested structures of symmetry lower than $P6_3/mmc$. However, such structures have not been observed in x-ray diffraction studies of ice **Ih**.

2. Positions of the hydrogen nuclei

Because of the empirical chemical formula of ice (H_2O), each oxygen nucleus must have two hydrogen nuclei associated with it. Since there are four other oxygen nuclei surrounding each oxygen nucleus, there is one hydrogen nucleus situated between each pair of oxygen nuclei. The question is how are these hydrogen nuclei distributed in the structure. The positions of these hydrogen nuclei are hard to determine by studying the x-ray diffraction pattern of the solid because the intensity of the x-rays scattered by the oxygen nuclei is about eight times greater than that scattered by the hydrogen nuclei. It was not until in the late 40's that attempts were made to establish the exact location of the hydrogen nucleus between two oxygen nuclei. One of the earliest speculative models puts the hydrogen atom in exactly the middle of the line separating the two oxygen nuclei [25]. However, this idea was displaced by the proposal of "Bernal-Fowler rules" [26]. The Bernal-Fowler rules are formulated under a statistical model, and an ice crystal which obeys these rules is termed an ideal crystal:

1. Each oxygen nucleus has two hydrogen nuclei attached to it at distances of about 0.95 Å, thereby forming a water molecule.
2. Each water molecule is oriented so that its two hydrogen nuclei are directed approximately towards two of the four

oxygen nuclei which surround it tetrahedrally.

3. The orientations of adjacent water molecules are such that only one hydrogen nucleus lies between each pair of oxygen nuclei.
4. Under ordinary conditions ice **Ih** can exist in any one of a large number of configurations, each corresponding to a certain distribution of the hydrogen nuclei with respect to the oxygen nuclei.

The six possible arrangements of hydrogen nuclei on the four bonds around each oxygen atom in ice **Ih** are shown in Figure II.2. According to these Bernal-Fowler rules, the structure of ice **Ih** may change from one configuration to another by the movement of a hydrogen nucleus from a potential minimum 0.95 Å from one adjacent oxygen nucleus to another one 0.95 Å from the other adjacent oxygen nucleus. In an ideal crystal, the movement of the hydrogen nuclei must be simultaneous for all six hydrogen nuclei in a basal plane. However, this would involve all the hydrogen nuclei in the crystal because of the interrelation between these planes, and seems energetically unlikely. The movements of hydrogen nuclei in the lattice is likely allowed by the existence of defects [23]. These movements are measured by the dielectric relaxation times. At 0 °C, the dielectric relaxation time of ice **Ih** was measured to be $\simeq 2 \times 10^{-5}$ sec [27]. At lower temperatures, the protons are frozen into one of a large number of configurations and the dielectric relaxation

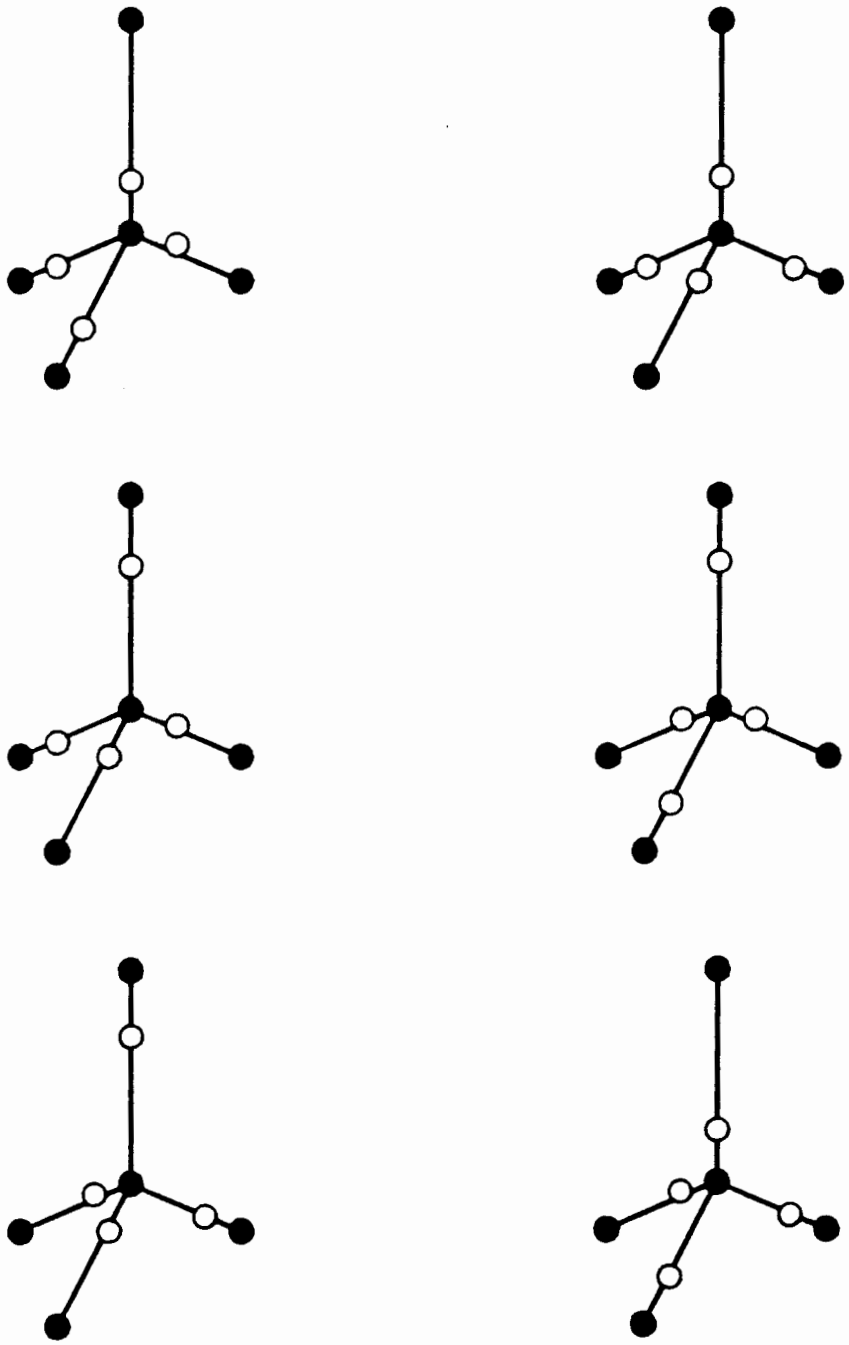

Figure II.2. The six possible arrangements of the hydrogen atoms on the four bonds around each oxygen atoms in ice Ih. ●-oxygen, o-hydrogen atoms.

time is longer. The region where this freezing-in takes place is speculated to be between 100 and 120 K from the results of determination of the heat capacity of the solid [28]. This arrangement of the hydrogen nuclei of the water molecules in the lattice implies a non-ordered distribution of the dipoles of the water molecules and allows a zero-point entropy for the solid. Experimentally, the value of the zero-point entropy was determined to be 3.41 J $mol^{-1}deg^{-1}$ [16]. The theoretical value of this zero-point entropy has been calculated by Hobbs [23] (S_0 = 3.4103 ± 0.0008 J $mol^{-1}deg^{-1}$). The movement and freezing-in of hydrogen nuclei in ice **Ih** have no direct bearing on the present research since their motional time scale is long compared to the muon life-time and the muonium relaxation time (μs regime).

Neutron diffraction has been used to determine the position of hydrogen nuclei in ice, and the space group of $P6_3/mmc$ was determined in D_2O ice **Ih** [30]. The deuterium nucleus is found to be at a distance of 1.011 Å from its nearest oxygen nucleus. The same distance has also been determined by nuclear magnetic resonance (**NMR**) techniques [31]. However, there are two schools of thought regarding the H-O-H bond angle (109.5° vs 104.5°) [23]. This difference has made the determination of the intermolecular potential of hydrogen and/or muonium in the structure quite difficult. The most recent structural study of ice **Ih** by Kuhs and Lehmann [58] using high-resolution, high-flux, and short-wavelength neutron sources supports the

former opinion. Following Kuhs and Lehmann, the positions of the hydrogen nuclei in ice **Ih** are taken to be 1.0 Å from their nearest oxygen nuclei with the H-O-H bond angle being 109.5° in all later calculations.

3. Dipole moment of the water molecule in ice Ih

The dipole moment of a water molecule is important since it causes induction forces on the trapped hydrogen atom in the lattice. The average dipole moment, μ_0, of a water molecule in ice **Ih** is not accessible to direct measurement. Its value is different from the dipole moment in the vapor phase since in ice **Ih** the electrostatic fields of the neighboring water molecules induce an additional dipole in each molecule.

The electrostatic potential produced by a charge distribution at an external point may be represented as the sum of the potentials produced by the electric moments of the charge distribution. In the case of a water molecule in an ice lattice, the most important contribution to the potential is from the dipole moment, but the higher moments should also be considered [23]. Coulson and Eisenberg [32] calculated the contributions from the dipole, (μ), quadrupole (Q), and octupole (O) moments of neighboring water molecules to the dipole moment of a water molecule in an ice lattice. They concluded that the average magnitude of the field arising from neighboring molecules is:

$$F = 1.548 \times 10^{10} \text{ V m}^{-1} \quad (2.1).$$

They also calculated the value of the dipole moment of a water molecule in ice Ih and obtained:

$$\mu_0 = 8.66 \times 10^{-30} \text{ C m} \quad (2.2).$$

This value of μ_0 is over 40 per cent greater than the value of the permanent dipole moment of an isolated water molecule. However, this is not unexpected due to the contributions from neighboring molecules [23]. This value is used for later calculations on the induction forces as caused by the dipole moments of the water molecules in the lattice on the hydrogen atom as it diffuses along the channel in the lattice.

III. Muon Spin Rotation, μSR

1. Positive muon and muonium

The positive *muon*, μ^+, is an elementary particle. It is a lepton because it decays via the weak interaction and has a spin of $\frac{1}{2}$ [8]. The μ^+ is produced by the decay of a positive pion:

$$\pi^+ \rightarrow \mu^+ + \nu_\mu \qquad (3.1).$$

In a weak interaction, the spins and angular momenta of the reactants must be conserved. Since the *neutrino* has negative helicity, the spin of the positive muon must be anti-parallel to its momentum in the pion's center-of-mass co-ordinate system [33]. Hence, a highly polarized beam of μ^+ can be produced by judiciously selecting the momenta of muons in the in-flight decay of the pions.

Muonium is an exotic atom consisting a positive muon and an electron (μ^+e^-) [7]. It is formed by stopping high energy muons in matter. It has a mass of about 106 MeV. Although muonium has only 1/9 the rest mass of a hydrogen atom, its reduced mass is within 0.5% that of hydrogen. Therefore the chemical properties of muonium are very similar to those of a hydrogen atom. A table of the properties of the muon and muonium is shown in

Table III.1. Muonium has been widely recognized as a light isotope of hydrogen [8,34]. Because of the magnitude of the mass discrepancy between muonium and protonium, the kinetic isotope effect is very readily observed [35]. The inclusion of muonium in the series of hydrogen isotopes (mass ratios 3:2:1:0.11) increases the scope of kinetic isotope studies vastly. The greatest advantage of the inclusion of muonium in the hydrogen isotope series is in the investigations of quantum tunnelling effects.

2. μSR

μSR is the experimental technique used in detecting muons and muonium [8]. Normally, it utilizes a highly polarized muon beam which can be obtained in "Meson Factories". There are three such establishments:

1. Los Alamos Meson Physics Facility (**LAMPF**),
2. Swiss Institute for Nuclear Research (**SIN**), and
3. TRI-University Meson Facility (**TRIUMF**).

Other less intense muon beams are available at **CERN**, **JINR** (Dubna, near Moscow), Leningrad and **KEK** (Japan).

There are two types of μSR: transverse field and longitudinal field. A magnetic field is applied perpendicular or parallel, respectively, to the initial muon polarization. The

Table III.1

Muon and Muonium Properties

Positive Muon	μ^+
spin	1/2
mass	1/9 mass of proton 105.6596 MeV c^{-2}
magnetic moment	28.0272×10^{-18} MeV G^{-1} 3.18 proton magnetic moment
gyromagnetic ratio, γ_μ	13.544 kHz G^{-1}
mean lifetime, τ	2.197μs
Muonium, Mu	μ^+e^-
spin	1 for triplet 0 for singlet
mass	1/9 mass of protonium
Bohr radius	0.5315 Å
ionization potential	13.539 eV
gyromagnetic ratio, γ_M	1.394 MHz G^{-1}
hyperfine frequency, ω_0	4463 MHz
mean lifetime, τ	limited by that of μ^+

sample is placed in the path of the muon beam. Various degraders and collimators are used to ensure that the muons stop inside the placed sample. In the sample, the muon decays into a positron and two neutrinos in the process:

$$\mu^+ \rightarrow e^+ + \bar{\nu}_\mu + \nu_e \qquad (3.2).$$

The angular distribution of positrons is anisotropic with the greatest probability in the direction of the muon spin at the moment of decay. As a result, the variation of positron detection probability in a given direction reflects the evolution of the muon spin polarization.

In the absence of muon spin polarization, the histogram accumulated would depict a single exponential decay. In a transverse field experiment, the precession of the muon spin in the applied field results in an oscillation of the e^+ signal. Figure III.1 is a typical example of the muon spin precession signal in water in a transverse field experiment. The general form of the histogram is :

$$N = B + N_0 \exp(-t/\tau) [1 + A(t)] \qquad (3.3)$$

where N_0 is the normalization factor, B is the background, and τ is the life-time of the muon. $A(t)$, the asymmetry factor, includes the sum of the time dependence of the muon and muonium spin polarization, and various geometrical parameters.

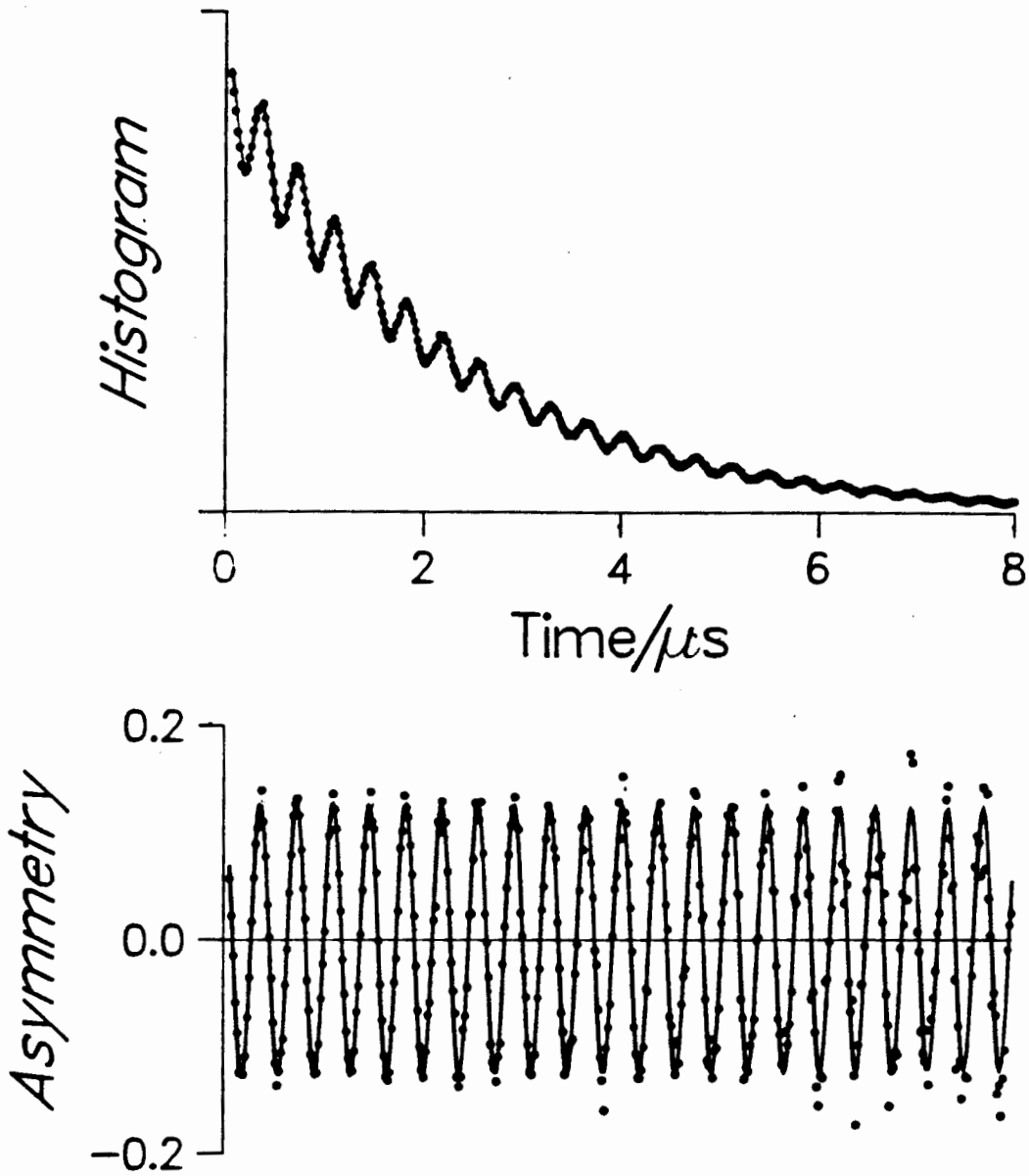

Figure III.1. μSR histogram (top) and diamagnetic signal (bottom) from water in a transverse field of 200 G. The precession signal is obtained from the histogram by subtraction of the background and dividing out the exponential decay.

Muonium is a two spin-$\frac{1}{2}$ system. Therefore, there are four spin states for muonium. For a symmetric hyperfine tensor, the spin states are divided into a singlet and a triplet at zero field. If a magnetic field is applied to muonium, the degeneracy of the triplet state is lifted. Figure III.2 describes the variation of the energy levels of the four spin states as a function of the strength of the applied field (*Breit-Rabi Diagram*). In a transverse field experiment, the precession signal of this system will consist of four allowed transition frequencies. However, two frequencies are too high to be resolved by conventional μSR techniques. At low applied field, the two observable frequencies are degenerate. At moderate fields, the degeneracy will be lifted and the two frequencies will give rise to the beat pattern given in Figure III.3. The signals are field dependent and their splittings can be obtained by Fourier transforming the time spectrum.

3. μSR spectrum of muonium in ice

Figure III.4 is a μSR spectrum of muonium in a D_2O single crystal of ice Ih at 146 K with an applied field of 10 G. The crystal has its *c*-axis oriented parallel to the applied magnetic field. The beat pattern represents a splitting of 1.2 MHz. At 10 G, Zeeman splitting is minor (0.09 MHz). The experimental splitting is temperature and isotope independent [11,36]. However, it is orientational dependent, *i.e.*, its magnitude

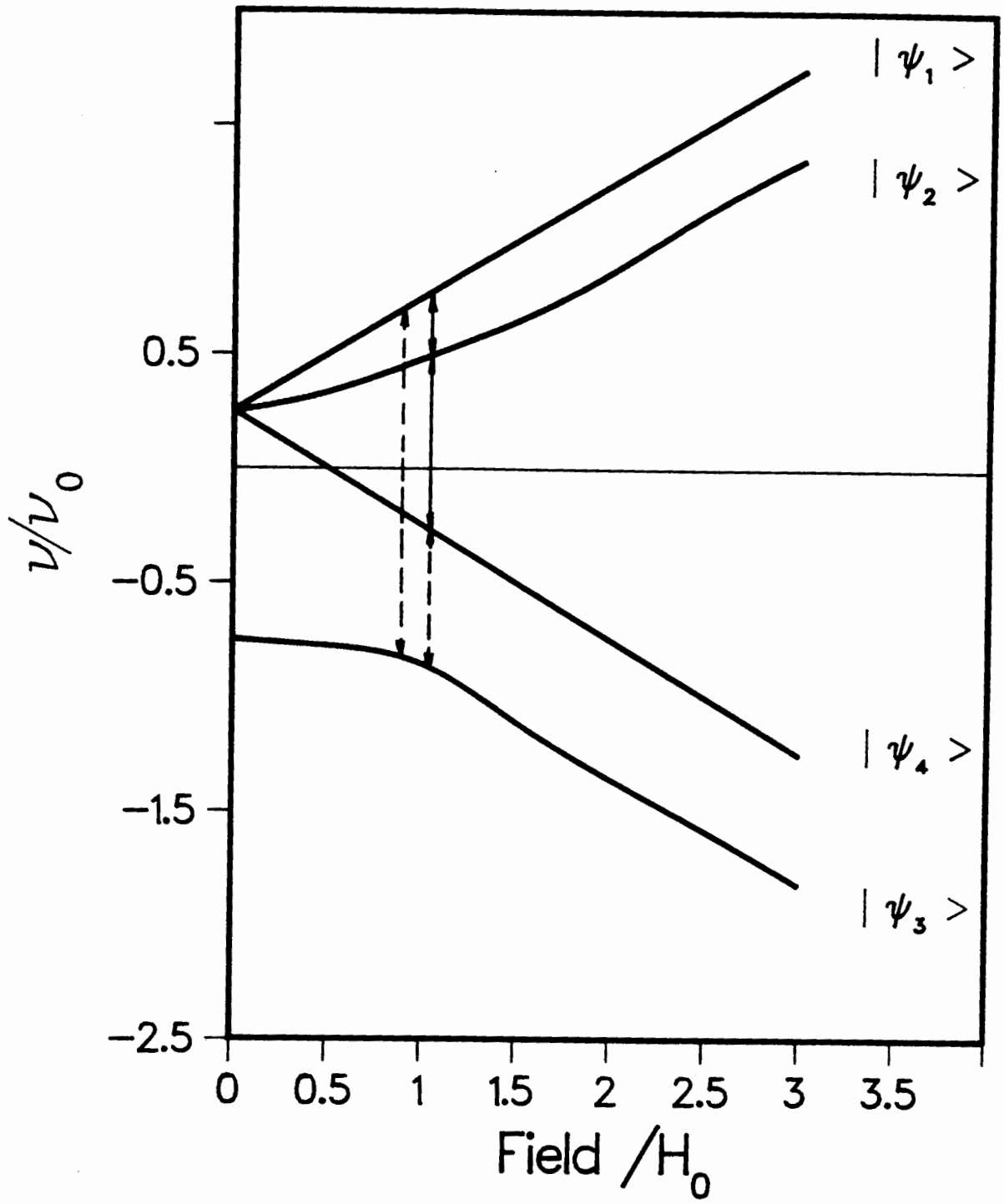

Figure III.2. Breit-Rabi diagram of the energy levels of a two spin ½ system as a function of applied magnetic field. Of the four allowed transitions, only the two denoted by full lines are resolvable in a low transverse field μSR experiment. (H_0 = 1585 G, ν_0 = 4463 MHz)

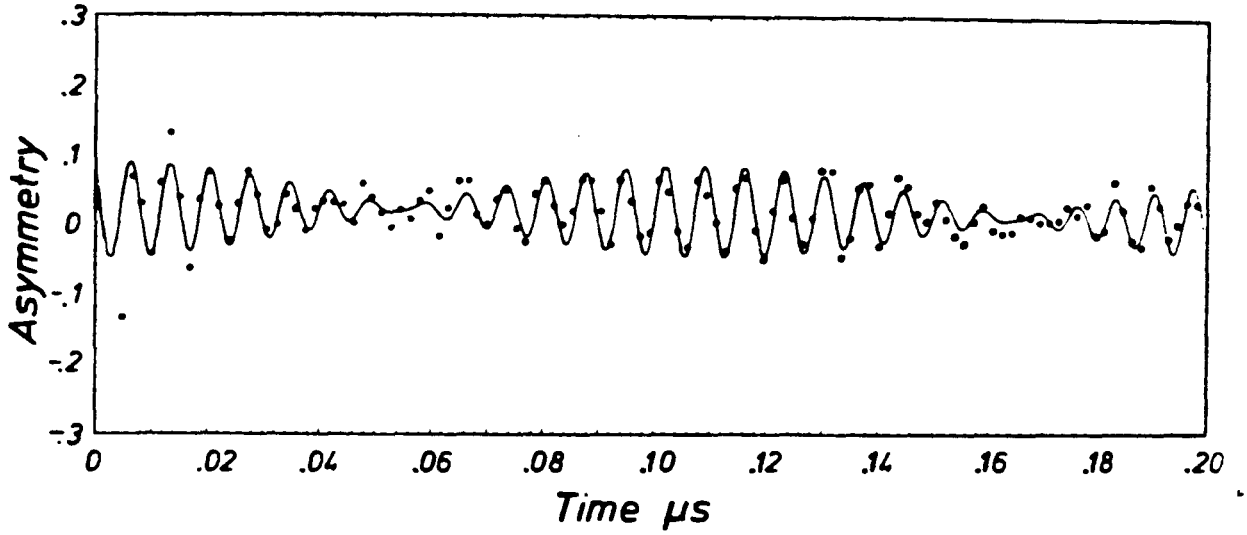

Figure III.3. Split muonium precession signal from quartz in a 101 Gauss magnetic field.

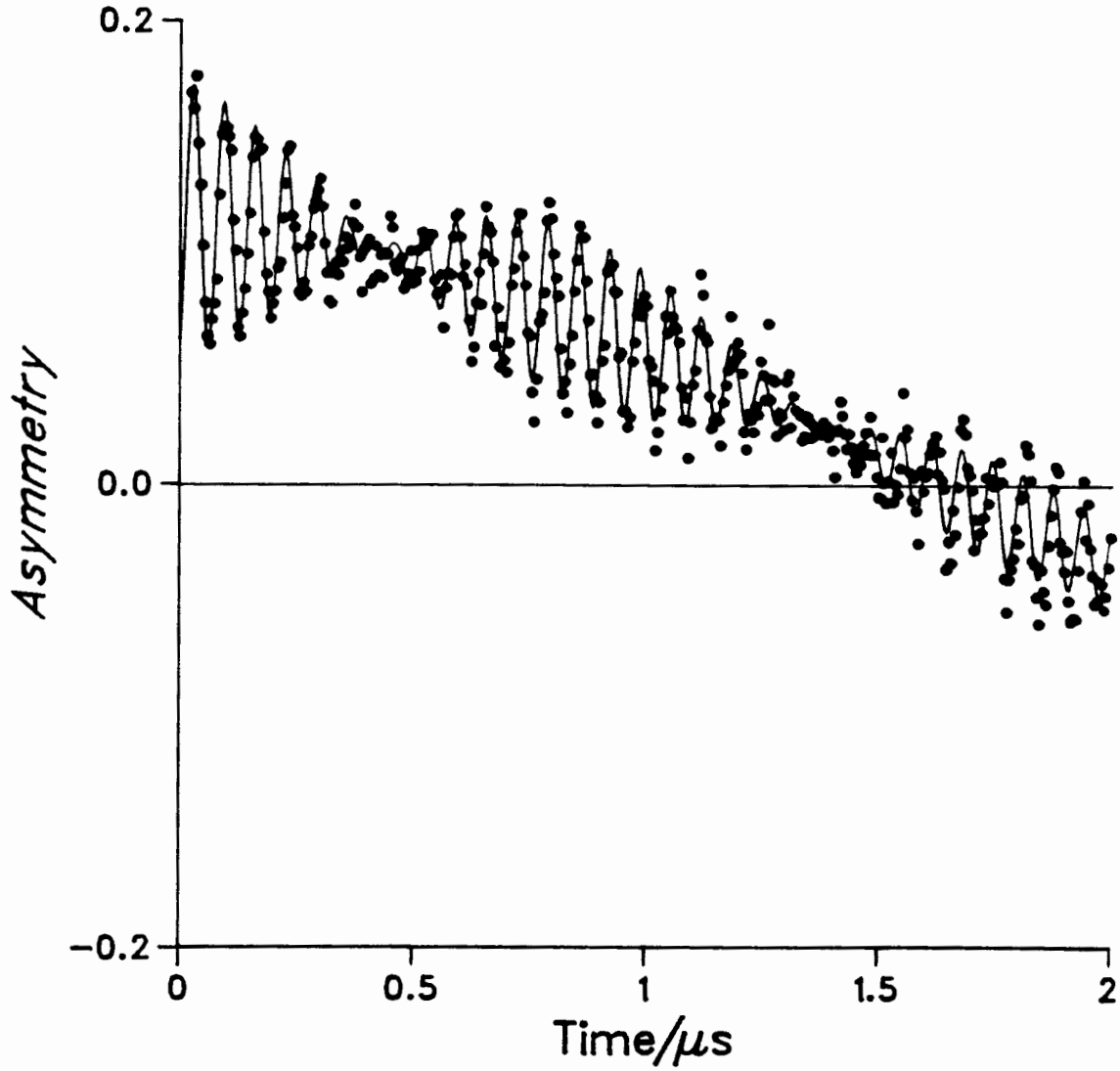

Figure III.4. Split muonium precession signal in a D_2O crystal at 211 K with its *c*-axis parallel to a magnetic field of 10 G.

depends on the angle the *c*-axis makes with the applied field, B_0. This same field dependent splitting had been observed in a single crystal of quartz by Brewer *et al* [12,13,14]. They concluded that the hyperfine interaction of muonium in quartz is slightly anisotropic. In their case, the hyperfine tensor was axially symmetric for temperatures above 130 K but became totally anisotropic for temperatures below that.

A striking similarity relates single crystals of quartz to single crystals of ice Ih - they both have hexagonal channels parallel to the *c*-axis of the crystal. In view of this, Percival *et al* [11], postulated that the hyperfine tensor for single crystal of ice Ih is also anisotropic with axial symmetry. In addition, they found that this axial symmetry is preserved for temperatures as low as 4.3 K.

The spin Hamiltonian for muon spin, I, and electron spin, S, in ice Ih can be written as:

$$\mathbf{H} = \omega_e \hbar \mathbf{S} - \omega_\mu \hbar \mathbf{I} + \mathbf{S} \cdot \mathbf{T} \cdot \mathbf{I} \qquad (3.4).$$

where the anisotropic tensor, T, has the axially symmetric form:

$$\mathbf{T} = \begin{bmatrix} A_\perp & 0 & 0 \\ 0 & A_\perp & 0 \\ 0 & 0 & A_{//} \end{bmatrix} \qquad (3.5)$$

when written in the principal axes of the crystal. The electron and muon Larmor precession frequencies, ω_e and ω_μ respectively,

are field dependent.

For a transverse field μSR experiment, the axis of quantization of the spins is defined by the direction of the applied magnetic field. Because the principal axes of the crystal and the axis of quantization are different, a unitary transformation has to be taken to transform the principal axis of the crystal into the laboratory frame of reference where the axis of quantization is defined, *i.e.*,

$$T' = U^{-1} \cdot T \cdot U \qquad (3.6).$$

Utilizing the axial symmetry of the crystal, it is up to one's discretion to choose the x- and y-axes of the crystal. If θ is the angle the principal axis of the crystal makes with the axis of quantization, and if one chooses to have the y-axis of the crystal in the xy-plane of the laboratory, the unitary matrix required to rotate the co-ordinates of the crystal into those of the laboratory is:

$$U = \begin{bmatrix} \cos\theta & 0 & \sin\theta \\ 0 & 1 & 0 \\ -\sin\theta & 0 & \cos\theta \end{bmatrix} \qquad (3.7).$$

After some simple algebra and utilizing the step-up, S_+, and step-down, S_-, operators, the Hamiltonian becomes:

$$H = \omega_e S_z - \omega_\mu I_z + 2\pi\{(\Theta - A_\perp)/4\,[S_+I_- + S_-I_+] + (\Theta + A_\perp)/4\,[S_+S_- + S_-I_+] + \Xi/2\,[S_+I + S_-I + SI_+ + SI_-] + \Phi SI\} \quad (3.8)$$

where $S_+ = S_x + iS_y$ (3.9)

$S_- = S_x - iS_y$ (3.10)

$I_+ = I_x + iS_y$ (3.11)

$I_- = I_x - iS_y$ (3.12)

$\Theta = (A_\perp - A_{//})\cos^2\theta + A_{//}$ (3.13)

$\Xi = (A_\perp - A_{//})\cos\theta\sin\theta$ (3.14)

$\Phi = (A_{//} - A_\perp)\cos^2\theta + A_\perp$ (3.15)

The four wave functions which describe the basis set of the coupling of the electron spin to the muon spin are: $|\alpha\alpha\rangle$, $|\alpha\beta\rangle$, $|\beta\alpha\rangle$, and $|\beta\beta\rangle$, where the first spin refers to the electron spin and the second to that of the muon. Since the anisotropy of the hyperfine tensor is small, the terms $(\Theta - A_\perp)$ and Ξ are neglected. Utilizing the fact that $H\Psi = E\Psi$, the secular determinant can be written as:

$$\begin{bmatrix} \omega_- + 2\pi\Phi/4 - E & 0 & 0 & 0 \\ 0 & \omega_+ - 2\pi\Phi/4 - E & 2\pi(\Theta + A_\perp)/4 & 0 \\ 0 & 2\pi(\Theta + A_\perp)/4 & -\omega_+ - 2\pi\Phi/4 - E & 0 \\ 0 & 0 & 0 & -\omega_- + 2\pi\Phi/4 - E \end{bmatrix} = 0 \quad (3.16)$$

where $\omega_- = (\omega_e - \omega_\mu)/2$ (3.17)

$$\omega_+ = (\omega_e + \omega_\mu)/2 \qquad (3.18).$$

After solving the quadratic equation, the four energy levels of muonium in ice can be obtained:

$$E_1 = \omega_- + \delta\omega/4 + \omega_1/2 \qquad (3.19)$$

$$E_2 = -\delta\omega/4 + \omega_1/2 + \Omega \qquad (3.20)$$

$$E_3 = -\delta\omega/4 - \omega_1/2 - \Omega \qquad (3.21)$$

$$E_4 = -\omega_- + \delta\omega/4 + \omega_1/2 \qquad (3.22)$$

where $\delta\omega = \pi\,[(3\cos^2\theta - 1)\,(A\perp - A//)]$ (3.23)

$$\omega_1 = 2\pi\,[A\perp + \tfrac{1}{2}(A// - A\perp)\sin^2\theta] \qquad (3.24)$$

$$\Omega = \tfrac{1}{2}\,(\sqrt{\omega_+^2 + \omega_1^2} - \omega_1) \qquad (3.25).$$

The two symmetric wavefunctions $|\alpha\alpha\rangle$ and $|\beta\beta\rangle$ remain eigenfunctions of the spin system while the two antisymmetric wavefunctions mix with each other to form the other two eigenfunctions. The two mixed eigenfunctions are solved by the orthogonality relation of the wavefunctions. The four eigenfunctions corresponding to these four energy levels are:

$$|\Psi_1\rangle = |\alpha\alpha\rangle \qquad (3.26)$$

$$|\Psi_2\rangle = c\,|\alpha\beta\rangle + s\,|\beta\alpha\rangle \qquad (3.27)$$

$$|\Psi_3\rangle = -s\,|\alpha\beta\rangle + c\,|\beta\alpha\rangle \qquad (3.28)$$

$$|\Psi_4\rangle = |\beta\beta\rangle \qquad (3.29)$$

where $c^2 = \frac{1}{2} \{ 1 + [\omega_+ / \sqrt{\omega_+^2 + \omega_1^2}] \}$ (3.30)

$$c^2 + s^2 = 1 \quad (3.31).$$

The experimental observables are the transitions between these four energy levels. The selection rules for the transitions between these spin energy levels can be obtained by calculating the expectation value of the relevant operator:

$$P = \langle \Psi \mid \hat{o} \mid \Psi \rangle \quad (3.32).$$

In a transverse field μSR experiment, the muons spins are completely polarized, *i.e.*, only the β states are populated, and are in the x-y plane of the laboratory frame of reference. The muonium electrons, because of their origin, are not polarized and can take the values of α or β. The observable transitions are those between muon spins. The expectation value of the muon step-up operator is used to calculate the transition probabilities. Using this operator and Equation 3.32, the selection rules for allowed transitions were determined to be $\Delta m = \pm 1$. The four allowed transitions are :

$$|\Psi_1\rangle \rightarrow |\Psi_3\rangle \quad (3.33)$$

$$|\Psi_1\rangle \rightarrow |\Psi_2\rangle \quad (3.34)$$

$$|\Psi_2\rangle \rightarrow |\Psi_4\rangle \quad (3.35)$$

$$|\Psi_3\rangle \rightarrow |\Psi_4\rangle \quad (3.36).$$

The four precession frequencies corresponding to these four transitions are:

$$\omega_{12} = \omega_{-} + \tfrac{1}{2}\delta\omega - \Omega \qquad (3.37)$$

$$\omega_{13} = \omega_{-} + \tfrac{1}{2}\delta\omega + \Omega + \omega_1 \qquad (3.38)$$

$$\omega_{24} = \omega_{-} - \tfrac{1}{2}\delta\omega + \Omega \qquad (3.39)$$

$$\omega_{34} = \omega_{-} - \tfrac{1}{2}\delta\omega - \Omega - \omega_1 \qquad (3.40).$$

Since the direction of the applied field is the axis of quantization of the muon spin, The observed muon polarization is:

$$P_{+} = P_x + iP_y \qquad (3.41)$$

$$= \tfrac{1}{2}c^2\{\exp(i\omega_{12}t) + \exp(i\omega_{34}t)\} + \tfrac{1}{2}s^2\{\exp(i\omega_{13}t) + \exp(i\omega_{24}t)\} \qquad (3.42).$$

The two transition frequencies, ω_{13} and ω_{34} are too high to be resolved by conventional μSR techniques. The two remaining frequencies give rise to the beat pattern shown in Figure III.4. The splitting of these two frequencies is $(\delta\omega - 2\Omega)$. The Breit-Rabi diagram which describes the variation of the energy levels of the four spin states as a function of applied field is given in Figure III.5. In the low field limit, $\Omega \rightarrow 0$, the frequency splitting should exhibit the characteristic $(3\cos^2\theta-1)$ dependence. This had been confirmed by Percival *et al* [7]. Their data revealed the magnitude of the anisotropy,

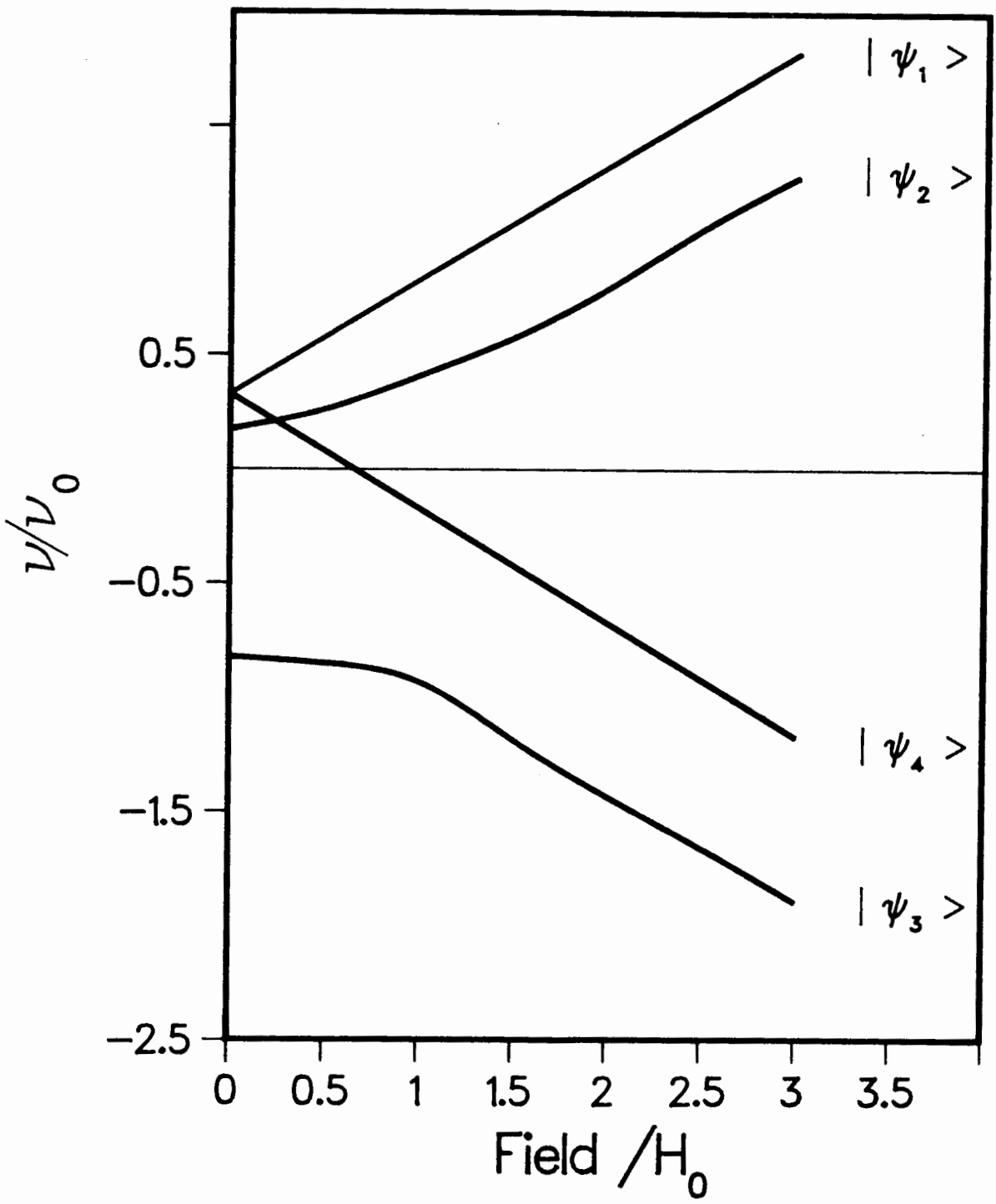

Figure III.5. Breit-Rabi diagram for muonium in ice Ih as a function of applied magnetic field strength.

$|A//-A\perp|$ = 1.27 MHz for both H_2O- and D_2O-single crystals of ice.

Another important feature of the four spin states is that at zero applied field, the triplet state is not degenerate as in the isotropic case. So, for a zero field μSR experiment, one should be able to observe a signal corresponding to the allowed transitions. This expected zero-field oscillation ($\nu = \frac{1}{2}(A\perp - A//)$) has been observed for muonium in both single crystals of H_2O- and D_2O-ices oriented with their c-axes perpendicular to the beam polarization [36].

The splitting caused by the anisotropic hyperfine tensor is field independent and is negative with respect to the Zeeman splitting. Since Zeeman splitting is field dependent, there should exist a field such that both effects cancel each other. The magnitude of the field was calculated to be 37 G for the situation when the c-axis of the crystal is parallel to the applied field. At this applied field strength, the two transitions become degenerate and only a single muonium precession frequency is present. This has been observed for both H_2O- and D_2O-ices [36].

IV. Line broadening mechanisms for Mu in ice

1. Line broadening in solids

There are two principal types of resonant lines in solids: those that are homogeneously broadened and those that are inhomogeneously broadened. The former are pure spectral singlets. The latter type consists of a spectral distribution of much narrower homogeneously broadened lines.

In 1946, Bloch proposed a set of phenomenological differential equations to describe the time dependence of the components of magnetization in the presence of an applied field [37]. Solutions to these equations allow the lineshape and relaxation behaviour of material under magnetic resonance conditions to be predicted. This set of equations applies to homogeneously broadened lines at or near resonance. The Lorentzian lineshape function for the absorption mode is [38]:

$$I(\omega) = 2T_2/(1+\Delta\omega^2 T_2^2) \qquad (4.1)$$

where T_2 is the transverse or spin-spin relaxation time in s,

$\Delta\omega = \omega - \omega_0$,

ω_0 is the Larmor precession frequency in radians/s,

ω is the observed frequency in radians/s.

The maximum of this function occurs at frequency ω_0 and is equal to $2T_2$. A straightforward algebraic manipulation leads to the result that $T_2 = 2/\omega(\frac{1}{2})$, where $\omega(\frac{1}{2})$ is the full width at half maximum (FWHM) of the absorption signal. The corresponding expression for a Gaussian lineshape is:

$$T_2 = 2\sqrt{(\pi \ln 2)}/\omega(\tfrac{1}{2}). \qquad (4.2).$$

Homogeneous broadening occurs when the magnetic resonance signal results from a transition between two spin levels which are somewhat intrinsically broadened. Several sources of homogeneous broadening are: (1) dipolar broadening between like spins, (2) spin-lattice relaxation, (3) interaction with the radiation field, (4) diffusion of excitation throughout the sample, and (5) motionally narrowing fluctuations in the local field.

An inhomogeneously broadened resonant line is one which consists of a spectral distribution of individual lines merged into one overall line or envelope. Several sources of inhomogeneous line broadening are :(1) applied field inhomogeneity, (2) dipolar interaction between unlike spins, (3) unresolved hyperfine structure, and (4) crystal lattice irregularities (*e.g.*, mosaic structure).

2. Theory of spin-spin relaxation mechanisms in solid

According to general magnetic resonance theory, the efficiency of spin-spin relaxation mechanisms is determined by a "correlation time" constant, τ_c, which characterizes the time scale for fluctuation in the frequency spectrum of local fields at the spin concerned [39]. T_2 consists of an energy term describing the coupling between the observed spin and other spins and a spectral density function. The various physical interactions which can provide a mechanism for spin-spin energy transfer in solids are: (1) dipole-dipole coupling, (2) electric quadrupole interaction, (3) relaxation through chemical shift anisotropy, and (4) scalar coupling. The total effect of these relaxation mechanisms is expressed as a sum of all the individual relaxation rates:

$$T_2^{-1} = T_2^{-1}(DD) + T_2^{-1}(SC) + T_2^{-1}(EQ) + T_2^{-1}(AH) \quad (4.3)$$

where DD = dipole-dipole coupling,
SC = scalar coupling,
EQ = electric quadrupole interaction,
AH = hyperfine anisotropy.

For muonium in ice, the broadening due to the anisotropic hyperfine tensor (only for polycrystalline samples) and dipole-dipole interactions between muonium and the lattice

hydrogen/deuterium nuclei are shown later to be dominant. Other minor effects, such as the coupling of the muon spin with the nuclear quadrupole moment of deuterium ($Q(^2H) = 2.8 \times 10^{-28}$ m^2), can be neglected. There is of course some broadening due to field instability and applied field inhomogeneity which will be discussed later in Section VI.6.

3. Inhomogeneous line broadening by anisotropic hyperfine tensor

Polycrystalline ice is made up of micro-crystals in many different orientations. Since the magnitude of the shift of the resonance frequency is dependent on the angle the c-axis makes with the applied magnetic field, each micro-crystal will give a slightly different spectrum. The result of this will be a powder spectrum well known in ESR and NMR spectroscopies [39]. The spectrum of muonium in polycrystalline ice contains contributions from all crystal orientations. Each contribution consists of a pair of lines at $\nu(\mathrm{Mu}) \pm (A_\perp - A_{//})(3\cos^2\theta - 1)/4$ with weighting proportional to $\sin\theta$. The simulated line shapes of muonium in polycrystalline ice for several natural line widths are given in Figure IV.1 [7]. The pure "powder pattern" spectrum is shown in part (a). The effect of increasing natural line-width is demonstrated in parts (b) to (d). The line widths correspond to actual values for muonium in H_2O at approximately 260 K, 220 K, and 130 K. At higher temperatures, the powder line width is dominant. Any attempt to derive relaxation times from

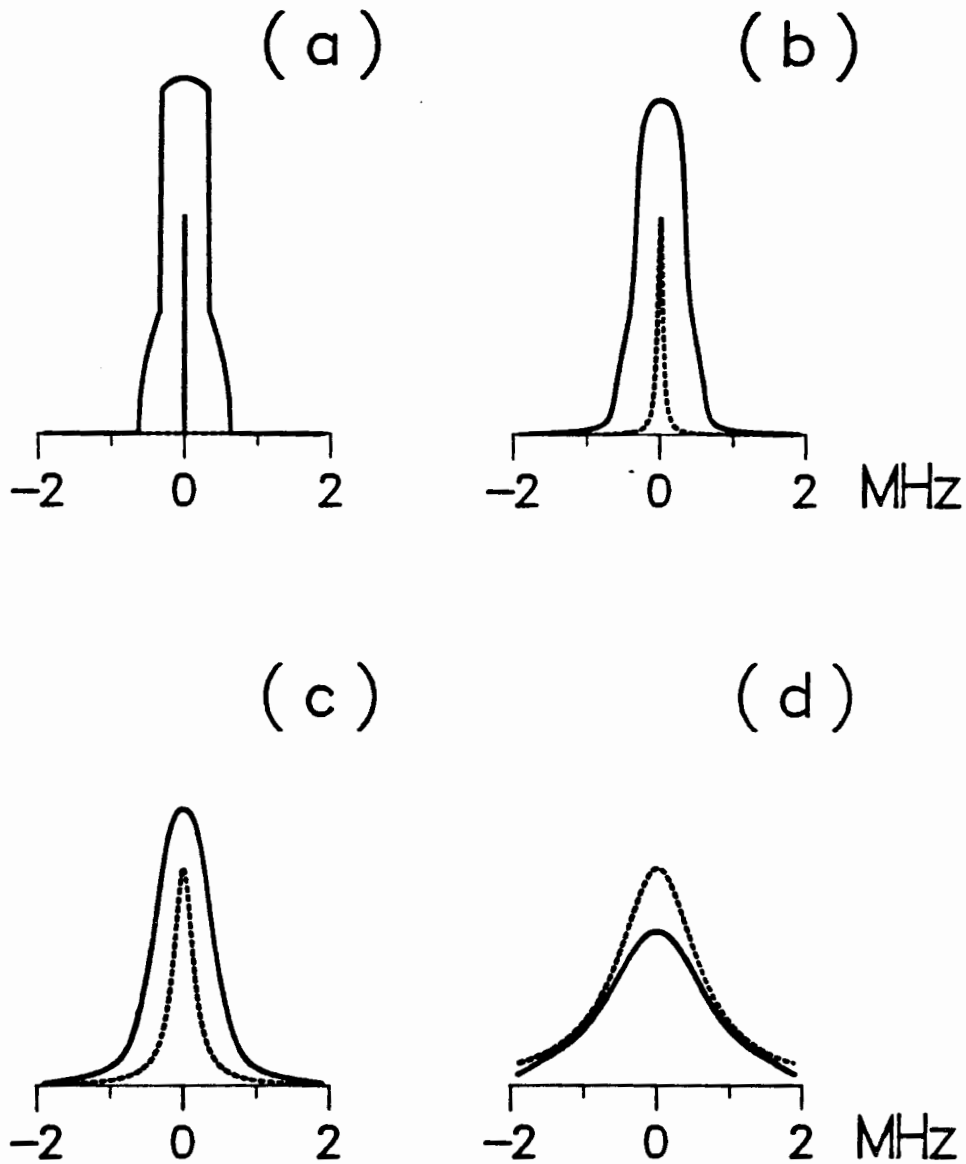

Figure IV.1. Simulated line shapes (solid lines) of muonium in polycrystalline ice for natural line widths (FWHM) of (a) 0, (b) 0.08, (c) 0.32, (d) 1.28 MHz. For comparision, single Lorentzian lines of corresponding width are shown by the dotted curves [36].

the decay curves which are Fourier transforms of these spectra will only result in decay constants characteristic of the inhomogeneous line width. The results obtained by Gurevich *et al* [9] suffered from this inhomogeneous broadening and led them to the erroneous conclusion that muonium does not diffuse in ice at 77 K.

4. Dipole-dipole interaction

Classically, a magnetic point dipole, $\bar{\mu}_1$, interacts with another magnetic point dipole, $\bar{\mu}_2$, located at a distance $\bar{r}$ away from it by means of the dipolar interaction [39]:

$$E = \bar{\mu}_1 \cdot \bar{\mu}_2 / r^3 - 3(\bar{\mu}_1 \cdot \bar{r})(\bar{\mu}_2 \cdot \bar{r})/r^5 \qquad (4.4).$$

This is a through space interaction which occurs because two spins exert a magnetic field on each other. For two spins I_1 and I_2, since $\mu = \gamma \hbar I$, the Hamiltonian for dipolar interaction can be written as:

$$H = \gamma_1 \gamma_2 \hbar^2 \{ I_1 \cdot I_2 / r^3 - 3(I_1 \cdot \bar{r})(I_2 \cdot \bar{r})/r^5 \} \qquad (4.5).$$

When the scalar products are expanded, the expression transformed into spherical co-ordinates, and utilizing the step-up and step-down operators analogous to those defined in the chapter before, Equation 4.5 can be expressed in six

terms [40]:

$$H = \gamma_1\gamma_2\hbar^2/r^3\ [A + B + C + D + E + F] \qquad (4.6)$$

where $A = -I_1I_2(3\cos^2\theta-1)$ (4.6a),

$B = \frac{1}{4}(I_{+1}I_{-2} + I_{-1}I_{+2})(3\cos^2\theta-1)$ (4.6b),

$C = -\frac{3}{2}(I_1I_{+2} + I_{+1}I_2)\sin\theta\cos\theta\exp(-i\phi)$ (4.6c),

$D = -\frac{3}{2}(I_1I_{-2} + I_{-1}I_2)\sin\theta\cos\theta\exp(i\phi)$ (4.6d),

$E = -\frac{3}{4}I_{+1}I_{+2}\ \sin^2\theta\exp(-2i\phi)$ (4.6e),

$F = -\frac{3}{4}I_{-1}I_{-2}\ \sin^2\theta\exp(2i\phi)$ (4.6f).

Each of the terms A to F contains a spin factor and a geometric factor, the effects of which can be appreciated separately. Term A causes broadening of the intrinsic line-width. Term B contains the "*flip-flop*" operator, which links the $|\alpha\beta\rangle$ and $|\beta\alpha\rangle$ only, whereas, terms C and D, which contain one step-up or step-down operator, link states differing by m = 1 in the total spin angular momentum, m, of the system. As a summary, the spectral densities and the induced transitions by the dipolar Hamiltonian are given in Table IV.1. The expressions for W^0, W_1^1, W_2^1, and W^2 have been determined explicitly [40]:

$$W^0 = (2\pi R)^2\ J(\omega_2-\omega_1)/20 \qquad (4.7),$$

$$W_1^1 = 3(2\pi R)^2\ J(\omega_1)/40 \qquad (4.8),$$

$$W_2^1 = 3(2\pi R)^2\ J(\omega_2)/40 \qquad (4.9),$$

Table IV.1

Transitions induced by the dipolar Hamiltonian.

Transition	Dipolar term	Transition rate	Spectral density
/	A	/	$J(0)$
$\|\alpha\beta\rangle \leftrightarrow \|\beta\beta\rangle$	C,D	W_1^1	$J(\omega_1)$
$\|\alpha\alpha\rangle \leftrightarrow \|\beta\alpha\rangle$	C,D	W_1^1	$J(\omega_1)$
$\|\beta\alpha\rangle \leftrightarrow \|\beta\beta\rangle$	C,D	W_2^1	$J(\omega_2)$
$\|\alpha\alpha\rangle \leftrightarrow \|\alpha\beta\rangle$	C,D	W_2^1	$J(\omega_2)$
$\|\alpha\beta\rangle \leftrightarrow \|\beta\alpha\rangle$	B	W^0	$J(\omega_2-\omega_1)$
$\|\alpha\alpha\rangle \leftrightarrow \|\beta\beta\rangle$	E,F	W^2	$J(\omega_2+\omega_1)$

Definition of transitions

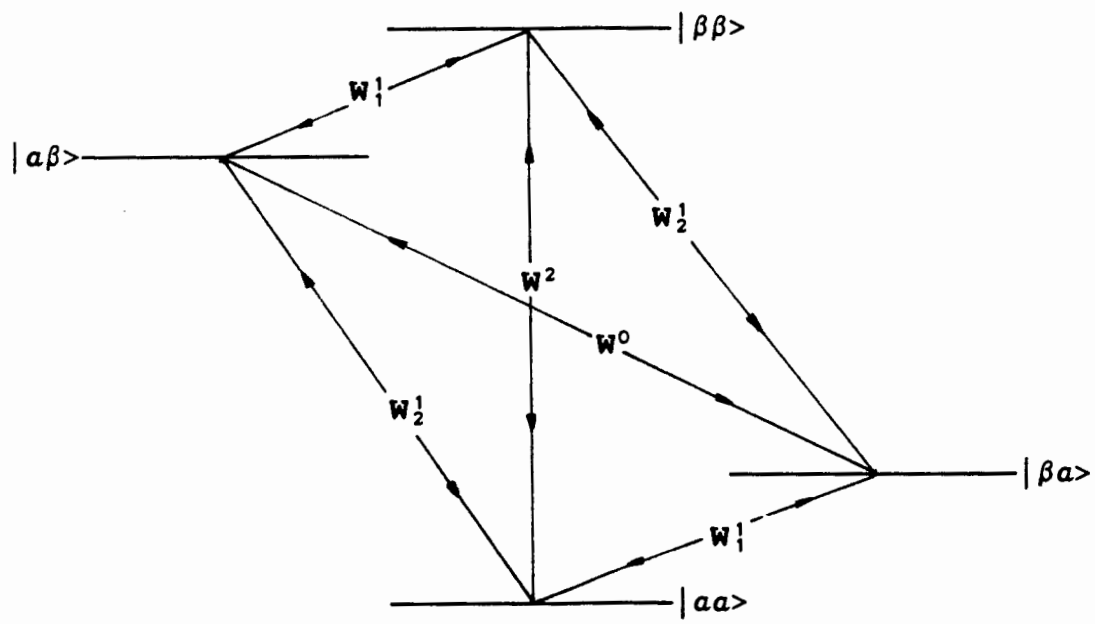

$$W^2 = 3(2\pi R)^2 J(\omega_2+\omega_1)/10 \quad (4.10),$$

where R is the dipolar interaction constant:

$$R = \gamma_1\gamma_2(\hbar/2\pi)/r^3 \quad (4.11).$$

In addition to these contributions, the terms causing spin-lattice relaxation lead to an uncertainty in the transitions and hence will contribute to the value of T_2^{-1}. The dipolar term A modulates the energy levels directly, leading to a secular contribution to linewidths and T_2^{-1} which depends on the zero-frequency spectral density J(0). If there is only a single correlation time constant, τ_c, the spin-spin relaxation rate, T_2^{-1}, can be obtained [40]:

$$\begin{aligned} T_2^{-1} = {} & 1/15\ I_2(I_2+1)\ (2\pi R)^2\tau_c\{4 + [1+(\omega_2-\omega_1)^2\tau_c^2]^{-1} + \\ & 3[1+\omega_1^2\tau_c^2]^{-1} + 6[1+\omega_2^2\tau_c^2]^{-1} + \\ & 6[1+(\omega_1+\omega_2)^2\tau_c^2]^{-1}\} \end{aligned} \quad (4.12).$$

The gyromagnetic ratio, γ_1, for muonium is 1.394 MHz/G whereas that of the hydrogen nuclei, γ_2, is 1/328 that of muonium. Therefore, for muonium in an ice lattice, $\omega_1 >> \omega_2$. For low field limit, *i.e.*, $\omega_M^2\tau_c^2 << 1$, Equation 4.12 is simplified to:

$$T_2^{-1} = \tfrac{2}{3}I_2(I_2+1)(2\pi R)^2\tau_c[1 + (1+\omega_1^2\tau_c^2)^{-1}] \quad (4.13).$$

5. Motional narrowing

Diffusion of ions and atoms are known to exist in many crystals [41]. This is particularly easy for muonium in ice **Ih** because of its light mass and of the existence of the hexagonal channels parallel to the *c*-axis. The resonance line-width will be narrowed because of this diffusion of muonium and it is termed, in magnetic resonance nomenclature, motional narrowing effect.

The time dependence of the homogeneous line broadening caused by dipolar interaction between the muonium spin and the spin of the lattice nuclei is [40]:

$$P = P_0 \exp\{-2\sigma^2\tau_c^2 [\exp(-t/\tau_c) - 1 + t/\tau_c]\} \quad (4.14)$$

where P_0 is the initial muon polarization, τ_c is the average time spent by muonium in one crystal cell, and σ is:

$$\sigma = \mu\sqrt{(I+1)/I} \quad (4.15)$$

where I and μ are the spin and magnetic moment of the lattice nuclei respectively.

It follows that for fast diffusion ($t>>\tau$):

$$P = P_0 \exp(-2\sigma^2 t\,\tau_c) \quad (4.16)$$

and in the absence of diffusion ($\tau \rightarrow \infty$):

$$P = P_0 \exp(-\sigma^2 t^2) \qquad (4.17).$$

If λ is the reciprocal of the time take for the precession amplitude to decrease by a factor of e, then, for fast diffusing muonium [9]:

$$\lambda(H_2O)/\lambda(D_2O) = \sigma(H)^2/\sigma(D)^2 \simeq 16 \qquad (4.18)$$

and for non-diffusing muonium [9]:

$$\lambda(H_2O)/\lambda(D_2O) = \sigma(H)/\sigma(D) \simeq 4 \qquad (4.19)$$

where $\tau_c(H_2O)$ is assumed to be equal to $\tau_c(D_2O)$. Hence, by measuring the experimental relaxation rates of muonium in H_2O- and D_2O- single crystals of ice at various temperatures, the ratio of the two relaxation rates can be calculated. By comparing with Equations 4.18 and 4.19, the motion of muonium/hydrogen in ice can be characterized. The fast diffusion and slow diffusion regimes can then be defined.

6. The calculated static dipolar line width of muonium in ice

The mathematical complications involved in solving the dipolar Hamiltonian may be circumvented by computing several moments of the line using the trace method [41]. The n-*th* moments, $\langle(\omega-\omega_0)^n\rangle$, centered about ω_0, the center frequency of the unbroadened line, are of practical use [41]. They allow the shapes and widths of the resonant lines to be estimated.

The second moment $\langle\omega^2\rangle$ is given by [39]:

$$\langle\omega^2\rangle = Tr\{[\mathbf{H},\mathbf{I}]^2\}/\hbar^2 Tr(\mathbf{I})^2 \qquad (4.20)$$

where the square bracket denotes the commutator of the two operators and *Tr* is the trace of the operator. Since frequency, ω, is related to applied field by the relation $\omega = \gamma H$, one can calculate the second moment by evaluating the quantity ΔH. The change in magnetic field, ΔH, caused by nuclei with spins, I_2, and experienced by a nucleus with spin, I_1, at a distance r away is given by [41]:

$$\Delta H = \gamma_2 \hbar \sqrt{[I_2(I_2+1)]} \sum_i (1-3\cos^2\theta_i)/r_i^3 \qquad (4.21)$$

where θ is the angle between the applied magnetic field and the line joining the two interacting nuclei. Then the second moment becomes:

$$<(\omega-\omega_0)^2> \quad = \quad <\gamma_1^2\Delta H^2> \qquad (4.22).$$

Solving for the second moment explicitly, one has:

$$<(\omega-\omega_0)^2> \quad = \quad 4/15\ \gamma_1^2\gamma_2^2\hbar^2 I_2(I_2+1) \sum_i (1-3\cos^2\theta_i)^2/r_i^6 \qquad (4.23)$$

where the sum is to be taken over all the lattice nuclei. For a Gaussian line-shape, the relaxation time, T_2, is related to the second moment by the following expression:

$$T_2 \quad = \quad \sqrt{\pi/(2<(\omega-\omega_0)^2>)} \qquad (4.24).$$

For muonium in H_2O- and D_2O- ices, the line shapes as caused by static dipolar interaction between the muonium and the lattice nuclei were simulated. Muonium was taken to be in a cavity defined by two chair forms of the oxygen nuclei. The number of hydrogen/deuterium nuclei used in the calculation was 15 corresponding to the 12 H/D nuclei in the two layers defining the cavity and the 3 H/D nuclei between the layers. The quantity ΔH was evaluated for each combination of the spins of the H/D nuclei. There were 2^{15} spin combinations for hydrogen ($I = \frac{1}{2}$) and 3^{15} for deuterium ($I = 1$). The calculated values of ΔH were accumulated in a histogram. The histogram was normalized with the total number of spin combinations being 1. The simulated line shapes are given in Figure IV.2 and IV.3. The second,

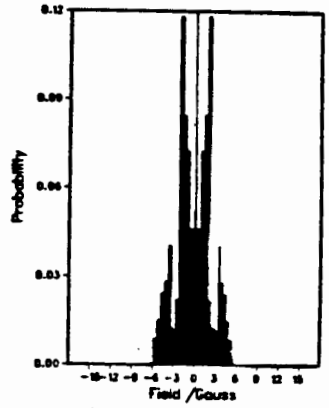

(i)

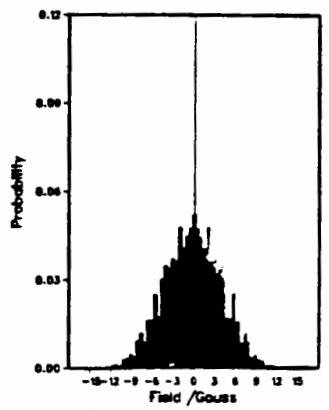

(ii)

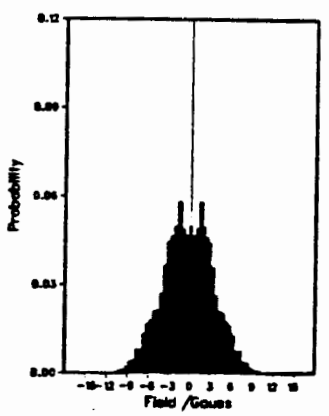

(iii)

Figure IV.2. Simulated static dipolar line shapes of muonium in H_2O-ice. The c-axis of the crystal is (i) 0°, (ii) 55°, (iii) 90° to the applied field.

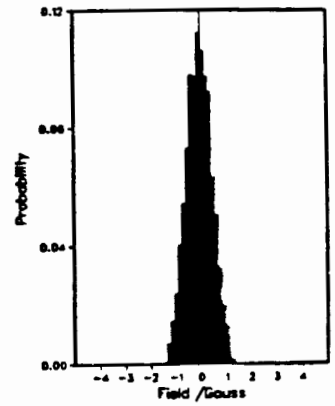

(i)

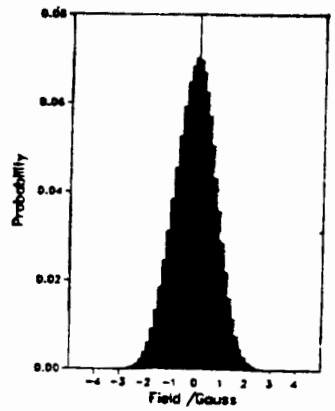

(ii)

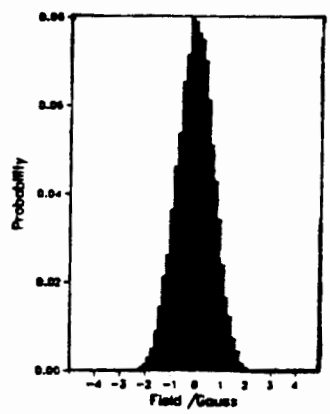

(iii)

Figure IV.3. Simulated static dipolar line-shapes of muonium in D_2O-ice. The *c*-axis of the crystal is (i) 0°, (ii) 55°, (iii) 90° to the applied field.

fourth, and sixth moments were also calculated using the appropriate expressions. The results are tabulated in Table IV.2. In addition, from the second moment, the static dipolar relaxation time had been estimated using Equation 4.24. The static dipolar relaxation time is found to be dependent on the angle the c-axis of the crystal makes with the applied field and is at a minimum for $\theta \simeq 55°$. Therefore, the experimental relaxation rates should also be angular dependent with a maximum at $\theta \simeq 55°$.

Table IV.2.

Calculated second, fourth, and sixth moments for muonium in H_2O- and D_2O-single crystals. The position of Mu is taken to be in between two layers of oxygen nuclei.

For H_2O, $I = \frac{1}{2}$

Angle between applied field and c-axis	second moment (G^2)	fourth moment (G^4)	sixth moment (G^6)	relaxation time (μs)	relaxation rate (μs^{-1})
0	6.186	90.91	1822	0.057	17.46
10	7.144	133.6	3634	0.053	18.76
20	9.563	253.8	10355	0.046	21.70
30	12.61	437.5	23241	0.040	24.92
45	15.88	680.7	44138	0.036	27.96
50	16.25	711.4	47347	0.035	28.30
55	16.28	714.8	47415	0.035	28.31
60	15.92	690.5	45644	0.036	28.00
70	14.61	585.5	35658	0.037	26.83
80	13.23	471.3	25951	0.039	25.53
90	12.71	437.3	22692	0.040	25.01

For D_2O, $I = 1$

0	0.423	0.630	1.459	0.246	4.07
55	0.683	1.296	3.811	0.172	5.80
90	0.535	0.797	1.845	0.195	5.13

V. Non-bonding interactions of muonium in ice

1. Nature of the interactions

When two molecules or atoms are infinitely apart, their interaction energy is zero. When the two atoms/molecules are separated by a finite distance, r, the interaction energy provides an extra contribution to the total energy of the system. This contribution is commonly referred to as the intermolecular potential energy. The energy of this interaction between the two molecules arises from electric forces between the charged entities of which they are made up.

The general shape of the intermolecular force between two interacting particles consists of a strong repulsive force at short range and an attractive force at long range. In terms of potential energy, V(r), this behavior corresponds to large, positive energies at small separations and negative energies at long range. The two extreme regions are joined by a function with a single negative minimum.

2. Long range forces

The long-range forces are invariably attractive. There are three possible contributors to the long range forces: (a) electrostatic forces, (b) induction forces, and (c) London dispersion forces, depending on the nature of the interacting molecules. Only the London dispersion force is present in all intermolecular interactions. A short discussion for all three contributors will be given with emphasis on those which are of relevance to the present research.

A. Electrostatic forces

It is well known that some molecules such as HCl possess permanent electric moments by virtue of the electric charge distribution in the molecule. One component of the interaction energy for two such molecules at long range therefore arises from the electrostatic interaction between these moments. The contribution to the total potential will thus be:

$$V(\text{electrostatic}) = V(\mu\mu) + V(\mu Q) + V(QQ) + \ldots \qquad (5.1)$$

where the terms in parentheses denote the interactions between dipole moments, μ, quadrupole moments, Q, and so on. For muonium in an ice crystal, this kind of forces does not apply since muonium does not possess a permanent electric moment.

B. Induction forces

The electric field experienced by a molecule positioned at a point O due to a dipole $\bar{\mu}$ located at $\bar{r}$ is given by [42]:

$$\bar{E} = \{3(\bar{\mu}\cdot\bar{r})\bar{r} - r^2\bar{\mu}\}/r^5 \qquad (5.2).$$

Electric multipoles may be induced in the molecule by the electric field $\bar{E}$ by a distortion of its electron cloud. In the simplest case only a dipole moment is induced. The induced dipole is proportional and parallel to the field, so that [43]:

$$\bar{\mu} = \alpha(0)\bar{E} \qquad (5.3).$$

The scalar quantity $\alpha(0)$ is the static polarizability of the molecule which is assumed to be isotropic. The energy of a dipole, $\bar{\mu}$, in an electric field $\bar{E}$ is:

$$V = -\int_0^{\bar{E}} \bar{\mu}\cdot d\bar{E} \qquad (5.4).$$

Thus the energy of the dipole induced in a molecule with an isotropic polarizability by the field $\bar{E}$ is:

$$V = -\tfrac{1}{2}\alpha(0)\bar{E}^2 \qquad (5.5).$$

C. London dispersion Force

The London dispersion force is the only long range force which is present in all intermolecular interactions. For the interaction of two molecules possessing no permanent electric dipole or higher-order moments, the London dispersion force is the only interaction term. A molecule always possesses an instantaneous dipole moment because of motions of its electron cloud. This instantaneous dipole moment will induce an instantaneous dipole moment on another molecule [44]. The origin of the London dispersion force has been attributed to the interaction between these instantaneous dipole moments. So, the London dispersion force is also known as the induced-dipole induced-dipole interaction. There are also higher order contributions to the dispersion force arising from instantaneous dipole-quadrupole, quadrupole-quadrupole interactions *etc*. The dispersion energy can be written as [45]:

$$V = C_6/r^6 + C_8/r^8 + C_{10}/r^{10} + \ldots \qquad (5.6)$$

Generally, the higher order terms are neglected and only the r^{-6} term is retained. The C_6 term can be estimated from the Slater-Kirkwood expression [46]:

$$C_6 = \tfrac{3}{2}e^2\sqrt{a_0}\ \{a_1a_2/[\sqrt{(a_1/N_1)}+\sqrt{(a_2/N_2)}]\} \qquad (5.7)$$

where e is the electronic charge, a_0 is the Bohr radius, α_1 and α_2 are the polarizabilities of the interacting atoms, and N_1 and N_2 are the number of electrons in the outer sub-shell of the atoms. This expression was derived originally by using a variational approach. It is found to be identical to results obtained by using more sophisticated methods (*Padé approximants* and *moment theory*) [60].

3. Short range forces

When two molecules approach sufficiently close to each other, their electron clouds overlap. The Pauli Exclusion Principle prohibits the electrons from occupying the overlap region and so reduces the electron density in this region. The positively charged nuclei of the atoms are thus incompletely shielded from each other and, therefore, exert a repulsive force on each other. Such short range forces are also referred to as overlap forces. The effective range of this force is $\leq$ 3 Å. The quantum mechanical theoretical treatment of this problem would involve the wave functions of all the electrons involved. Methods such as: (a) *ab initio*, (b) Self consistent field (SCF), (c) Configuration interaction (CI), and combinations of these methods are generally used. However, these methods are mathematically complicated and calculations are time consuming and their results are very sensitive to geometry and the size of the basis set used [18]. Hence, empirical formulae are devised.

These empirical formulae generally have two terms: one for the short range repulsive force and another for long range attractive forces. The two most widely used expressions are the Lennard-Jones 6-12 potential function (L-J or 6-12) [47]:

$$V(r) = A_{12}/r^{12} - C_6/r^6 \qquad (5.8),$$

and the Buckingham potential function (6-exp) [48]:

$$V(r) = A \exp(-\rho r) - C_6/r^6 \qquad (5.9)$$

The two expressions are very similar - they both contain a r^{-6} attractive term and a repulsive term. The L-J expression has a r^{-12} dependence as its repulsive term while the 6-exp expression uses an exponential function to describe the repulsive energy.[1]

4. Intermolecular potential of muonium in an ice lattice

The characterization of the intermolecular potential of muonium/hydrogen in ice involves estimating the contributions from all the lattice nuclei. Eisenberg and Kauzmann [16] presented a set of empirical formulae for the intermolecular potential between two water molecules using the method described by Hendrickson [56]. They used Buckingham potentials to describe

[1] The Buckingham potential is generally accepted as a representation closer to reality because of its milder dependence on r at short distances [43].

the interactions between individual nuclei from one molecule with the nuclei of the other. The constants ρ were estimated from scattering of rare gases while C_6 were estimated by the Slater-Kirkwood Formula given in Equation 5.7. The values of constant A were calculated from the condition that $\partial V/\partial r$ must vanish at $r = r_0$, where r_0 is the sum of the *van der Waals* radii of the interacting nuclei.

In 1980, Benderskii *et al* [17] proposed an intermolecular potential for a hydrogen atom diffusing in an ice-lattice. Their potential function takes the form:

$$V(r) = A \exp(-\rho r) - C_6/r^6 \qquad (5.10)$$

where A, ρ, C_6 have the values of 3.5×10^2 eV, 3.6 $Å^{-1}$, and 4.1 eV $Å^6$ respectively. They constructed a potential by "meshing" the Buckingham potential supplied by Eisenberg and Kauzmann for the interaction between a hydrogen nucleus and an oxygen nucleus with the results obtained by Niblaeus *et al* [18] for the reaction:

$$H_3O\cdot \rightarrow H\cdot + H_2O \qquad (5.11).$$

Benderskii *et al* made the assumption that the interactions between the diffusing hydrogen atom and the lattice nuclei can be approximated by treating individual water molecules in the lattice as one entity instead of treating individual nuclei of

the molecule separately.

As the hydrogen atom diffuses along the channel, it is always closer to the lattice hydrogen nuclei than the oxygen nuclei because of the lattice geometry. Since the intermolecular potential is either r^{-6} or exp(-r) dependent, it is questionable whether the procedure used by Benderskii *et al* is valid.

In view of the questions mentioned above, an investigation into the intermolecular potential of muonium in ice was undertaken. The potential of interaction of muonium and the lattice atoms is assumed to be of the atom-atom type. Therefore, the intermolecular potential of muonium in ice consists of contributions from both the hydrogen and oxygen atoms in the lattice. In addition, the induction force exerted on muonium by the permanent dipoles of the water molecules in the lattice has to be included:

$$V(Mu) = V(H\text{-}Mu) + V(O\text{-}Mu) + V(induction) \quad (5.12).$$

The induction potential experienced by muonium from the dipoles of the water molecules was calculated. It is plotted as a function of the position of the muonium along the diffusion path in Figure V.1. The number of water molecules used in the calculation is 36. The calculation procedure involved summing up the total electric field gradient exerted on muonium by the 36 point dipoles using Equation 5.2. The induction potential was obtained by using Equation 5.5. The value of the static

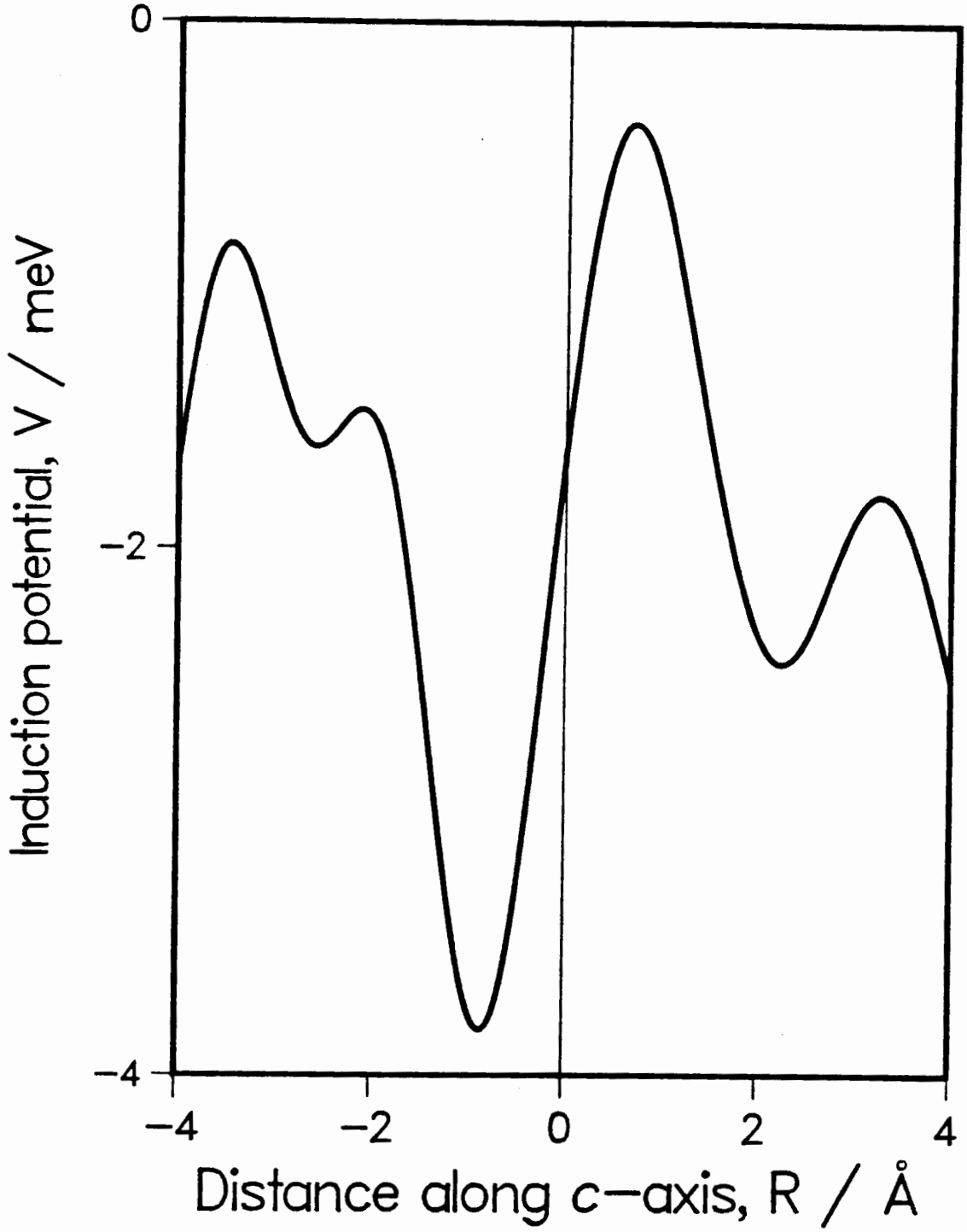

Figure V.1. Induction Potential of muonium as it diffuses along the channel parallel to the *c*-axis.

polarizability, $\alpha(0)$, of muonium was taken to be that of a hydrogen atom (5.36×10^{-25} cm^3) [61]. The value of the dipole, $\bar{\mu}$, is the same as in Equation 2.2 with its direction along the angle bisecting the H-O-H angle. Since the orientations of the hydrogen nuclei obey the Bernal-Fowler rules, the orientations of the dipoles are random. As can be seen in Figure V.1, the magnitude of the induction potential is small (peak to peak height is $\leq$ 3 meV). This is in agreement with results obtained for Mu/H in water by Klein *et al* [72]. Therefore, the induction contribution was not included in the calculation of the overall potential.

Following Eisenberg and Kauzmann [16], Buckingham potential functions (Equation 5.9) were used to represent the dispersion and overlap interactions between muonium and the lattice atoms. The values of ρ were not estimated from scattering of rare gases since more accurate quantum mechanical calculations are now available [62,63,64]. The values of ρ used were those calculated by Böhm and Ahlrichs [64]. They used first order SCF theory to estimate the exponential repulsive potential for nonbonded atoms in arbitrary states between closed-shell molecules (2.63 Å^{-1} for H-H and 3.13 Å^{-1} for H-O).

The dispersion coefficients used were calculated from the Slater-Kirkwood expression (Equation 5.7). The values of the static polarizability of the hydrogen and oxygen nuclei in the ice lattice were approximated by that of the hydrogen and oxygen nuclei in a hydroxyl group as recommended by Ketelaar [65]. The

calculated C_6's are 2.986 eV Å^6 for H-Mu and 5.443 eV Å^6 for O-Mu.[2]

Finally, the values of the coefficients A were calculated from the condition that the slope of the potential, *i.e.*, $\partial V/\partial r$, must vanish at the sum of the *van der Waals* radii of the interacting nuclei [16]. The *van der Waals* radius is defined as the distance between two atoms where the attractive forces just balance the repulsive force. Bondi [67] pointed out that the *van der Waals* radius of an atom depends strongly on its chemical environment. For example, the *van der Waals* radius of Xe in XeF_4 is 1.7 Å while the accepted value from solid xenon is 2.18 Å [70].[3] This point of view is supported by Huheey [71]. In the present case, the chemical environment of muonium is different from those of the lattice hydrogen. Since the literature value for the *van der Waals* radius of hydrogen was deduced from aliphatic compounds [67], it is not unreasonable to assume that the *van der Waals* radius of muonium is different. Klein *et al*

---

[2] Kolos and Wolniewicz [66] used variational method to calculate the energy function for the triplet state ($^3\Sigma^+$) of a free hydrogen molecule. Their results were fitted to an analytical expression and a value of 3.883 eV Å^6 for C_6 was obtained by Silvera [69]. The value of C_6 for two free hydrogen atoms as calculated by the Slater-Kirkwood formula is 4.218 eV Å^6. The difference can be explained by the inclusion of higher order dispersion terms (C_8 and C_{10}) in the analytical expression. Although the variational calculation is accepted as more accurate, the Slater-Kirkwood expression is used because of its simpler form and lack of data for the O-Mu interaction.

[3] In XeF_4 the xenon atoms do not touch each other. The *van der Waals* radius of xenon was estimated by subtracting the *van der Waals* radius of fluorine from the shortest non-bonded xenon-fluorine distance (3.2-3.3 Å).

[73] quoted a value of 1.8 Å for the *van der Waals* radius of Mu/H. They based their claim on the triplet state calculation for a free hydrogen molecule by Kolos and Wolniewicz [66]. However, Silvera [69] cited a value of 2.1 Å from the same reference. Inspection of the original literature indicated that the value quoted by Klein *et al* might be the Lennard-Jones radius [71] of Mu/H. Following Silvera [69], the *van der Waals* radius of muonium is taken to be 2.1 Å.

There are two sets of *van der Waals* radii for bonded hydrogen and oxygen available [64,67]. According to Bondi [67], the *van der Waals* radii for hydrogen and oxygen are 1.2 Å and 1.52 Å respectively. However, Böhm and Ahlrichs [64] calculated them to be 1.5 Å and 1.48 Å. In view of the controversy surrounding the definition and actual value of the *van der Waals* radius discussed earlier, both sets of radii were used to calculate the value of A. Hereinafter, the potential obtained from the Böhm and Ahlrichs parameters is called V_1 and that from Bondi V_2. For the sake of reference, the parameters supplied by Benderskii were used to calculate the potential V_3. A summary of the values for the coefficients used is tabulated in Table V.1.

The potential energy curves of V(H-Mu) and V(O-Mu) are shown in Figure V.2 as a function of the distance separating the two interacting particles. When Mu is between two layers of oxygen nuclei, it is $\simeq$ 3.2 Å away from each layer. As it diffuses, it is never closer than 2.6 Å from the lattice nuclei because of lattice geometry. Therefore, the portion of the

Table V.1

The values of parameters used in the

Buckingham potentials for V(H-Mu) and V(O-Mu)

Buckingham potential: $V(X\text{-}Y) = A \exp(-\rho r) - C_6/r^6$

Parameter	V_1(H-Mu)	V_2(H-Mu)	V_1(O-Mu)	V_2(O-Mu)
A (eV)	11.27	9.40	101.79	106.73
ρ ($Å^{-1}$)	2.63 †		3.13 †	
C_6 (eV $Å^6$)	2.986		5.443	

Other parameters used in the calculation

Parameter	V_1(H-Mu)	V_2(H-Mu)	V_1(O-Mu)	V_2(O-Mu)
r(vdW) (Å)	1.50 †	1.20 ††	1.48 †	1.52 ††

r(vdW) (Å) for diffusing Mu/H: 2.10 Å ‡

static polarizability, $\alpha(0)$ (cm^3)	4.2×10^{-25} (lattice hydrogen)	5.9×10^{-25} (lattice oxygen)

static polarizability for diffusing Mu/H: 6.6×10^{-25} cm^3

† From ref. [64]. ‡ From ref. [66]. †† From ref. [67].

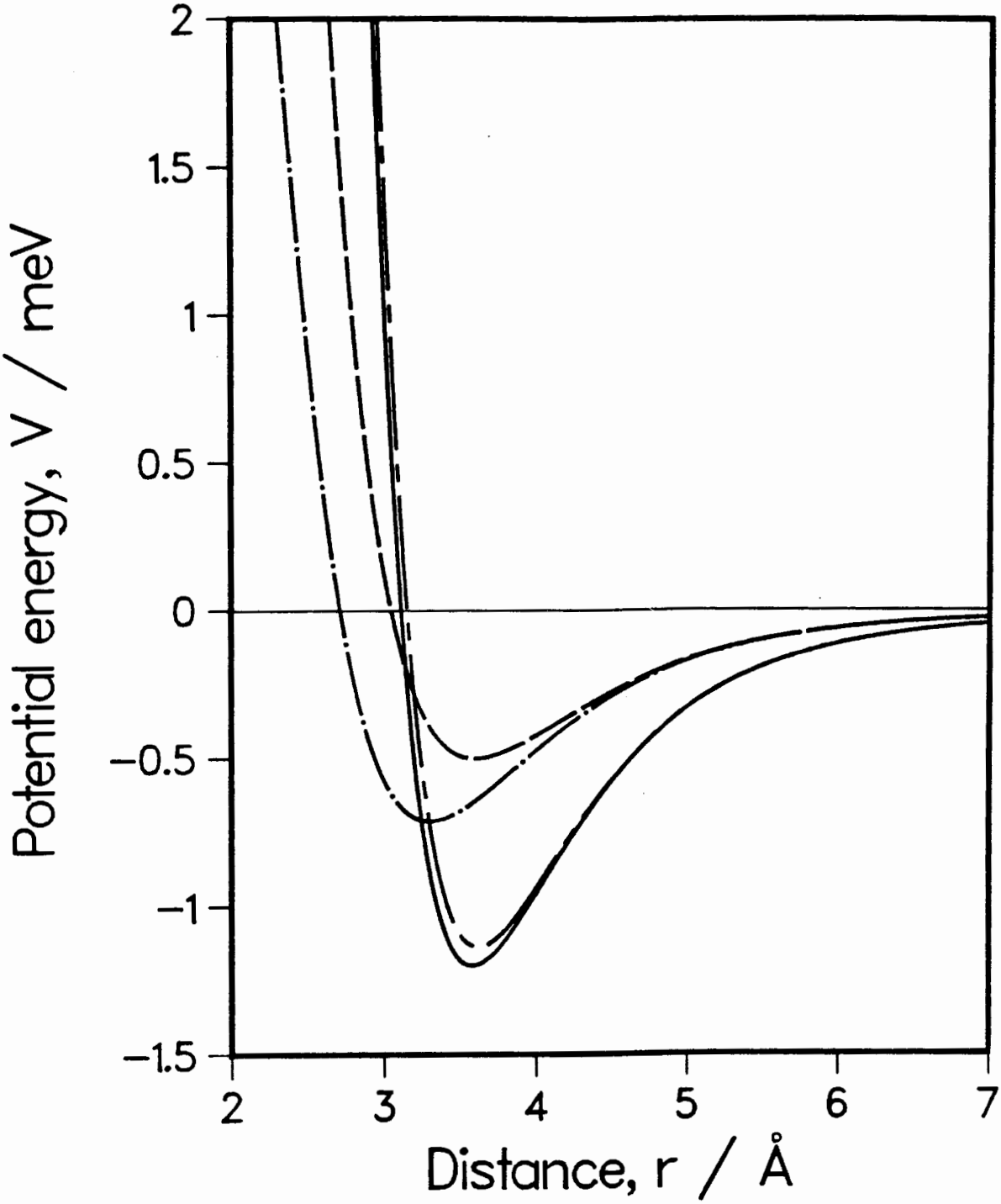

Figure V.2. The calculated Buckingham potential function for V_1(O-Mu) (solid line), V_1(H-Mu) (broken line), V_2(O-Mu) (chaindashed line), and V_2(H-Mu) (chaindotted line) as a function of the distance separating the particles.

potential from 2.6 Å to 3.2 Å is important for the present calculation. This implies that the choice of the *van der Waals* radii is critical since the potentials are at their turning points around these distances. If the radii chosen are too small, the potential that muonium experiences will always be attractive while the opposite happens if the choice is too large.

The total potential energy of muonium as a function of its location along the diffusion path was calculated by summing the potential energy contributions from each individual lattice nucleus using the respective expressions for the hydrogen and oxygen nuclei. The contributions from the hydrogen and oxygen nuclei to the intermolecular potential from the two sets of parameters (V_1 and V_2) are shown in Figure V.3.

The total potential energy of muonium as a function of its location along the channel parallel to the *c*-axis, R, is shown in Figure V.4. Also shown in Figure V.4 is the total potential energy of muonium as it diffuses along a zig-zag channel perpendicular to the *c*-axis. It can be seen clearly from Figure V.4 that the channel perpendicular to the *c*-axis is not favored energetically for diffusion because of its wider barrier width (lower permeability for quantum tunnelling) and taller barrier height (lower thermally activated diffusion rates). Therefore, it is not unreasonable to assume that muonium diffuses solely along the channel parallel to the *c*-axis.

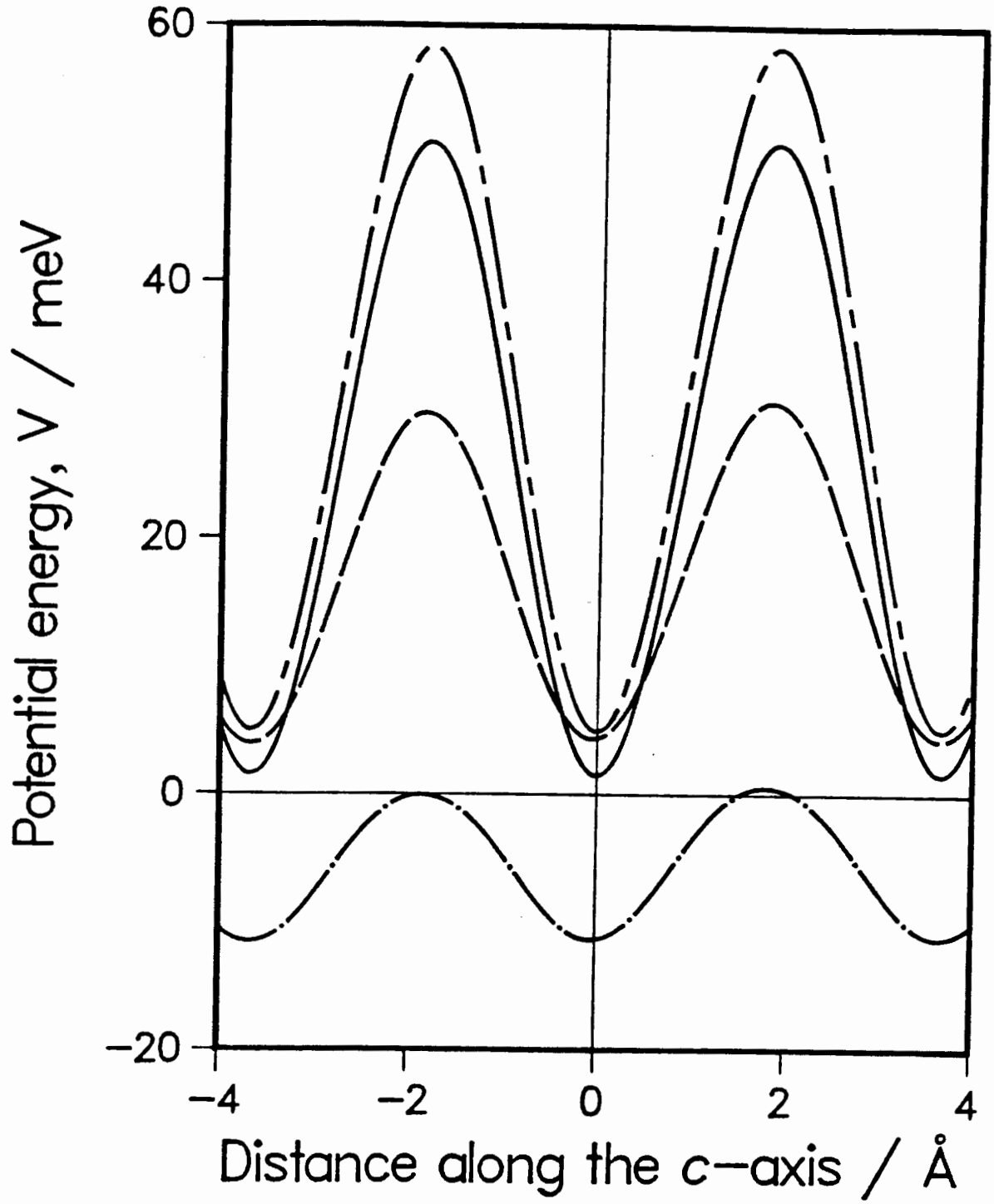

Figure V.3. Contribution to the potential from hydrogen and oxygen nuclei: (i) V_1(O-Mu) (solid line), (ii) V_1(H-Mu) (broken line), (iii) V_2 (O-Mu) (chaindashed), (iv) V_2(H-Mu) (chaindotted).

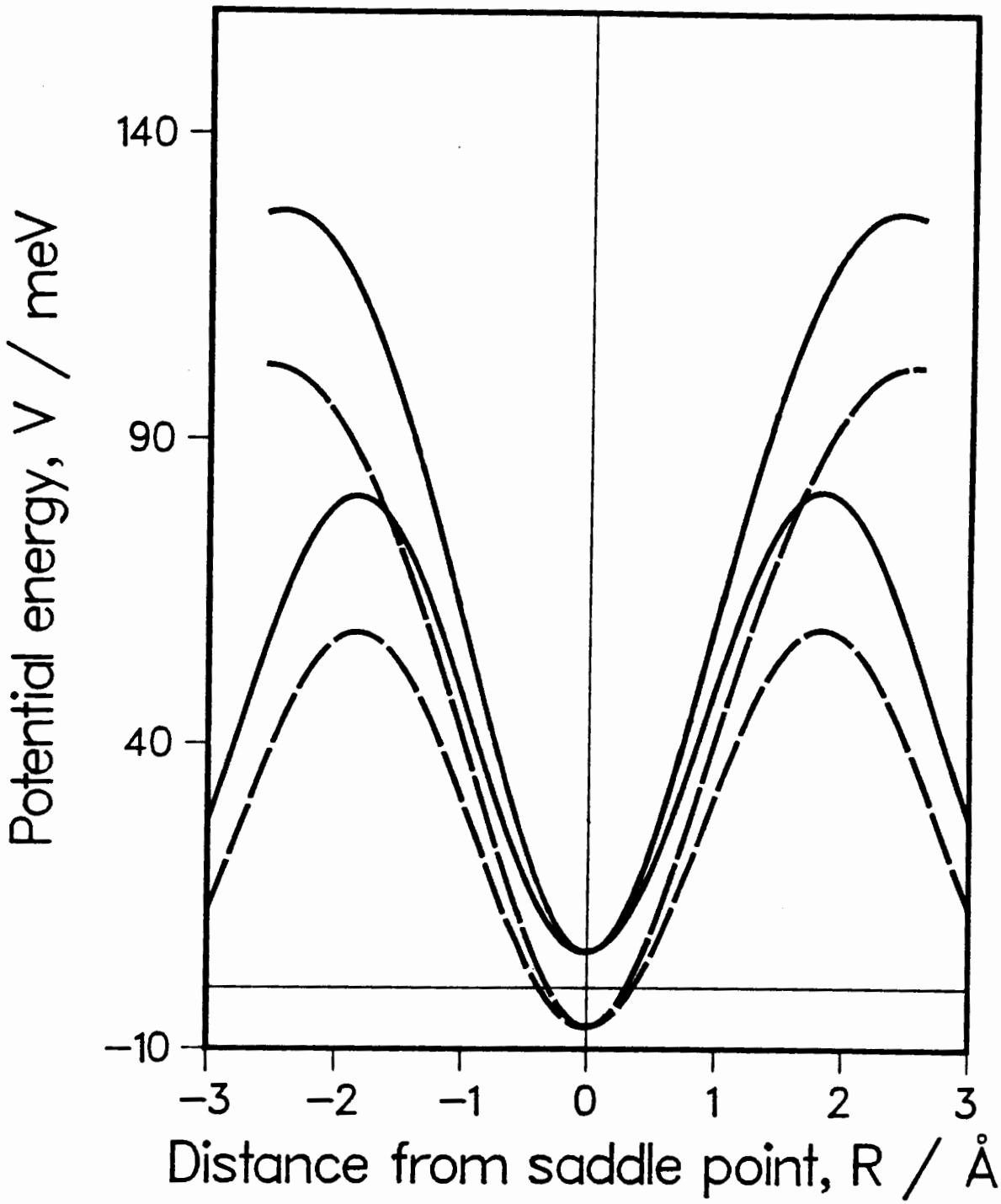

Figure V.4. The potential energy curve of muonium as a function of its location on the diffusion path: (i) along the channel parallel to the *c*-axis (lower curves), (ii) along a zig-zag path perpendicular to the *c*-axis (upper curves). Solid line are V_1 results and broken line are V_2 results.

5. Bound states for muonium and hydrogen in the intermolecular potential

The motion of muonium/hydrogen in the potential barrier has been approximated by a simple harmonic oscillator (S.H.O.) [68]:

$$V(R) = \tfrac{1}{2}m\omega^2R^2 \qquad (5.13)$$

where R is the distance the particle travels from its equilibrium position and ω is the oscillator frequency. The parameter m is the reduced mass of the system, and for the present case can be taken as the mass of the particle in the potential. The value of $\frac{1}{2}m\omega^2$ was found from the y-intercept of the best straight line with a slope of 2 through the linear portion of the log-log plot of V(R) versus R:

$$\log[V(R)] = \log(\tfrac{1}{2}m\omega^2) + 2\log(R) \qquad (5.14).$$

The values of ω for muonium and hydrogen for the two different sets of parameters and the potential of Benderskii *et al* are given in Table V.2.

The energy levels for muonium/hydrogen calculated in the S.H.O. approximation [68]

$$E = (n+\tfrac{1}{2})\,\hbar\omega \quad (n = 0,1,2...) \qquad (5.15)$$

are also tabulated in Table V.2. There is only one bound state found for muonium but three for hydrogen for all three potentials.[4] This is not unexpected since the mass of a hydrogen atom is 9 times that of muonium.[5]

Figure V.5 is a plot of the potential barriers calculated from the previous section with the S.H.O. approximation superimposed on one period.

---

[4] E_0 of Mu coincides with E_1 of H because of the inverse-root-mass dependence of ω ($m_H = 9m_{Mu}$) and $E_1 = 3E_0$.

[5] The value of E_2 for hydrogen is probably an over-estimate since the potential barrier deviates significantly from the S.H.O. at that region.

Table V.2

Comparision of parameters between muonium and hydrogen obtained from the simple harmonic oscillator approximation

Potential		ω (s^{-1})	E_0 (meV)	E_1 (meV)	E_2 (meV)
V_1	muonium	1.00×10^{14}	32.9		
	hydrogen	3.33×10^{13}	11.0	32.9	54.9
V_2	muonium	9.00×10^{13}	29.6		
	hydrogen	3.00×10^{13}	9.87	29.6	49.4
V_3†	muonium	1.5×10^{14}	45.0		
	hydrogen	5.0×10^{13}	15.0	45.0	75.0

† from ref. [17].

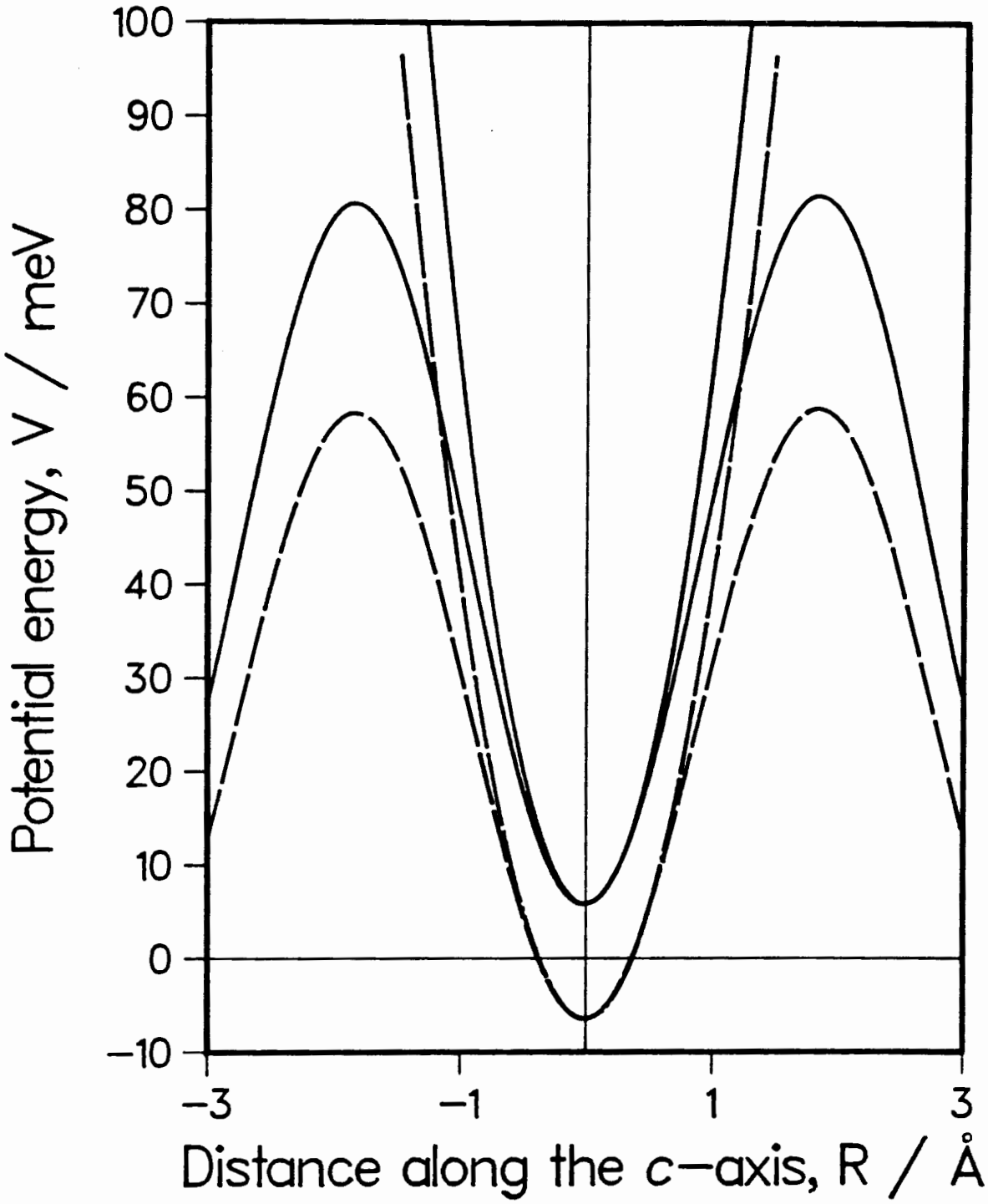

Figure V.5. The total potential function of Mu/H in ice with the simple harmonic oscillator. Results from V_1 are shown in solid line while those from V_2 in broken line.

VI. Diffusion mechanism of muonium and hydrogen in ice

1. Activated diffusion in ice

Classically, the thermally activated diffusion rate of a particle over a potential barrier is described by the Arrhenius Equation [74]:

$$D_A = D_0 \exp(-E_A/kT) \qquad (6.1)$$

where D_0 is the diffusion constant, E_A is the thermal activation energy and k is the Boltzmann constant. It is assumed that the diffusing atom oscillates from its equilibrium position with the frequency calculated from the simple harmonic oscillator model. The value of D_0 is calculated by [75]:

$$D_0 = g\,\omega / 2\pi \qquad (6.2)$$

where g is the number of saddle points surrounding the equilibrium site and ω is the oscillator frequency. For the present case, g is two, corresponding to diffusion "up" and "down" the channel. E_A is calculated from the separation between the energy levels and the maximum of the potential barrier. The activation energies calculated from the three different

potentials are tabulated in Table VI.1.

From statistical mechanics, the distribution of particles among allowed energy levels is given by the Boltzmann distribution [77]:

$$N_i = p_i \exp(-E_i/kT) \; / \; \sum_i p_i \exp(-E_i/kT) \qquad (6.3).$$

where p_i and E_i are the degeneracy and the energy of the $i-th$ level. For the present case, the value of p is 1 since there are no degenerate energy levels. The probability of finding the particle in a higher energy level is always less than that of the ground state. Therefore, the activated diffusion rates for each energy level have to be weighted by this Boltzmann factor. The total activated diffusion rates have been calculated at various temperatures for both muonium and hydrogen in the three potentials used. The results are given in Figure VI.1 in the form of $\ln(D_A)$ versus $1/T$. The activation energy determined from the slope of the linear portion of the plot is the same as E_{Ao}.

2. Quantum tunnelling in ice

Non-linear Arrhenius behaviour at low temperatures where the effect of the Boltzmann distribution is minor has been observed [76]. This can be explained by quantum tunnelling [86]. Although prohibited by classical theory, the probability of finding a particle bound in a potential in the adjacent saddle

Table VI.1

Activation energies for muonium and hydrogen for the three potentials.

(All units in meV)

	V_1	V_2	V_3 †
Muonium			
E_{A^0}	42.9	35.8	45.0
Hydrogen			
E_{A^0}	64.8	55.5	75.0
E_{A^1}	42.9	35.8	45.0
E_{A^2}	20.9	16.1	15.0
Peak to peak height of V:	75.8	65.4	90.0

†From ref. [17].

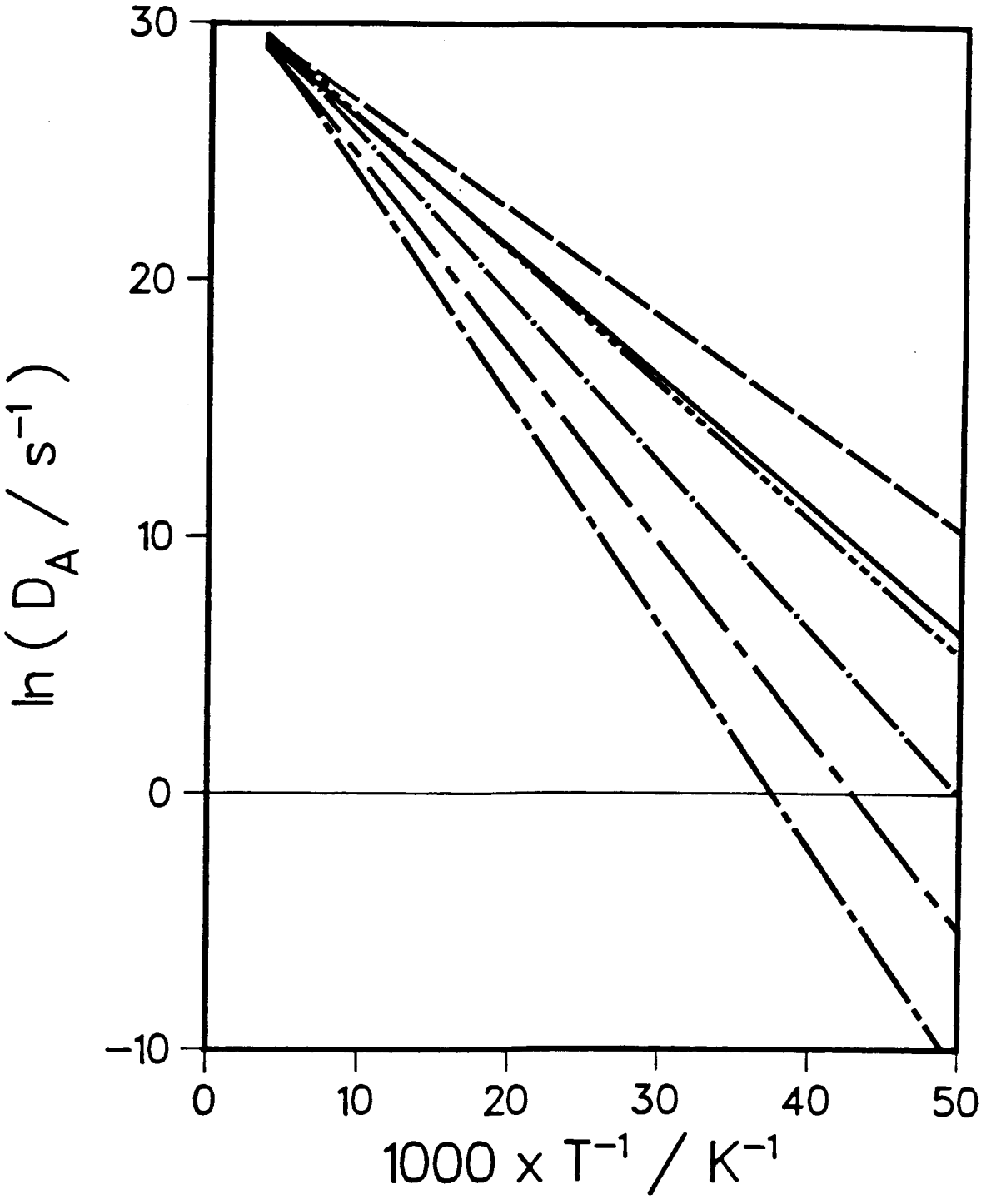

Figure VI.1. $\ln(D_A)$ of Mu from V_1 (solid line), V_2 (broken line) and V_3 (chain-triple-dashed line) and H from V_1 (chaindashed line), V_2 (chaindotted line), and V_3 (chain short dashed line) as a function of reciprocal temperature.

points is non-zero. This probability is called the "permeability" of the particle through the potential barrier and can be calculated using the BWK approximation.[1]

A computer program [88] formulated under this aproximation was used to calculate the permeabilities for the potentials. The results are given in Table VI.2. The permeability of the potential increases for higher energy levels. This is expected since the barrier width decreases towards the top. Therefore, the probability of hydrogen diffusion via quantum tunnelling is greatest for bound state E_2 and smallest for E_0.

The tunnelling rate of a particle in a potential barrier depends on the permeability, P, the oscillator frequency, ω, and the number of adjacent saddle points, g [78]:

$$D_T = g\,\omega\,P\,/\,2\pi \qquad (6.4).$$

where g and ω are the same as defined in Equation 6.3. The total tunnelling rate is a sum of the Boltzmann weighted tunneling rates from each individual energy level. For muonium in ice, this is temperature independent because there is only one populated level. For hydrogen in ice, the tunnelling rate is temperature dependent. A plot of the calculated $\ln(D_T)$ of hydrogen in ice as a function of inverse temperature is

[1] BWK approximation stands for the method for solving the Schrödinger equation for a bound system proposed almost simultaneously, though independently, by Brillouin, Wentzel, and Kramers. Other variations of the acronym are permutations of the letters: WKB, KWB *etc*.

Table VI.2

Calculated permeabilities for muonium and hydrogen in the different energy levels of the potentials using the BWK approximation.

	V_1	V_2	V_3
Muonium			
P_0	1.37×10^{-2}	2.17×10^{-2}	1.15×10^{-2}
Hydrogen			
P_0	3.04×10^{-10}	1.53×10^{-9}	4.18×10^{-11}
P_1	1.18×10^{-6}	4.13×10^{-6}	1.07×10^{-6}
P_2	1.85×10^{-3}	5.22×10^{-3}	6.87×10^{-3}

displayed in Figure VI.2. As can be seen from Figure VI.2, the tunnelling rate of hydrogen is constant in the low temperature regime (T < 40 K) but rises sharply when temperature is increased as the Boltzmann factor becomes important. At intermediate temperatures, the plot resembles that of a classical Arrhenius plot before it bends over to give a smaller slope at high tempeatures.

3. Effective diffusion in ice

The "effective" diffusion rate is a sum of the total activated diffusion rates and the total tunnelling rates:

$$D_E = D_A + D_T \qquad (6.5).$$

This has been calculated. The result is plotted in the form of $\ln(D_E)$ versus inverse temperature in Figure VI.3. The calculated effective diffusion rates for both muonium and hydrogen have temperature dependent and independent regions. The temperature dependent region is the manifestation of thermally activated diffusion. Quantum tunnelling dominates the temperature independent region. The intermediate region is a sum of the rates of the two mechanisms and exhibits the characteristic "bend-over" before it reaches the tunnelling limit. The effective activation energy is determined by the slope of the linear portion of Figure VI.3. This has been calculated and is

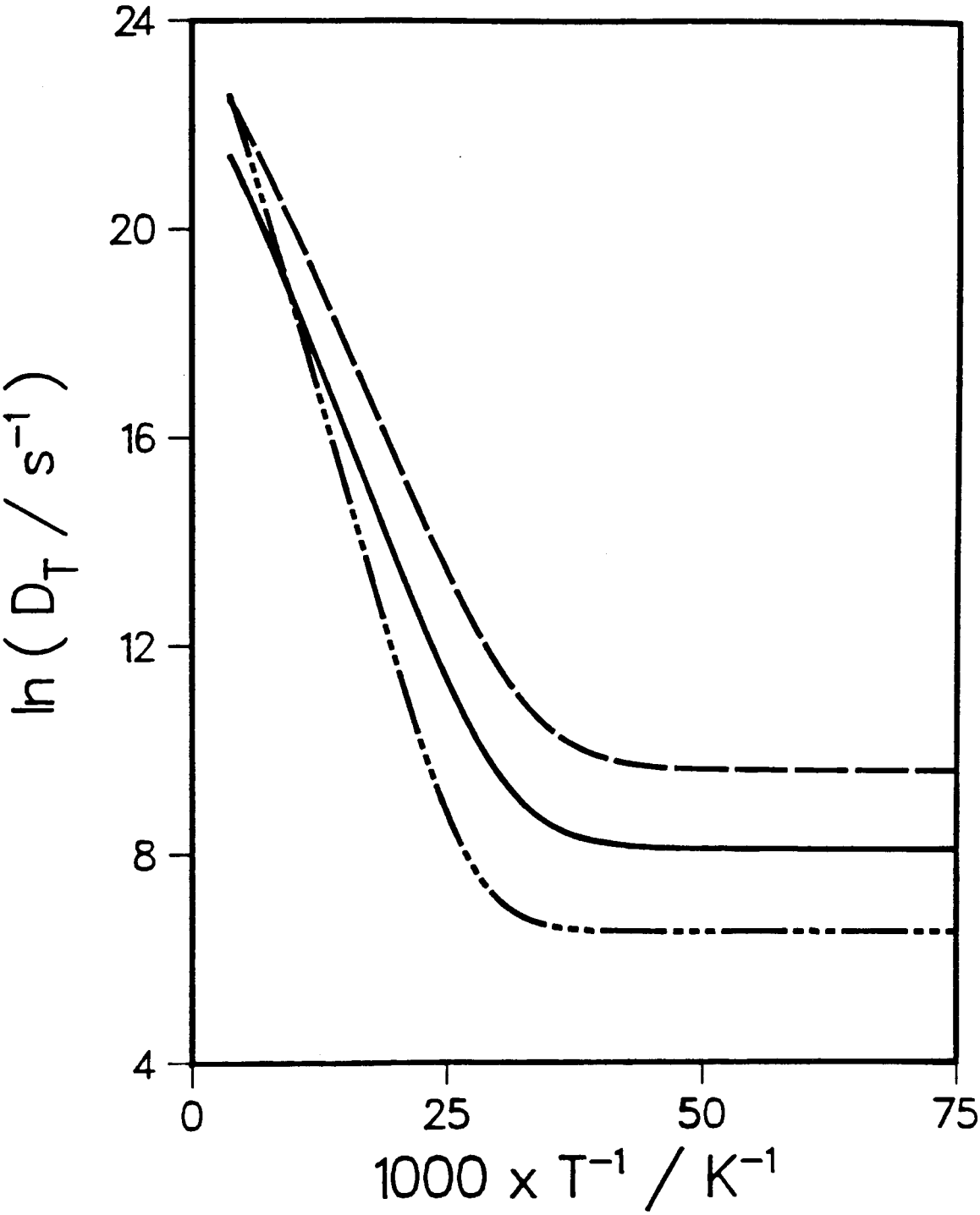

Figure VI.2. $\ln(D_T)$ of H in ice from V_1 (solid line), V_2 (broken line), and V_3 (chain-triple-dashed line) as a function of reciprocal temperature.

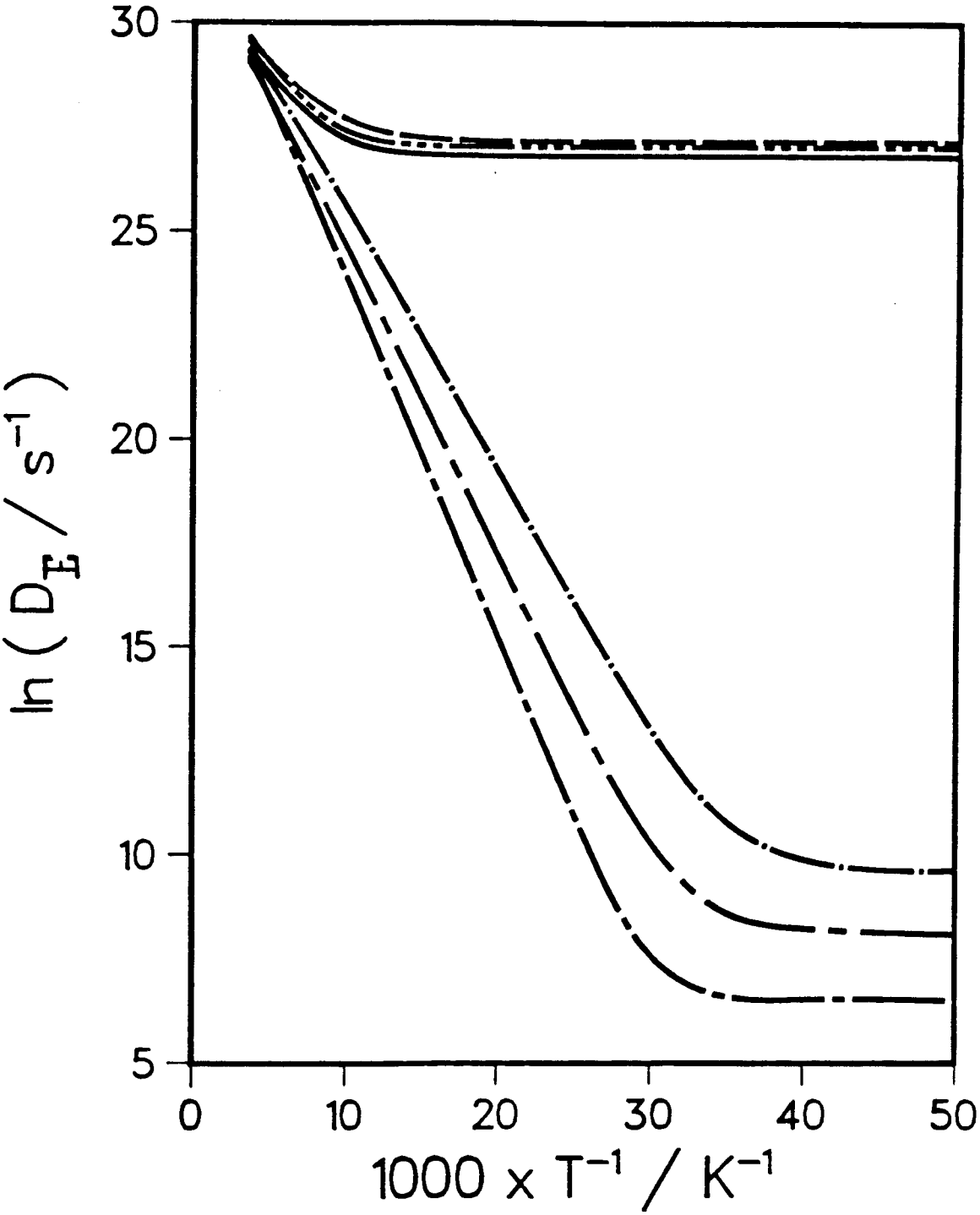

Figure VI.3. $\ln(D_E)$ of Mu from V_1 (solid line), V_2 (broken line) and V_3 (chain-triple-dashed line) and H from V_1 (chaindashed line), V_2 (chaindotted line), and V_3 (chain short dashed line) as a function of reciprocal temperature.

tabulated in Table VI.3. The effective activation energy of hydrogen in ice does not deviate significantly from that obtained by activated diffusion alone. However, that calculated for muonium does show a decrease of $\simeq$ 10% in the high temperature regime before it reaches the tunnelling limit.

In addition, the temperature where the tunnelling rate begins to exceed the activated rate (their cross-over point) is estimated and is also given in Table VI.3. Obviously, because of the inverse-root-mass dependence of D_A and D_T, the cross-over point of muonium is at much higher temperature than that of hydrogen.

Table VI.3

Calculated effective activation energies from the slope of the total diffusion rates

(All units in meV)

	Muonium	Hydrogen
V_1	37.5	64.6
V_2	31.0	53.9
V_3	39.8	74.7
Estimated temperature where tunnelling becomes dominant (Units in Kelvin)		
V_1	114	33
V_2	106	29
V_3	116	37

VII. Experimental methods

1. Sample preparation

Single crystals of H_2O- and D_2O- ice were grown by two separate methods. The first method was that outlined by Jona and Scherrer [50]. Several sets of thermostatically controlled heating coils were wound around a beaker at various levels. The beaker was then put inside a box with thermal insulation around it. Distilled and degassed water was poured into the beaker. The whole apparatus was placed in a freezer at -20°C. A temperature gradient was introduced by applying different electric currents through the different sets of coils around the beaker with the lowest current at the top. By slowly reducing the current in the individual coils in a controlled manner, it was possible to initiate and control the growth of an ice crystal from the surface downwards. It took 2 to 3 days for complete growth of a crystal. The single crystals produced by this method usually have their *c*-axis parallel to the length of the beaker.

The second method (mentioned by Jaccard [51]) was both faster and simpler. A capillary tube was drawn from a cylindrical beaker. Distilled and degassed water was poured into the beaker. The tip of the capillary tube was then seeded by dipping it into liquid nitrogen. The whole apparatus was then

slowly lowered into an ethanol bath at -20°C with the seeded tip of the capillary tube just touching the ethanol surface initially. The rate of descent was 6mm/hour. As the device was lowered into the bath, a single ice-crystal started to grow from the capillary tube upward. The *c*-axis of the crystal is usually perpendicular to the axis of the beaker. This whole process took about 1 to 2 days. Hereinafter, the crystals grown by the first method will be labelled crystals I and those by the second method crystals II.

Crystals II are of superior quality when compared to crystals I. The success rate of the second method was also much higher than that of the first. Both methods yielded cylindrical blocks of ice typically of the size 7 cm in diameter and 10 cm long. Good quality single crystals were carved from the centre of the blocks using a rotary cutting disc. They were subsequently polished with emery cloth and suede leather. The samples used in experiments were either cuboid or cylindrical in shape. The sides of the cuboid samples were approximately 4 cm. The cylindrical samples were 4 cm in diameter with a typical height of 4 cm.

The location of the *c*-axis of each crystal was determined by varying the orientation of the crystal with respect to polarized light. When the *c*-axis of a crystal is parallel to the polarized light, no light extinction should result from rotation of the crystal around its symmetry axis.

2. Cryostats

The prototype cryostat was essentially a double walled styrofoam box through which thermostatically controlled cold nitrogen gas was passed. Sample temperature was monitored by a silicon diode sensor (Lake Shore Cryotronics DT-500-DRC) held in contact with the sample surface at the edge of the expected muon stopping region. The lowest temperature attained by this cryostat was 88 K. The temperature gradient inside the cryostat was large. A second cryostat was constructed so that the 'exhaust' nitrogen gas was passed through an inner wall of the cryostat. The schematic drawing for this cryostat is given in Figure VII.1. By doing this, the lowest temperature attainable was 80 K and the temperature gradient reduced. The temperature stability was also improved.

However, some of the experiments required a cryostat which can reach temperatures down to 10 K. A 2-stage helium expansion cryostat was obtained (CTI-Cryogenics Model 21C Cryodyne Cryocooler). This He cryostat consists of a compressor and a cold head. Helium gas is compressed in the compressor and transported to the cold head. It is then allowed to expand in two stages in the cold head and, during the expansion, extracts heat from the cold tip. After expansion, the helium gas is returned to the compressor for recycling. The cold head was kept under vacuum. The sample was placed in thermal contact with the second stage cold tip. The temperature of the sample was

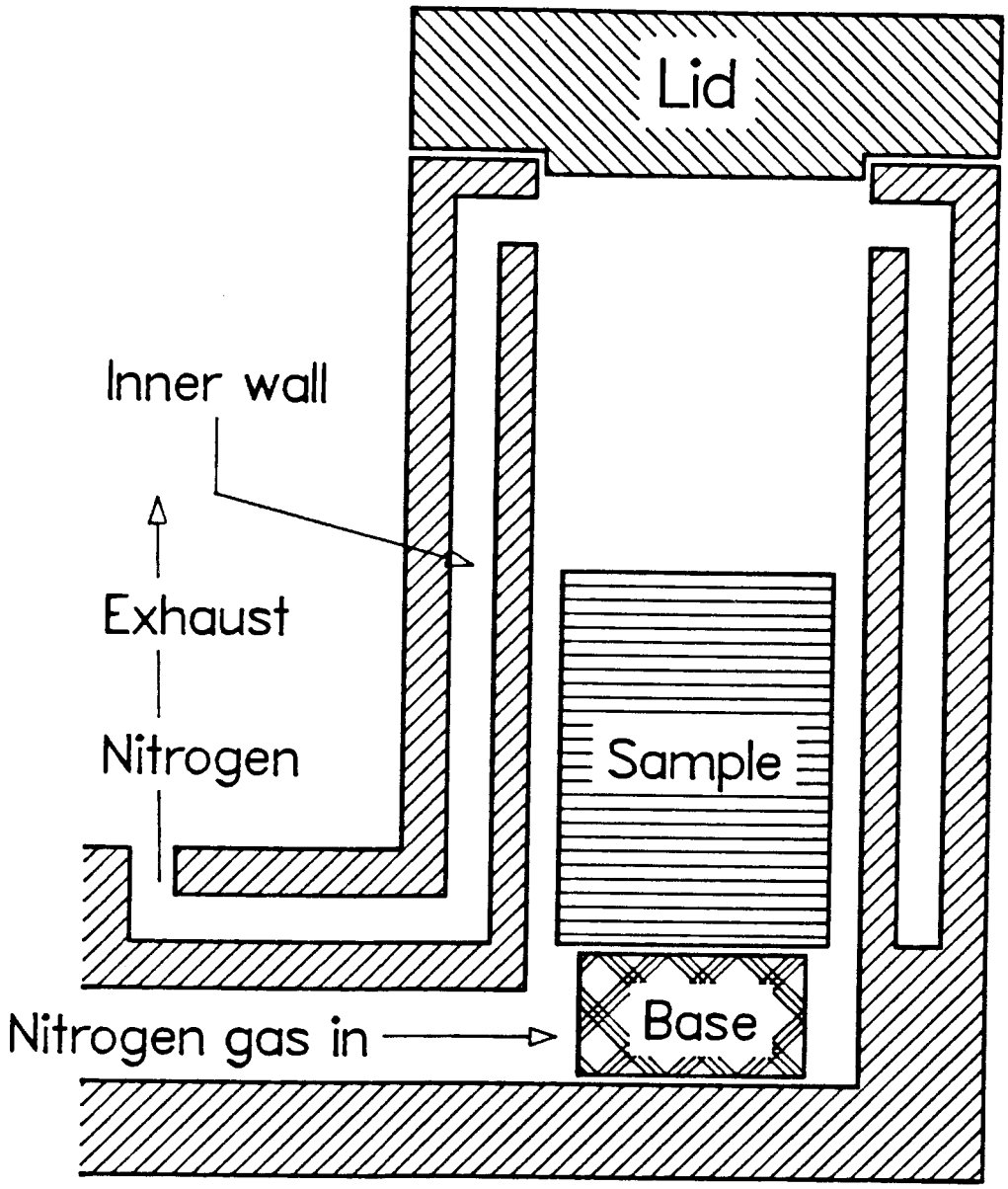

Figure VII.1. Schematic diagram of the nitrogen flow cryostat.

controlled by thermostatically controlled coils wound around the cold tip. The temperature sensor used was the same as that for the nitrogen flow cryostats. A shield with mylar sheet wrapped around the window was installed in order to block thermal radiation, which becomes important at low temperatures. Special precautions such as applying thermally conducting grease between the sample and the cold tip and making sure the sample was not in thermal contact with the radiation shield had to be taken to ensure the stability of temperature and to minimize the temperature gradient in the sample. The schematic diagram of this cryostat is shown in Figure VII.2. The lowest temperature attained with this cryostat was 8.0 K. The stability of this cryostat is extremely good. For a 2 hour experiment, the temperature drift was no more than 1 K at high temperatures and much less at low temperatures.

3. μSR experiments

Experiments were performed at the M20A beam line of TRIUMF, using the conventional transverse field muon spin rotation (μSR) technique. The apparatus used was SFUMU,[1] which consists of a set of Helmholtz coils, a water degrader and various collimators. The sample was placed in the cryostat. The cryostat was mounted onto SFUMU with the sample volume in the middle of

[1] SFUMU, as its name suggests, stands for the Simon Fraser University MU spin rotation group. Although SFUMU nominally belongs to the SFU group, it is shared with other TRIUMF users.

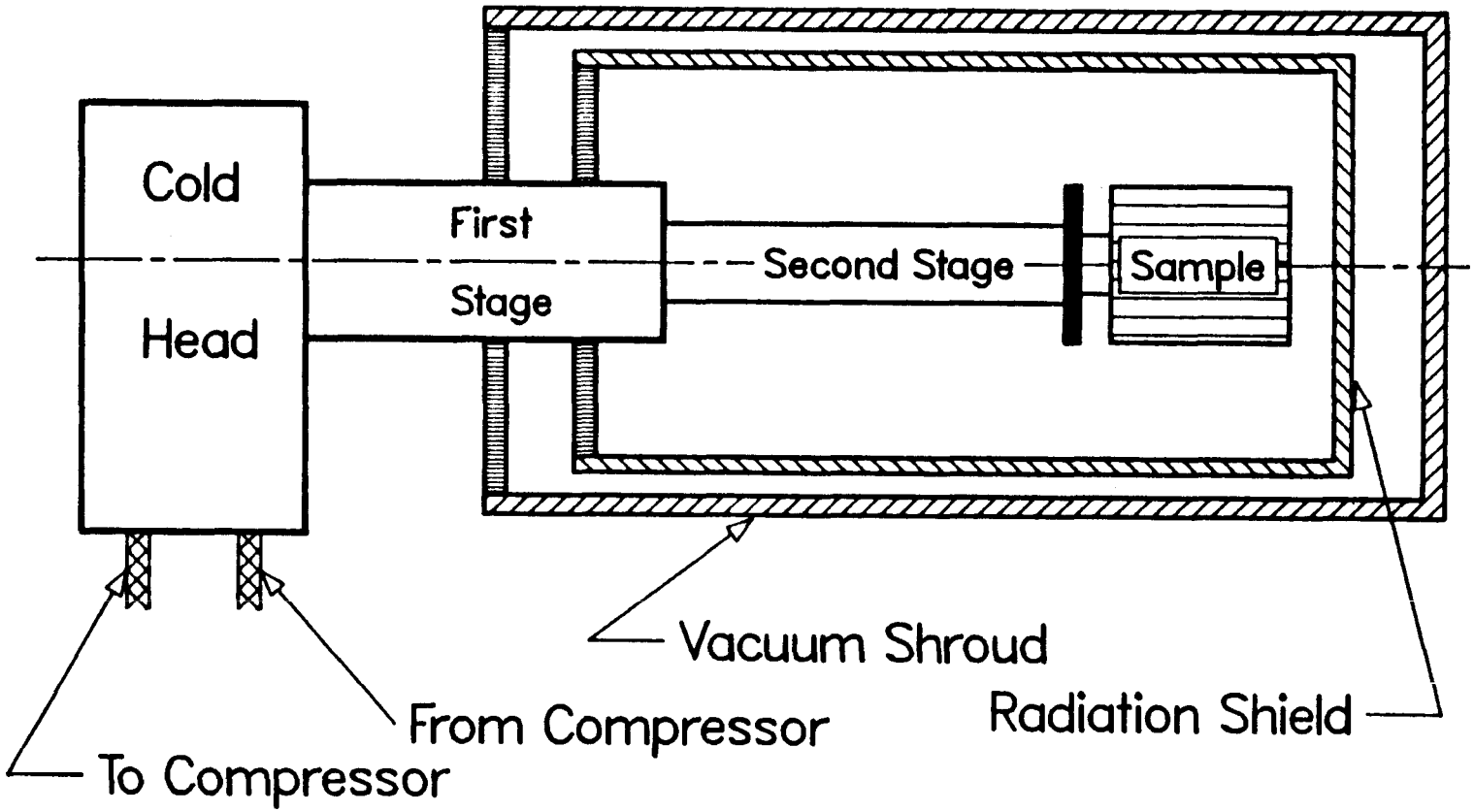

Figure VII.2. Schematic representation of the helium flow cryostat. Helium from the compressor is allowed to expand in the cold head in 2 stages and extract heat from the cold tip in the process. The gas is then returned to the compressor for recycling.

the Helmholtz coils where the field inhomogeneity is least. The whole apparatus was aligned with the beam. A beam of longitudinally polarized backward muons (μ^+) with momentum of 88 MeV/c in the laboratory frame of reference was introduced to the sample. The momentum of the muons was sufficient to ensure that the muons penetrated the cryostat walls and irradiated the target sample. The thickness of the water degrader was varied remotely to moderate the momentum of the muons and optimize the stopping site of the muons. With a final beam collimator of 20 mm in diameter the muon stopping rate was typically 2×10^4/s. Three positron telescopes, arranged in forward, backward and perpendicular directions with respect to the muon beam, were used at first. At a later experimental stage, a fourth telescope was installed in the other perpendicular direction. The experimental set-up is given in Figure VII.3.

The ratio of the muon precession amplitudes detected by the forward and backward telescopes was used to optimize the water degrader setting. As a rule of thumb, the optimum muon stopping distribution was achieved when the muon precession amplitudes detected by the forward and backward telescopes were equal provided the sample was placed midway between the two detectors. This method was found to be more sensitive than other commonly used criteria such as the perpendicular telescope counting rate or the ratio of muon stops to beam intensity.

For the experimental set-up to register a muon stop in the sample, the muon must pass through counters B, M_1, M_2 but not

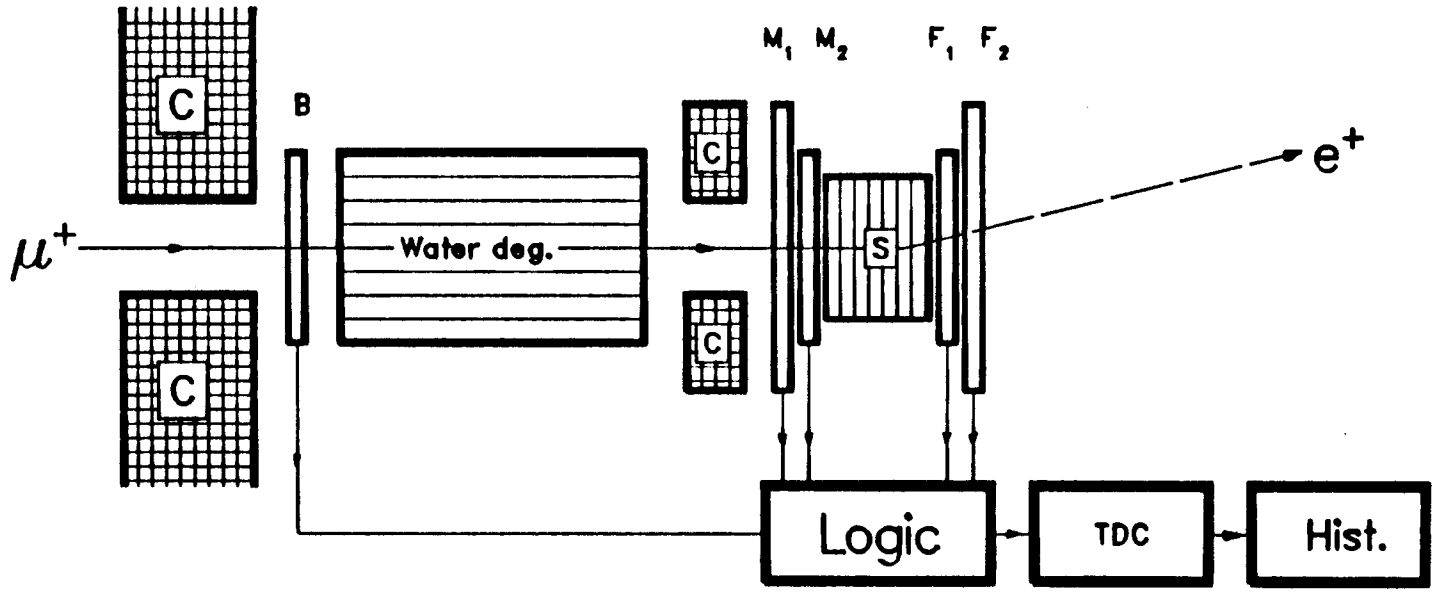

Figure VII.3. Schematic representation of a μSR experimental assembly. Individual muons pass through the collimator, slow down in the degrader, and stop in the sample where they decay and emit a positron.

F_1. Therefore, the muon stop signature is $B.M_1.M_2.\overline{F}_1$. Correspondingly, $\overline{M}_2.F_1.F_2$ represents a decay of a muon in the forward direction. The two signatures form the start and stop signals for the life-time counting apparatus. The standard data acquiring system of TRIUMF was used. The elapsed time between muon stop and its decay (signalled by the emission of a positron) was measured with a 1 GHz digital clock (TRIUMF B080) at first. A pileup gate was used to reject events for which two muons had entered the target within the gate time, which for a typical muonium experiment, was set at 8 μsec, to reduce the distortion of the μSR spectrum. During September 1984, a new clock (Lecroy Camac 4024 TDC) was installed in place of the old clock. The resolution (.1 ns) of the new clock is better. The electronics is simplified because multiple stops of the clock are rejected. The data are collected in three/four histograms (N versus t) corresponding to the three/four positron telescopes. For lower field muonium experiments, each histogram contains 2048 bins of 4 ns width. For higher field (70 G) experiments, the bin width was decreased. 6-8 million events per histogram are accumulated for a muonium experiment. Under typical beam intensities and stabilities, the whole experiment takes $1\frac{1}{2}$-2 hours.

4. Data analysis

The μSR histograms were analyzed by computer fitting of the appropriate theoretical function. The general form of a histogram is:

$$N(t) = B + N_0 \exp(-t/\tau) [1 + A(t)] \qquad (3.3)$$

where B represents background, N_0 is the normalization factor, τ is the muon life time, and $A(t)$ is the muon asymmetry. For ice, $A(t)$ is a sum of the diamagnetic and muonium precession signals:

$$A(t) = D(t) + M(t) \qquad (7.1).$$

The diamagnetic signal is given by:

$$D(t) = A_D \exp(-\lambda_D t) \cos(\omega_D t + \phi_D) \qquad (7.2),$$

i.e., a simple oscillation characterized by amplitude (A_D), relaxation rate (λ_D), frequency (ω_D) and phase (ϕ_D). Two different expressions were used to fit the muonium signal, $M(t)$, depending on the strength of the applied field and the orientation of the *c*-axis of the single crystal with respect to the applied field. For a single frequency,

$$M(t) = A_M \exp(-\lambda_M t) \cos(\omega_M t + \phi_M) \qquad (7.3)$$

and for split muonium precession,

$$M(t) = \tfrac{1}{2}A_M \exp(-\lambda_M t)\,[\cos\{(\omega_M - \tfrac{1}{2}\delta)t + \phi_M - \delta_0/2\} + K_A \cos\{(\omega_M + \tfrac{1}{2}\delta)t + \phi_M + \delta_0/2\}] \qquad (7.4).$$

The splitting parameter δ can incorporate both the Zeeman splitting and the hyperfine anisotropy. The former also affects the relative amplitudes of the amplitude components. K_A is the ratio of the amplitudes of the muonium frequencies with δ_0 the phase difference between the frequencies. At higher fields, *e.g.*, 70 G experiments, this effect is important.

For experiments done with an applied field of less than or equal to 10 Gauss and with the sample oriented 55° to the applied field, expression (7.3) was used to fit the histograms since the Zeeman splittings were small. For experiments done with an applied field of 37 Gauss and with the *c*-axis of the sample parallel to the applied field, expression (7.3) was also used since the Zeeman splitting offsetted the splitting caused by the anisotropic hyperfine tensor. All other data obtained from various experimental conditions were fitted with expression (7.4). The slow precession of the diamagnetic muon, was accounted for by Equation 7.2, in which ω_D is related to ω_M by a constant factor describing their gyromagnetic ratios ($\gamma(Mu)/\gamma(\mu^+) = 103$). Thus, for the most complicated case, split muonium precession (*e.g.* 70 Gauss experiments), 12 free fit parameters (B, N_0, A_D, λ_D, ϕ_D, A_M, λ_M, ω_M, ϕ_M, δ, K_A, δ_0) are

required.

Examples of the three types of signals are given in Figure VII.4 for muon and muonium in a D_2O-xtal. All fits were made to the full histogram, $N(t)$, but for clarity, the muon decay has been divided out.

The computer program used was MINUIT, written by James and Roos [52]. It involves a non-linear least-square minimization procedure to fit a theoretical expression to experimental data and calculate the parameter errors and correlations.

5. Calibration procedures

The signal amplitudes A_D and A_M were converted to muon polarization fractions P_D and P_M by calibration against A_D for standard samples run in identical apparatus configurations [53]. The standard samples included aluminum foil and ferric oxide powder made into the same shape, size and weight as the real ice samples. Ferric oxide does not give rise to any signal at the observed ω, so $A_D(Fe_2O_3)$ is attributed to the background signal due to muon stops outside the sample. Aluminum is used as a standard because it gives full asymmetry at ω_D. Then the polarization is given by [54]:

$$P_D = [A_D(ice)-A_D(Fe_2O_3)]/[A_D(Al)-A_D(Fe_2O_3)] \quad (7.5)$$

$$P_M = 2A_M(ice)/[A_D(Al)-A_D(Fe_2O_3)] \quad (7.6).$$

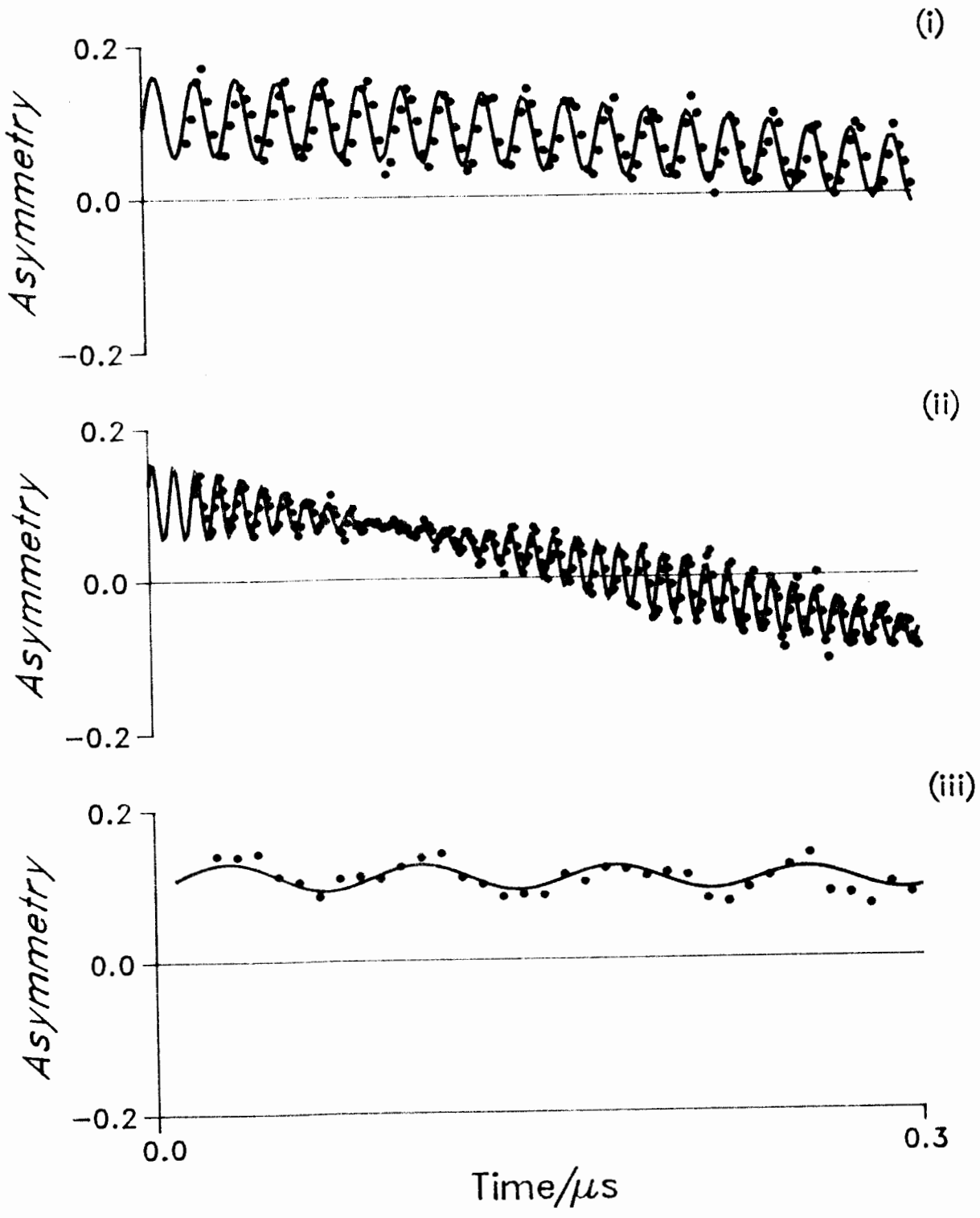

Figure VII.4. μSR spectra of muonium in D_2O ice: (i) 0° orientation, 37 G, 209 K. (ii) 0°, 70 G, 209 K. (iii) 55°, 10 G, 95 K.

The factor of 2 in P_M accounts for the unobserved fraction of muonium in the singlet state [54]. The polarizations obtained for each histogram were then statistically averaged:

$$\langle P \rangle = \sum_i (P_i/\Delta P_i^2) \; / \; \sum_i (1/\Delta P_i^2) \qquad (7.7).$$

The temperatures measured by the silicon diode sensor were calibrated against various standard temperature baths [55]. The deviations of the temperatures recorded by the silicon diode sensors were found to be no more than 1 K off the standard bath temperatures in the high temperature regime. A plot of the deviations as a function of bath temperatures exhibits a staight line. Extrapolation of the straight line indicated that, in the low temperature regime, the deviation is minimal. Since only the relative errors are important, the temperatures measured by the silicon diodes are taken to be absolute.

The relaxation rates obtained for each histogram were also statistically averaged in the manner of Equation 7.7. The averaged relaxation rates contain contributions from both dipolar interactions and field inhomogeneities. The contribution from field inhomogeneities has to be subtracted from experimental relaxation rates. The calibration procedure for this was more complicated and is discussed in the next section.

Another factor which can cause anomalous relaxation rates is applied field instability. If the applied field strength is not stable, the Larmor precession frequency of muons would be

different at different points in time. This will cause dephasing of the muonium spins and will result in an apparent relaxation of the signal. The effect of this is not distinguishable from field inhomogeneity effects. Therefore, its effect is taken to be incorporated in the field inhomogeneity corrections.

6. Field inhomogeneity corrections

If the applied field in a μSR experiment is not homogeneous, the precession frequencies of individual muons and muonium would be different. This arises because individual muons and muonium will experience different field strength depending on the stopping site. The effect of this will be depolarization of the muon spins and an increase of the transverse relaxation rate. Field inhomogeneity has two origins: the inherent magnetic field gradient of the helmholtz coils used and the presence of paramagnetic materials around or near the sample which alter the effective magnetic flux experienced by the sample. Another minor contribution to the field inhomogeneity is the change of the magnetic environment caused by other dipole, quadrupole and hexapole magnets of the beam lines, and the magnetic field of TRIUMF. The effect of this contribution is random field inhomogeneity because it depends on the environment. The correction of this effect is incorporated into the correction of field inhomogeneity.

Measurements have been made to estimate the effect of the former two contributions. It was found that the field inhomogeneity caused by the Helmholtz coils on the SFUMU apparatus was minimal. The relaxation rates observed by a μSR experiment is a sum of all the different relaxation rates, *i.e.*,

$$T_2^{-1}(\text{obs}) = \sum_i T_{2i}^{-1} \qquad (7.8).$$

In aqueous environment (water), muonium is diffusing rapidly while the water molecules are also rearranging themselves rapidly, the relaxation rate caused by dipolar interaction is motionally averaged and is negligible. Therefore, the origin of the observed relaxation rates of muonium in water ($0.186^{+0.056}_{-0.054}$) can be attributed to field inhomogeneity of the coils. If no other cause for field inhomogeneity was present, relaxation rates obtained at lower temperatures must be corrected by this amount in order to determine the true relaxation rate caused by dipolar interaction. The styrofoam cryostats used at the beginning of the research contain no paramagnetic materials and therefore did not contribute to the field inhomogeneity. Therefore, the experimental relaxation rates were corrected by subtracting the relaxation rates obtained for muonium in water.

The Helium cryostat, however, did alter the magnetic flux around the sample. When the cryostat was first designed, the radiation shield was plated with Nickel while the vacuum shroud was made of steel. After the maiden application of the cryostat

(January 1984), it was found that the relaxation rates measured were anomalously high when compared with results obtained by using the styrofoam cryostats. Hence, an investigation of the magnetic flux contour for the sample volume was initiated. The contours of the magnetic flux for a cross-sectional plane perpendicular to the applied field and bisecting the sample are plotted in Figure VII.5. In Figure VII.6, cross-sections of the field along and perpendicular to the direction of the field right through the middle of the sample for an applied field of 10 Gauss are plotted. From this plot, the field inhomogeneity of the applied field is evident. The variation of this inhomogeneity as a function of applied field after the inaugural use of the He cryostat is given in Figure VII.7. In view of this field inhomogeneity effect caused by the cryostat, a set of experiments done with different applied field intensities at the same temperature ($T > 220$ K) were performed for each subsequent beam periods to serve as calibration.

After the first usage of the He cryostat, the radiation shield and vacuum shroud were reconstructed using copper. The relaxation rates obtained during the second usage of the cryostat (May 1984), were still higher than those obtained from the Nitrogen flow cryostat. This anomalous behavior was caused by the plating on the cold tip of the cryostat. The plating was subsequently sanded away.

For the beam periods in November, 1984 and May, 1985, a new sample holder, radiation shield, and vacuum shroud were used.

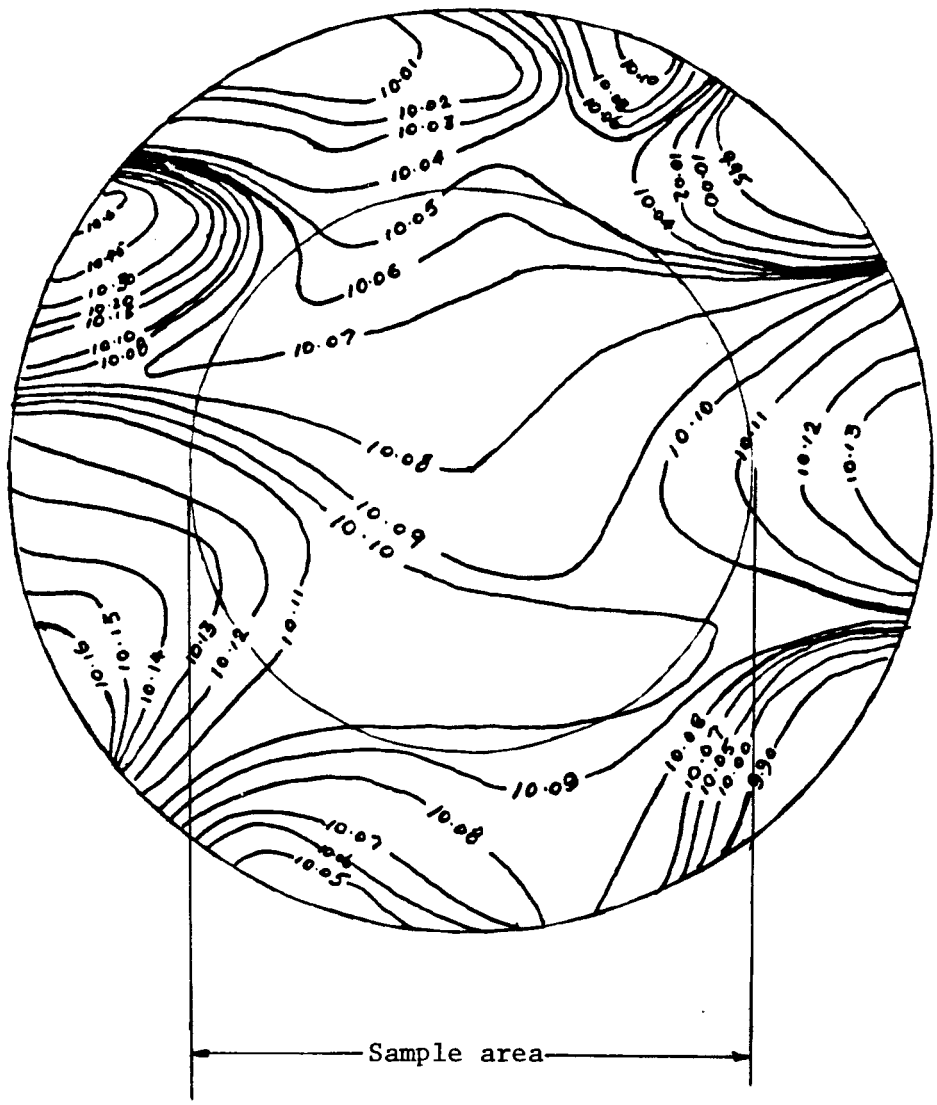

Figure VII.5. Contours of magnetic field intensity inside the radiation shield and vacuum shroud of the He cryostat. The applied field is 10 G.

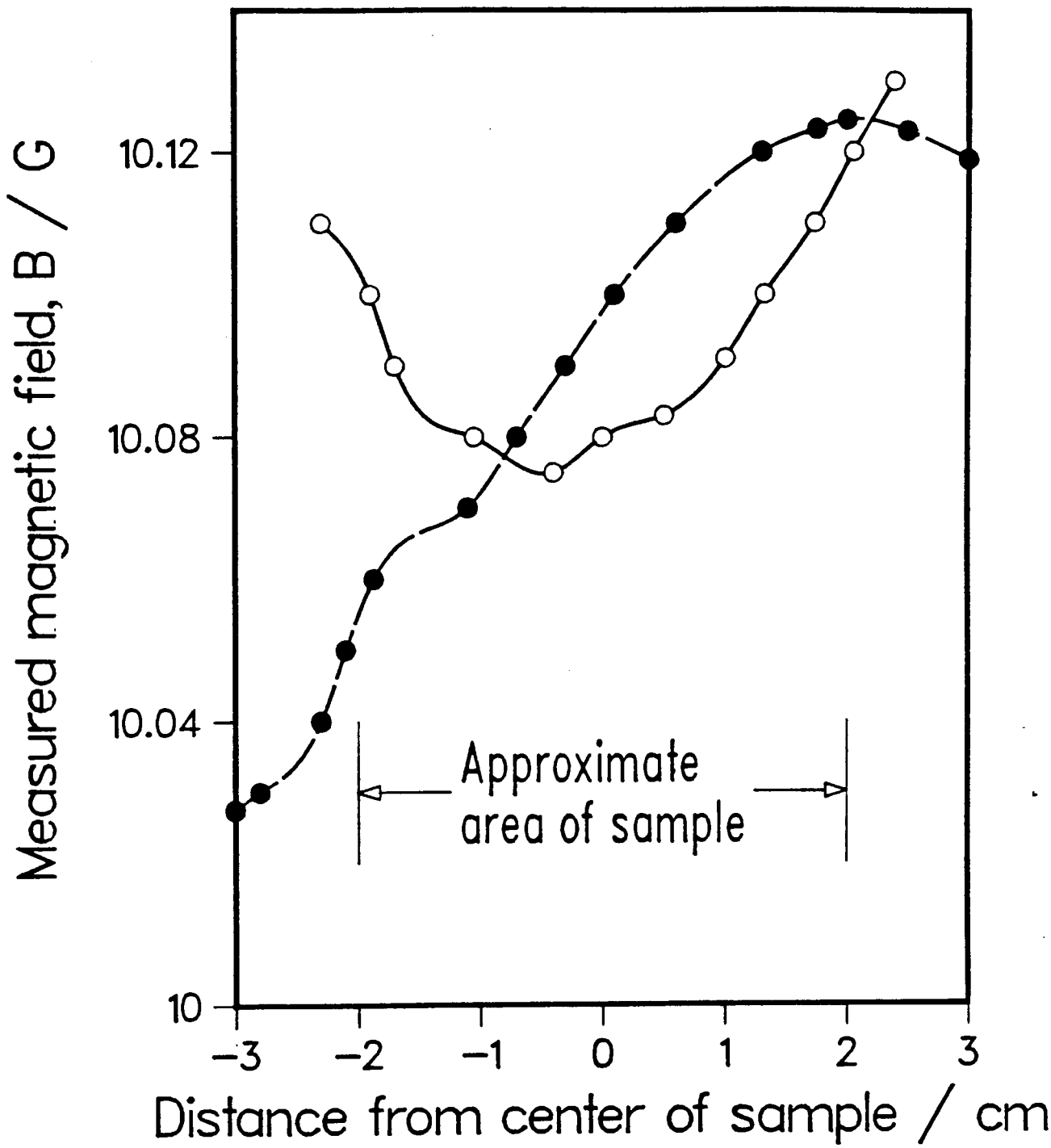

Figure VII.6. Magnetic field intensities as a function of position at the sample area parallel (●) and perpendicular (o) to the applied field of 10 G.

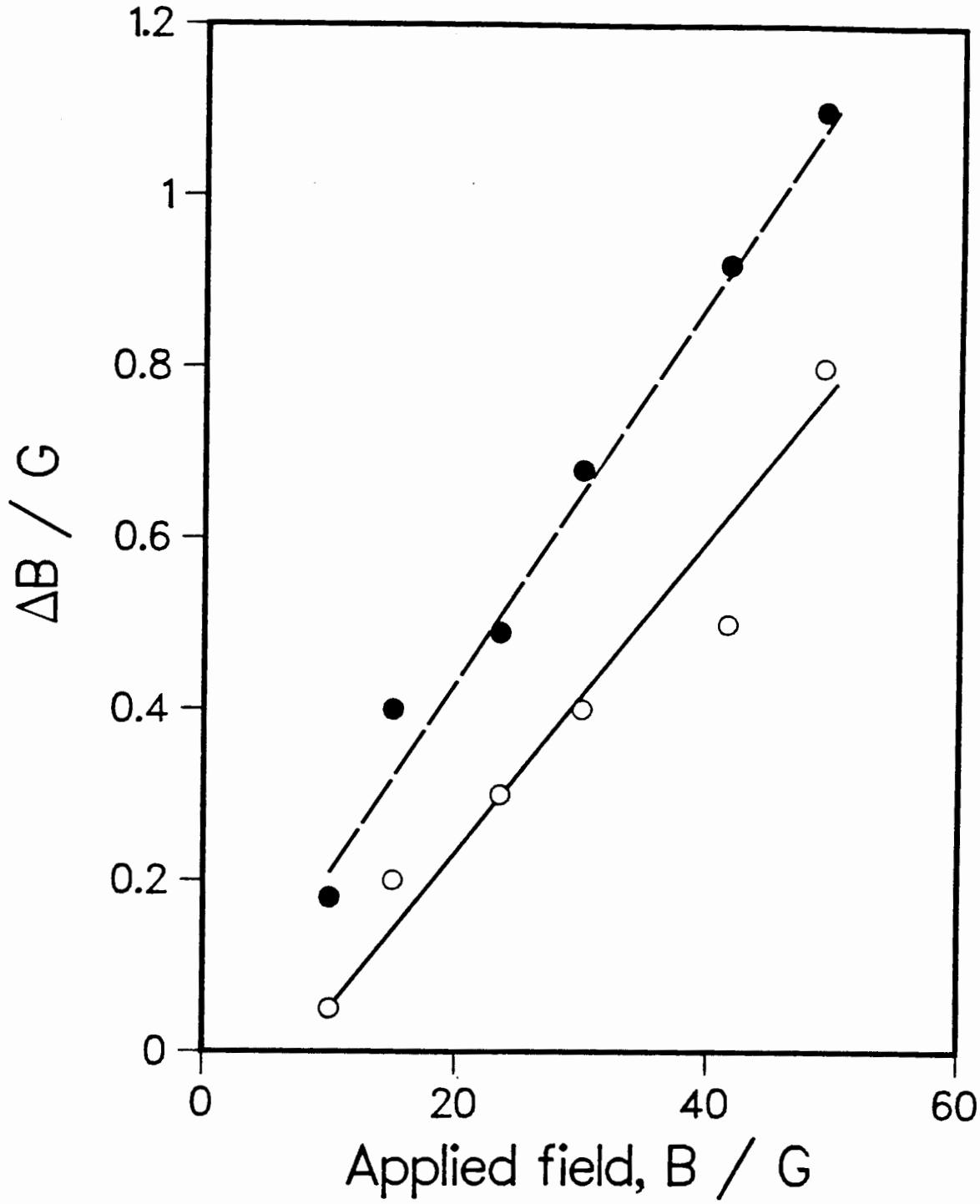

Figure VII.7. Field inhomogeneity as a function of applied field strength. ● is for measurements in the direction of the field and o is perpendicular.

The new sample holder was designed such that the sample volume is farther away from the cold tip. This way, the field gradient caused by any remaining paramagnetic material in the cold tip will be minimized.

In view of the previous discussion, the experiments performed inside the He cryostat were corrected using four different methods corresponding to the four stages of the development of the cryostat. They are summarized below in reverse chronological order.

A. Runs done in November, 1984 and May, 1985

These two beam periods were grouped together for field inhomogeneity corrections because a re-designed sample holder was used in the He cryostat for both periods. During the May, 1985 beam period, both the styrofoam and He flow cryostats were used. The relaxation rate of Mu in water ($0.236 \pm {}^{0.036}_{0.034}\ \mu s^{-1}$) in the styrofoam cryostat was measured in the more recent beam period. The intrinsic relaxation rate of muonium in water ($0.050 \pm 0.020\ \mu s^{-1}$ [59]) was subtracted from the experimental value and a value of $0.186 \pm {}^{0.056}_{0.059}\ \mu s^{-1}$ was attributed to the static field inhomogeneity. This value was used to correct for all runs performed in the styrofoam cryostat.

A series of experiments of muonium in D_2O-ice were done in different applied fields at 209 K. A plot of the muonium relaxation rate as a function of applied field strength yielded

a straight line with slope .0070 ± 0.014 μs^{-1} G^{-1} (the result for the 37 G run was not used in this calibration procedure for reasons explained in later sections). Then all runs performed in the He flow cryostat were corrected by summing the static part (obtained from the relaxation rate of muonium in water) and the field dependent part (the product of the slope and the applied field).

B. For experiments done in June, 1984

For these experiments, all the major contributors to field inhomogeneity had been removed. Relaxation rates were measured for muonium in D_2O-ice at 230 K at 10 G, 20 G, and 37 G of applied field. Since the relaxation rate of muonium at this temperature is negligible, the experimental relaxation rates were a measure of field inhomogeneity. Experiments performed at other temperatures were corrected by subtracting from the experimental relaxation rate the relaxation rate at 230 K and corresponding applied field.

C. For experiments done in May, 1984

There were only three experiments dedicated to the study of the behaviour of Mu in ice during this beam period. From results obtained by using the N_2 cryostat, the relaxation rate of Mu in

D_2O ice at 110 K was estimated to be 0.55 μs^{-1}. By plotting the experimental data of Mu at 41.4 K, a slope of 0.0092 $\mu s^{-1}G^{-1}$ - a measure of the variation of relaxation rates as a function of applied fields - was obtained. The experimental relaxation rates were assumed to take the form:

$$\lambda(exp) = \lambda_0 + \lambda_0' + \lambda(G) \qquad (7.9)$$

where λ_0 is the true relaxation rate, λ_0' is a static field inhomogeneity, and $\lambda(G)$ is a field dependent inhomogeneity. From the calculation, the value of λ_0' was estimated to be 1.49 μs^{-1} at 110 K. Since both λ_0' and $\lambda(G)$ are temperature independent, the value of λ_0 was calculated. The errors quoted for these runs were the sum of the uncertainties of the estimated relaxation rate at 110 K (± 0.1 μs^{-1}) and those of the experimental relaxation rates at 110 K. The uncertainty of $\lambda(G)$ was estimated to be small and was subsequently neglected.

D. Runs done in January, 1984

The correction for data obtained during this beam period was the most difficult to estimate since the inhomogeneity effect was not noticed until all the experiments were finished. The true relaxation rates, λ_0, in the linear region (high temperature regime) for 10 G runs were estimated from experiments performed with the nitrogen cryostat. The deviation

between the relaxation rates obtained during this beam period for 10 G experiments and the true relaxation rates (0.77 μs^{-1}) was estimated. This deviation was used to correct for lower temperature 10 G runs. The same slope, *i.e.*, 0.0092 μs^{-1} G^{-1} as obtained earlier, coupled with the deviation obtained for 10 G experiments were used to calculate the correction (0.86 ± 0.07 μs^{-1}) for 20 G applied field runs.

A summary of these corrections is given in Table VII.1.

Table VII.1

Summary of the corrections to the experimental relaxation rates made to each beam period.

All units are in μs^{-1}

	10 G	20 G	37 G
Nitrogen cryostat		$0.186 \pm {}^{0.056}_{0.054}$	
Runs done in Jan. 1984.	0.77±0.05	0.86±0.07	-------
Runs done in May 1984.	1.78±0.2	-------	2.33±0.2
Runs done in June 1984	$0.491 \pm {}^{0.027}_{0.026}$	$0.628 \pm {}^{0.033}_{0.032}$	0.783±0.025
Runs done in Nov., 1984 & Apr.,1985	$0.256 \pm {}^{0.068}_{0.068}$	$0.327 \pm {}^{0.083}_{0.081}$	$0.446 \pm {}^{0.106}_{0.104}$

VIII. Experimental results

1. Spin relaxation rates of muonium

The muonium signal in H_2O- and D_2O-ices decays as a function of time because of the spin relaxation mechanisms discussed earlier (Chapter IV). The relaxation rate of muonium increases as an inverse function of temperature because of the temperature dependent nature of the correlation time, τ_c. As an illustration, Figure VIII.1 shows the effect of temperature on the muonum signal in a single ice crystal of D_2O oriented with its c-axis parallel to the field of 37 G. It is clear from Figure VIII.1 that the muonium signal decays faster as the temperature is lowered.

The experimental relaxation rates were extracted from the spectra using either Equation 7.3 or 7.4 depending on the experimental situation as explained earlier. The θ = 55° orientation and the 37 G applied field experiments were chosen to simplify the expression used in fitting. However, the two frequency signal is preferrable at high temperatures, since any residual splitting due to an inaccurate 55° orientation or 37 G applied field strength would result in non-exponential relaxation. Below 200 K this source of error can be discounted since the natural linewidth is greater than any potential

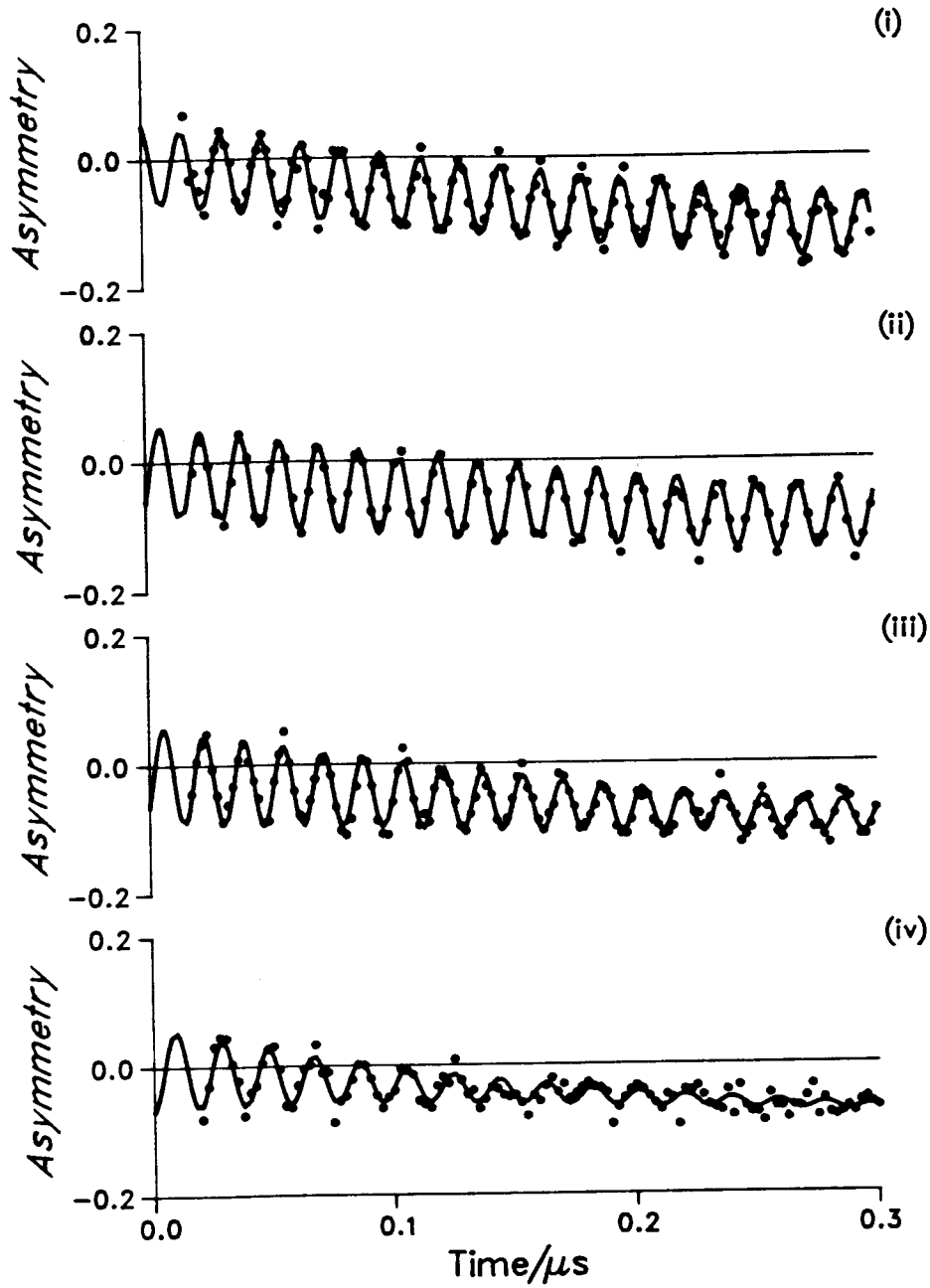

Figure VIII.1. Spectra of muonium in D_2O ice at different temperatures in an applied field of 37 G: (i)195 K. (ii)78.3 K. (iii)36.5 K. (iv)8 K.

splitting. A summary of the experimental relaxation rates is given in Appendix 1. The relaxation rates quoted in Appendix 1 have not been corrected for field inhomogeneity effects.

Figure VIII.2 and VIII.3 are plots of the corrected relaxation rates of muonium in H_2O-ice and D_2O-ice as a function of temperature respectively. The correction procedure used is that mentioned in Section VII.5. The experimental data are divided into several sets corresponding to different crystal orientations (0° and 55°) and applied field strengths (10 G, 20 G, and 37 G). No distinction is given to the results obtained from crystals I and crystals II since the experimental relaxation rates obtained from these two different crystals do not show any discrepancy.

Experiments were done to investigate the dpendence of relaxation rate as a function of the angle the *c*-axis of the crystal makes with the applied field. The crystal used was H_2O and the temperature was at 227 K. A field of 10 G was used. The results are shown in Figure VIII.4. As can be seen in Figure VIII.4, the relaxation rate of muonium is dependent on the angle the *c*-axis of the crystal makes with the applied field. The implications of this dependence will be discussed in the next chapter.

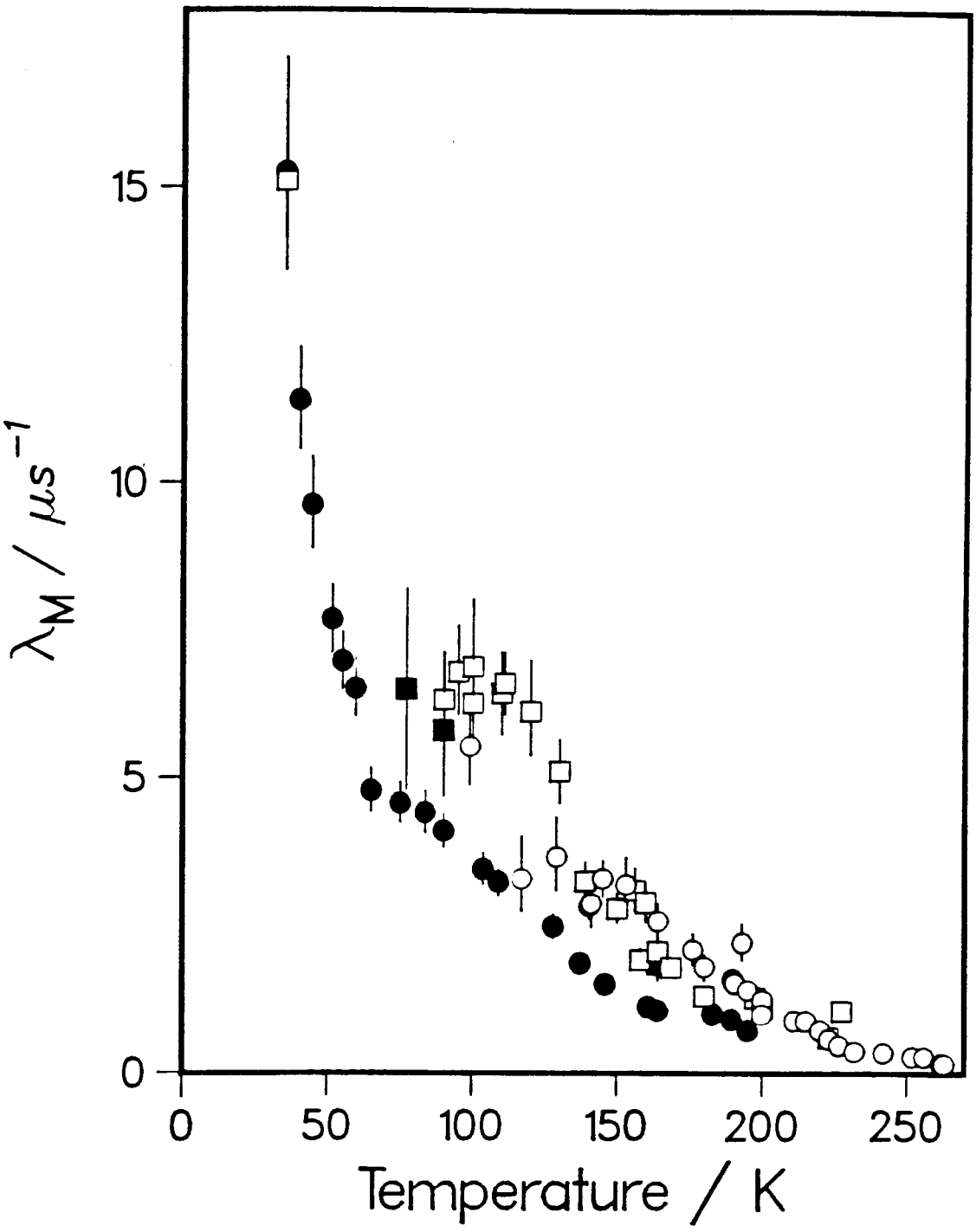

Figure VIII.2. Corrected relaxation rate of muonium in H_2O-ice as a function of temperature. (o 0° 10G, ● 0° 37G, ▫ 55° 10G, ▪ 55° 20G).

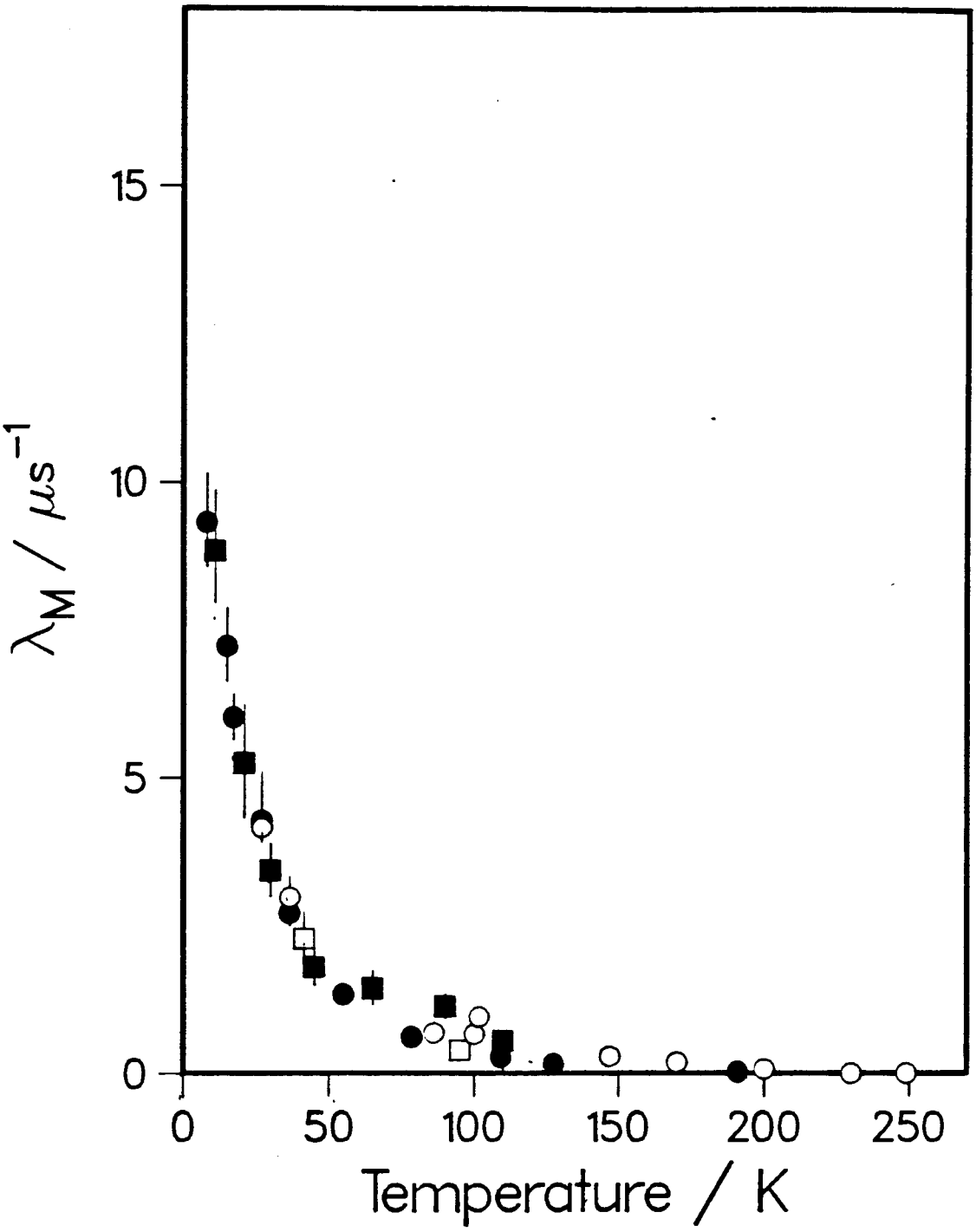

Figure VIII.3. Corrected relaxation rate of muonium in D_2O-ice as a function of temperature. (o 0° 10G, ● 0° 37G, ¤ 55° 10G, ■ 55° 20G).

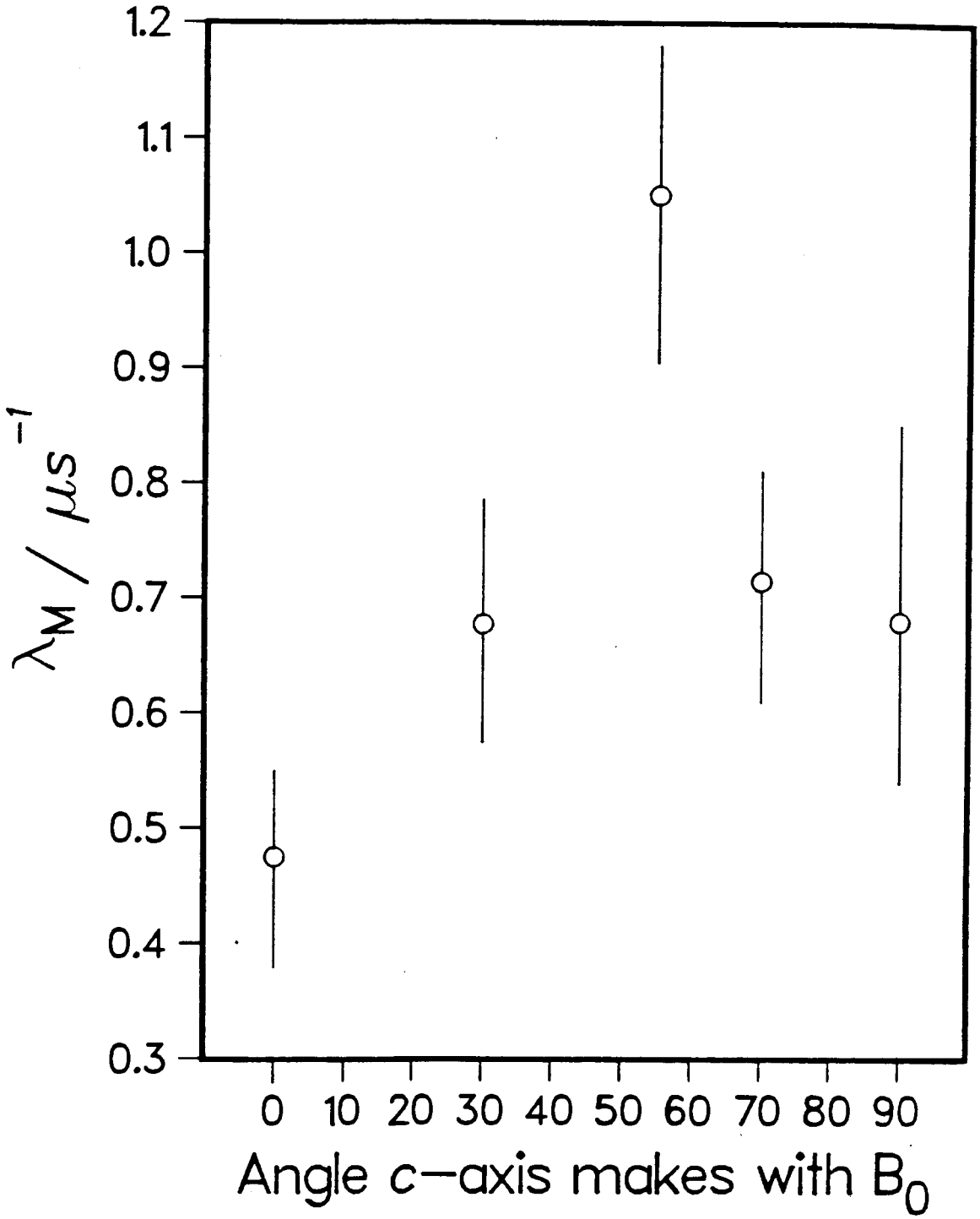

Figure VIII.4. Muonium relaxation rate as a function of orientation. The temperature was 227K. The crystal used was H_2O.

2. Asymmetries of muon and muonium

The diamagnetic fractions, P_D, determined for single crystal samples are displayed as a function of temperature in Figure VIII.5. The data are divided into two sets according to the two different methods used in growing the crystals. No distinction is given to the diamagnetic asymmetries obtained for the different orientations of the crystals with respect to the applied field since there is no disagreement between the data. This suggests that there is no dependence of P_D on the crystal orientation. The statistical errors in the P_D values are all close to 0.01. Systematic errors in calibration are potentially higher, particularly for the earlier experiments where stops in the cryostat were not taken into account. However, good agreement of the data is evident.

Muonium fractions, P_M, are displayed in Figure VIII.6 as a function of temperature. The data are separated into two groups according to the crystal orientation: $\theta = 0°$ or $55°$. There is no disagreement between the P_M values for these two orientations which in turn suggests that there is no dependence of P_M on orientation.

There is disagreement between the P_M values found for the crystal I and crystal II in the region $T > 200$ K. Difficulties have been encountered in calibrating the results. The cause of this disagreement is unclear as explained in an earlier publication [54]. Nevertheless, the trend is clear: P_M continues

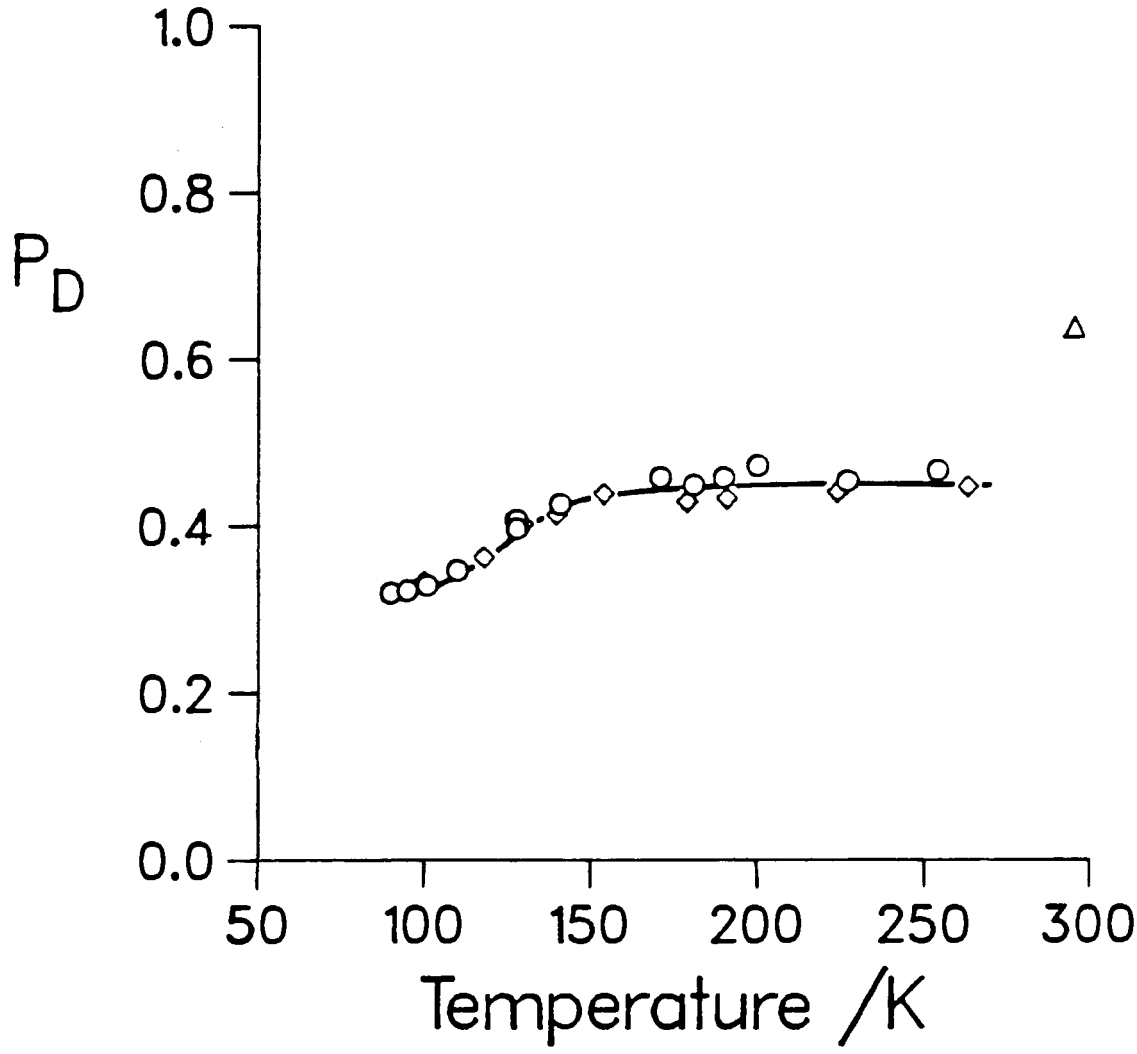

Figure VIII.5. Diamagnetic fractions in H_2O ice crystals I (◇) and II (○).

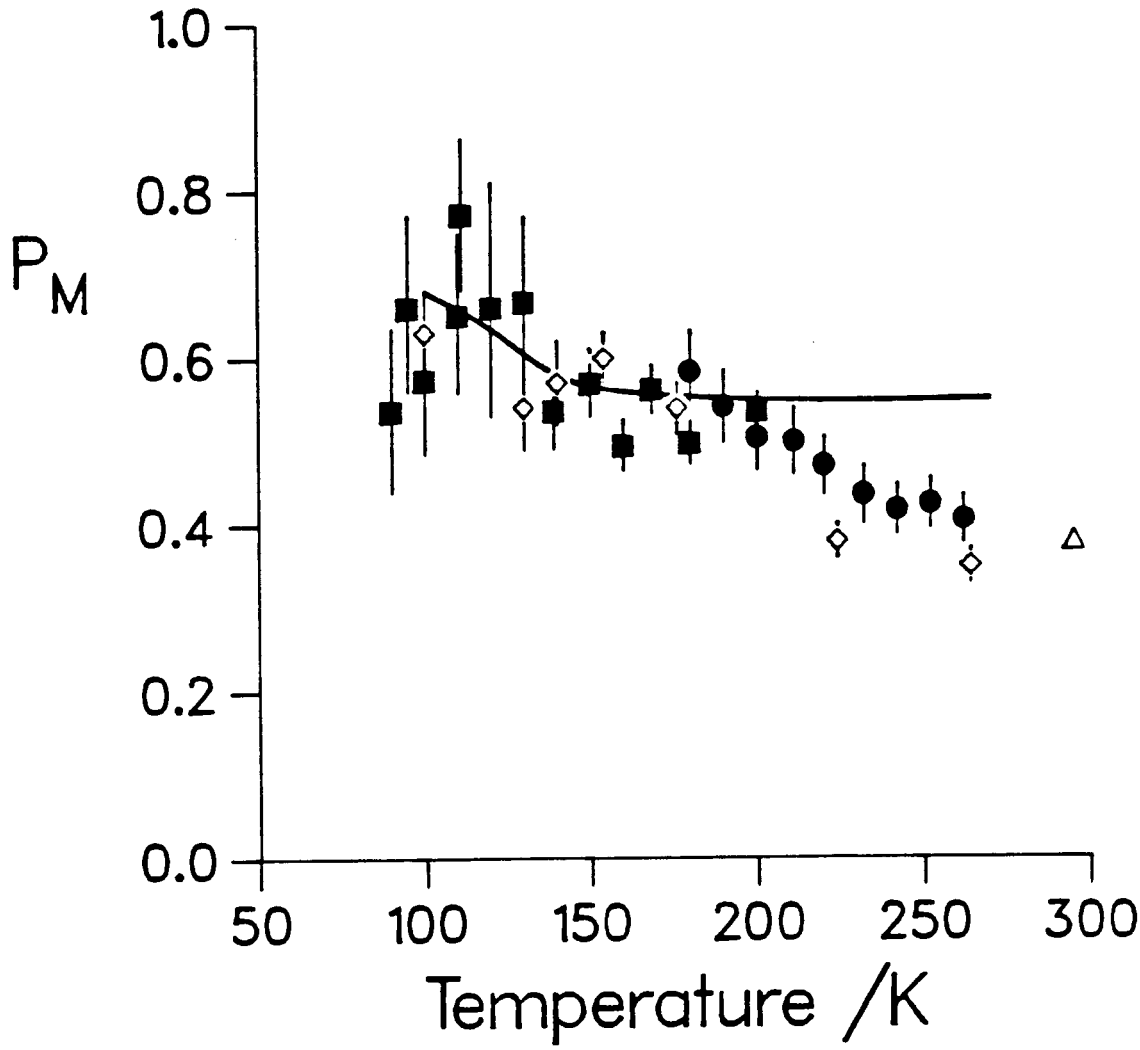

Figure VIII.6. Muonium fractions in H_2O ice crystal I with its *c*-axis at 0°(◇) to the field, and crystal II oriented at 0°(•) and 55°(■). The solid line represents $1-P_D$ for the crystals and for liquid water. The triangle is the muonium fraction in water.

to fall as the temperature is raised above 200 K.

As an aid to comparison of the diamagnetic and muonium fractions a smooth curve has been drawn through the P_D points in Figure VIII.5. It is reproduced in the form of $1 - P_D$ in Figure VIII.6. Clearly, for temperatures above 200 K P_M falls short of $1 - P_D$. Put another way, there is a missing fraction of muon polarization in ice above 200 K. A detailed explanation is beyond the scope of the present work and will not be discussed any further. Interested readers are referred to an earlier publication [54].

3. The hyperfine frequency of muonium in ice

The Larmor precession frequencies and the splittings of muonium in H_2O- and D_2O-ices have been extracted from the experimental spectra using Equation 7.4. Knowing these two parameters, the hyperfine frequency and the anisotropic splitting parameter, $\delta\omega$, can be calculated using Equations 3.23 and 3.24. Table VIII.1 is a summary of these parameters for field dependence runs. These values should be compared with the hyperfine frequency of muonium *in vacuo*, 4463 MHz G^{-1}. The hyperfine frequency of muonium in H_2O-ice is $\simeq$ 5% higher while that of muonium in D_2O-ice is marginally higher than that of muonium *in vacuo*. The implications of this will be discussed in the following chapter.

Table VIII.1

Summary of hyperfine frequency of muonium in ice

H_2O results

Temp. (K)	$\bar{\omega}$ (MHz)	Field (G)	$\delta\bar{\nu}$ (MHz)	Anisotropic splitting (MHz)	Hyperfine freq. (MHz)
190	14.376±.013	10.31	-0.942±.019	1.025±.13	4780±70
	14.277±.012	10.24	-0.935±.016		
	72.166±.008	51.75	1.197±.028		
184	13.830±.019	9.918	-0.640±.022	0.74 ±.02 †	4690±30
	28.415±.018	20.38	0.366±.026		
	71.228±.008	51.08	1.399±.024		
	100.114±.009	71.79	3.635±.018		

D_2O results

209	15.170±.003	10.88	-1.064±.005	1.172±.004	4487±12
	29.385±.007	21.07	-0.783±.009		
	72.861±.006	52.25	1.193±.019		
	101.423±.007	72.73	3.501±.015		
	143.30 ±.02	102.76	8.204±.042		
102	14.320±.007	10.27	-1.063±.010	1.17 ±.01	4503±8
	97.684±.009	70.05	3.103±.015		
	139.317±.009	99.90	7.630±.013		
36.5	101.953±.022	77.11	3.432±.051	N/A ††	4456±14
	143.36 ±.02	102.81	8.249±.030		

† The c-axis of the crystal was not parallel to the applied field.

†† The relaxation rate of muonium in ice at this temperature is high. Correlation between λ_M and δ of Equation 7.4 made the fit difficult and yielded unreliable results. Therefore, δ was fixed at the value obtained for higher temperatures.

IX. Discussion

1. Relaxation mechanism

The marked difference between results in H_2O- and D_2O-ices shows that the line-width of trapped muonium arises mostly from dipolar interactions with protons/deuterons of nearby water molecules. The smaller relaxation rate (narrower line-width) at higher temperatures means the fluctuation of the magnetic field experienced by muonium is time averaged. Two possible interpretations can be applied to this narrowing effect: One is to explain this by re-orientations of the water molecules surrounding the "trapped" muonium, and the other is to explain this by the translational diffusion of muonium.

For ice **Ih**, no phase transition has been observed below its melting point [23]. As discussed in Chapter II, re-orientation of the water molecules (measured by dielectric relaxation) is slow when compared with the time scale of the muonium spin relaxation. In fact, the motional narrowing regime of the proton NMR line-width does not begin until 230 K [86]. Shiraishi *et al* [4] explained the narrowing of the ESR line-width of hydrogen atoms by translational diffusion of the hydrogen atoms. This is particularly easy for muonium because it is nine times lighter than hydrogen. Therefore, the line-width of muonium in ice

should be attributed to dipolar broadening modulated by translational diffusion.

Second moment calculations from Chapter IV indicated that the relaxation rate of muonium in ice should be dependent on the angle the *c*-axis of the crystal makes with the applied field. The experimental results and the predictions from dipolar theory are given in Figure IX.1. The calculated results were made in the static dipolar line-width regime and have been normalized to the present data. Agreement of experimental data with static dipolar calculation is good except at 55° where the discrepancy between experimental and theoretical values is $\simeq 0.3\ \mu s^{-1}$. There is no obvious reason for this discrepancy. Nevertheless, the experimental relaxation rates of muonium in H_2O-ice showed a maximum at 55° and a minimum at 0°, in accord with predictions from dipolar calculations.

In view of this, the experimental data are divided into two sets depending on the orientations of the *c*-axis of the crystal - 0° or 55° to the applied field. The two sets of data for H_2O-ice are shown in Figure IX.2 and Figure IX.3. The D_2O-ice data are not divided into two sets because they can be distinguished easily due to the fewer number of data points available.

It was discovered that the experimental relaxation rates obtained for experiments done with the applied field set at 37 G are less than those obtained from other fields. This anomaly is probably due to the degeneracy of the two observable transitions

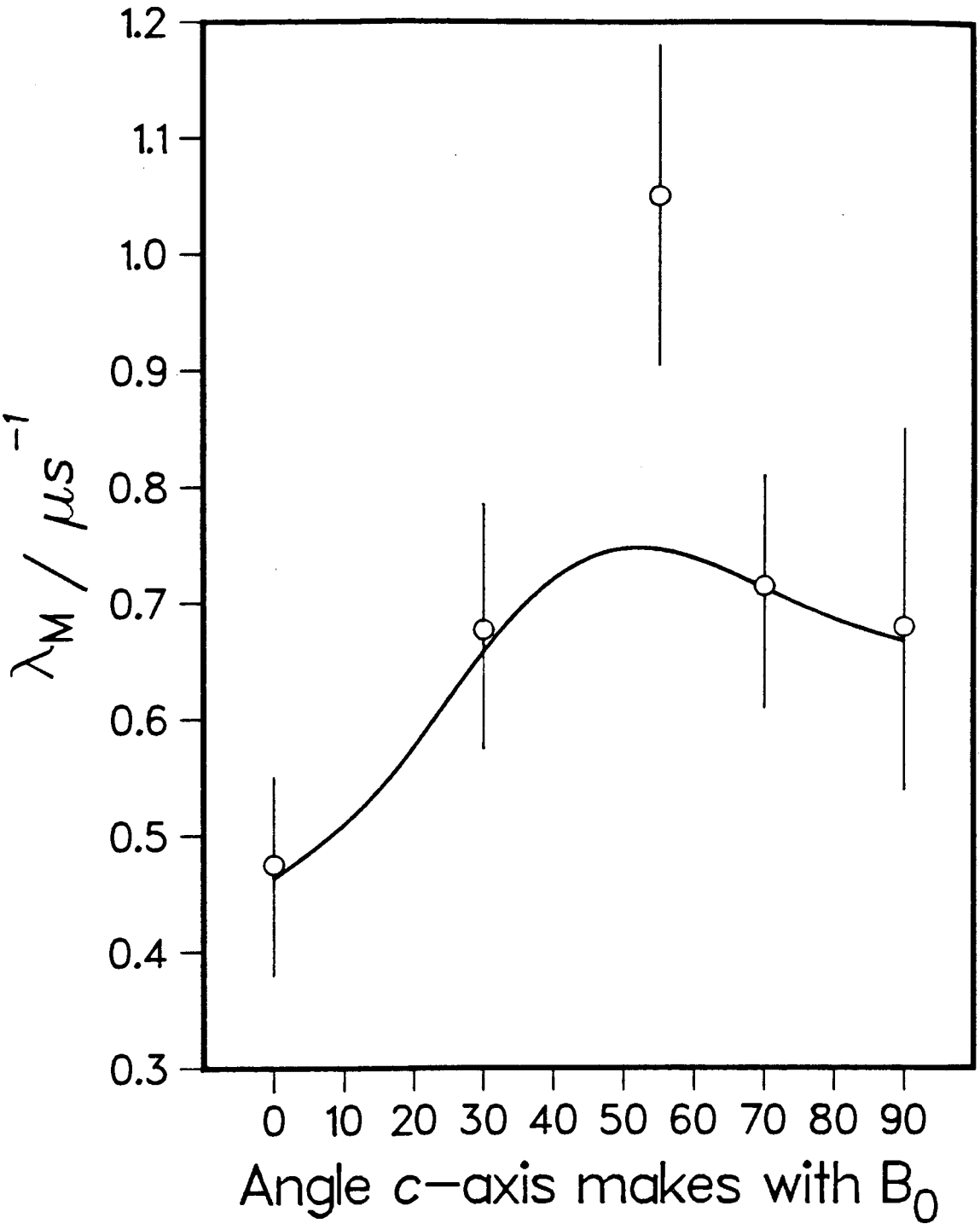

Figure IX.1. Muonium relaxation rate as a function of the angle the *c*-axis of the crystal makes with the applied field. The solid line is the normalized results from static dipolar calculation.

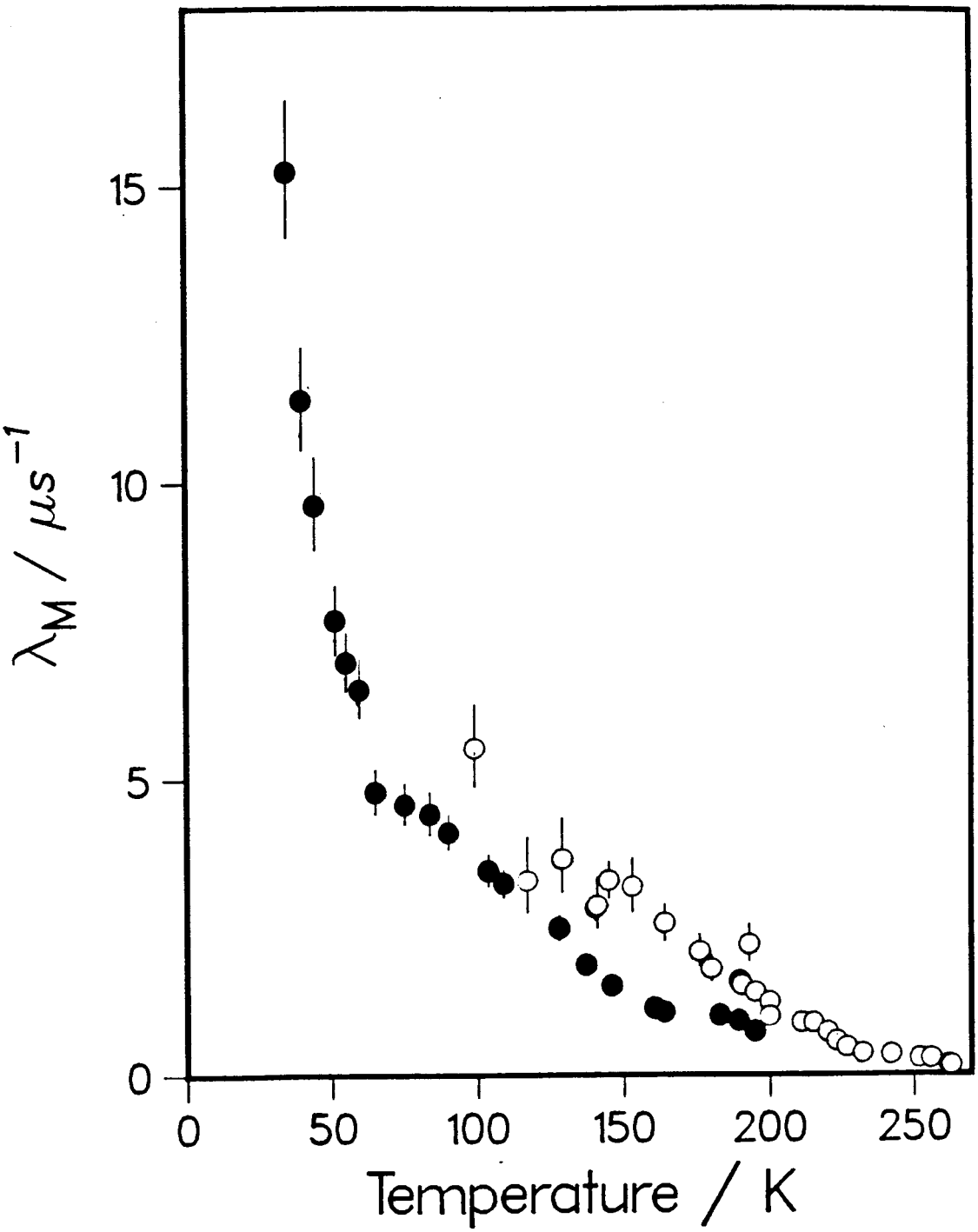

Figure IX.2. Relaxation rates of muonium in H_2O-ice at 10 G (o) and 37 G (•) oriented with its *c*-axis 0° to the applied field.

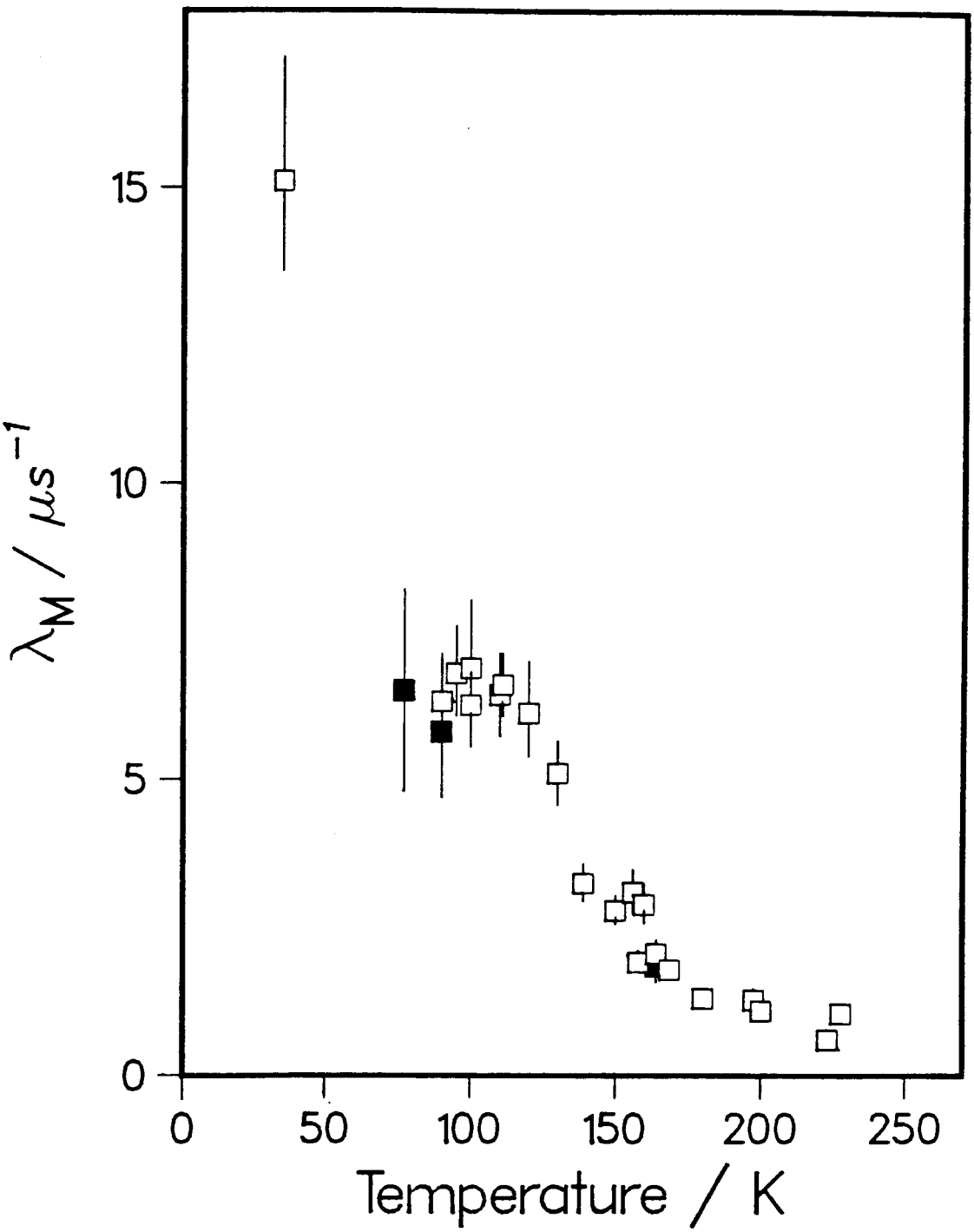

Figure IX.3. Relaxation rates of muonium in H_2O-ice at 10G (□) and 20 G (■) oriented with its *c*-axis 55° to the applied field.

at 37 G. However, a quantitative treatment of the problem is beyond the realm of the present research and is not pursued further. The set of data obtained at this field is very consistent. Therefore, it is used for later calculations. Data for both H_2O- and D_2O-ices at 37 G are shown in Figure IX.4.

The ratio of the relaxation rates for muonium in H_2O- and D_2O- ices varies with temperature. The predictions from motional narrowing for fast and slow diffusing muonium in ice are 16 and 4 respectively (Equations IV.18 and IV.19) [9]. The ratio obtained by Gurevich *et al* [9] is 2.9 at 77 K. The ratio obtained from the present data at 77 K is $\simeq$ 7.3. **It seems that muonium is still diffusing in ice at 77 K.** This negates the claim made by Gurevich *et al* that muonium does not diffuse in ice at this temperature. However, because of the limitations of the motional narrowing theory, the translational motion of muonium in ice cannot be inferred for lower temperatures by this method.

According to Slichter [87], the longest τ_c for which Equation 4.13 remains valid is when $\tau_c < T_2$. For $\tau_c > T_2$, the spins will not be dephasing by a "random" walk because dephasing occurs before there is a chance to hop. The line-width is then independent of the jump rate, resulting in the temperature independent rigid lattice line-width. In the present case, the calculated value of τ_c at the rigid lattice limit is 5.7×10^{-8} s for H_2O-ice which in turns implies that the

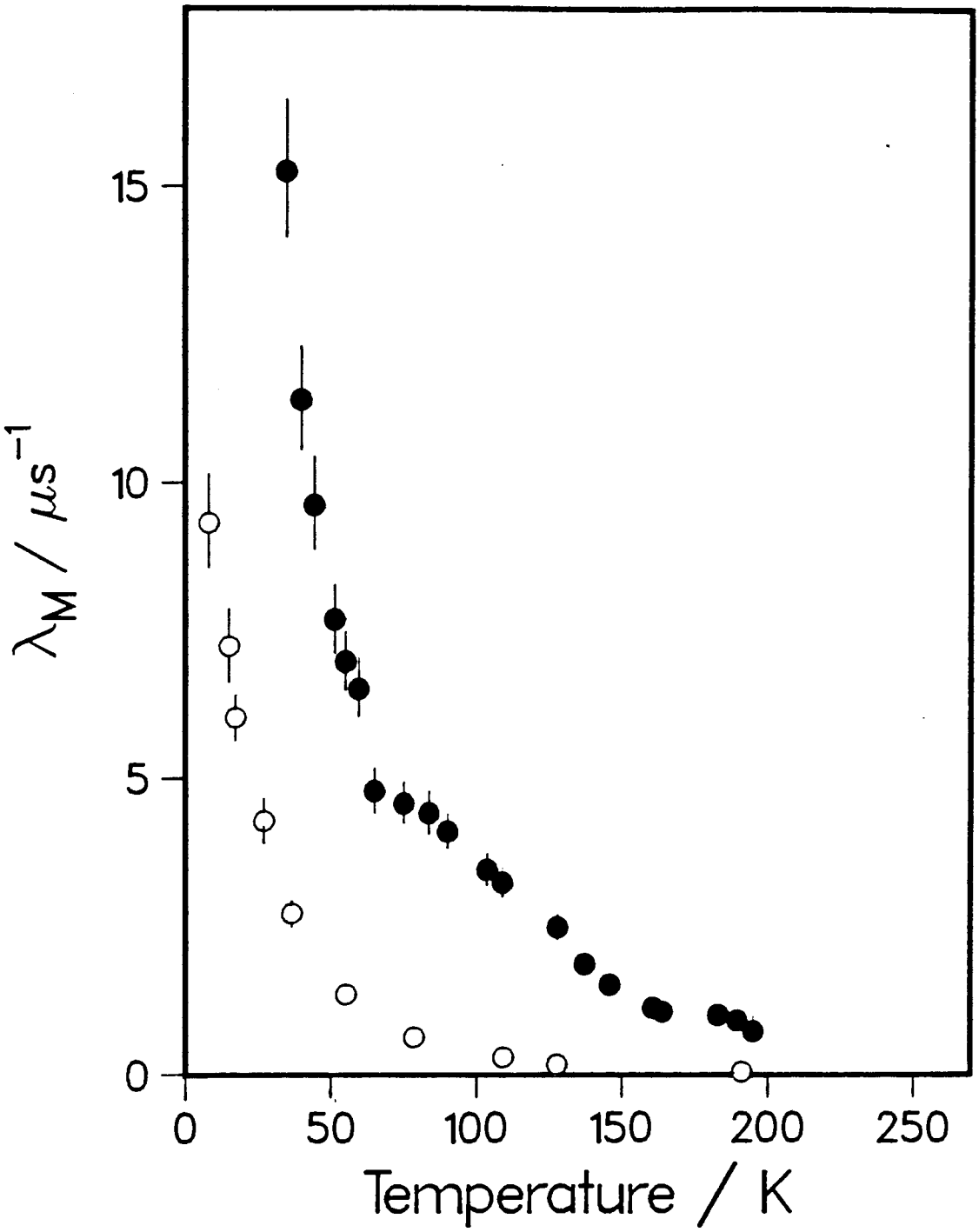

Figure IX.4. Muonium relaxation rates in H_2O- (•) and D_2O-crystals (o) oriented with their *c*-axis parallel to an applied field of 37G as a function of temperature.

relaxation rate of muonium at the limit should be $\simeq 17\ \mu s^{-1}$.[1] This relaxation rate corresponds to the experimental results in the temperature range of around 35 K. Since the theory breaks down at this value of τ, the ratio of λ_M between H_2O- and D_2O-ices at this temperature should not be taken into consideration. Furthermore, when $\tau_c \simeq T_2$, the line-shape of the relaxation function deviates from a Lorentzian. However, due to the complexity of the spectra and lack of existing theory, the experimental spectra were fitted to a Lorentzian for practical purposes.

As mentioned earlier, when $\tau_c \simeq T_2$ the transverse relaxation rate, T_2^{-1}, reaches the dipolar limit. In the motional narrowing regime, the value of λ_M is small. The intermediate range is characterized by an increase of λ_M which indicates the slowing down of muonium; and a bend-over region after which it reaches the static dipolar broadening limit. The bend-over region signifies the on-set of localization of muonium in the cavity. This has not been observed. The experimental values of T_2^{-1} for muonium in D_2O-ice well exceeds the value of $\simeq 4\ \mu s^{-1}$ obtained at the dipolar rigid lattice limit. The explanation of this is given later in Section 3. In fact, the relaxation rate of muonium in D_2O-ice is $\simeq 10\ \mu s^{-1}$ at 8 K. This means that muonium is not localized at this temperature. **Put another way, muonium is still diffusing in ice at 8 K.**

---

[1] This is probably an underestimate. See later sections for discussions.

2. Diffusion parameters

In the motional narrowing limit, the correlation time, τ_c, is the inverse of D_E. In that limit, the relaxation rate of muonium in ice is directly proportional to τ_c. If no other diffusion mechanism is present, a plot of $\ln(\lambda)$ versus $1/T$ will yield a straight line. The slope of the straight line is related to the activation energy by the Boltzmann constant. If quantum tunnelling is present, the plot will show the characteristic "bend-over" discussed in Chapter VI. The natural logarithm of the experimental relaxation rate of muonium in single crystals of ice as a function of reciprocal temperature is plotted in Figure IX.5. At around 75 K, the plot for muonium in H_2O-ice shows a "kink", *i.e.*, a dip from the expected straight line. This is thought to be the region where $\omega_M \tau_c = 1$. It is not observed for D_2O-ice because of insufficient number of data points.[2] For temperatures below 50 K, the D_2O data shows the characteristic bend-over which indicates the on-set of tunnelling. This is in accord with the prediction of the present potential that tunnelling dominates for temperatures at or below 100 K. However, the temperature where tunnelling becomes dominant is different between the experimental data and the theoretical predictions. This difference is thought to be caused

[2] Discussions on the implication of this "kink" are given in the following section.

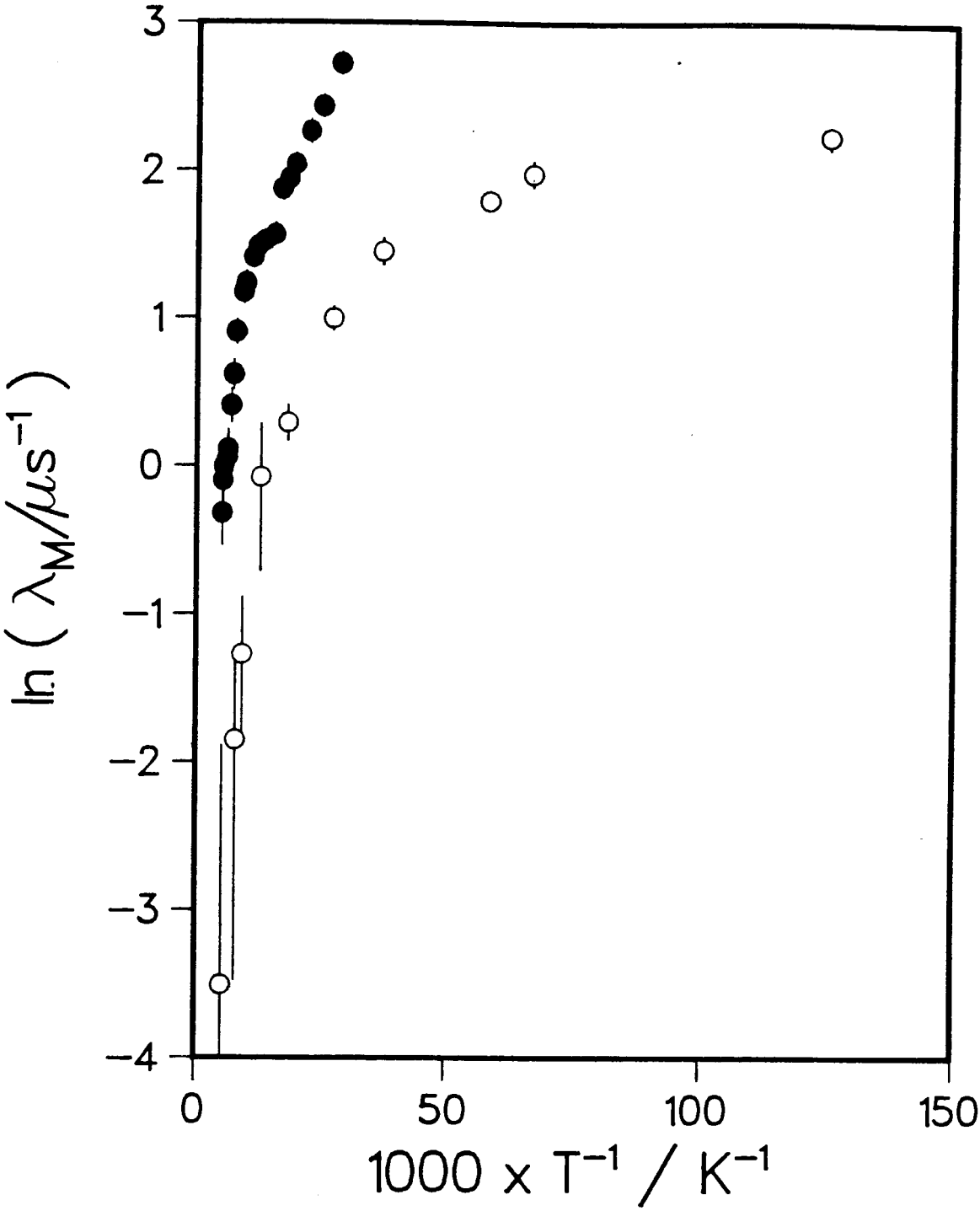

Figure IX.5. The natural logarithm of T_2^{-1} of muonium in H_2O- (•) and D_2O- (o) ices at 37 G - an Arrhenius plot.

by an overestimate of the oscillator frequency which is discussed in the following section. Experiments were not done for H_2O at these temperatures because the relaxation rates are too high to give reliable results.

The slope of the linear portion of the plot (high temperature regime) gives an effective activation energy of **40 ± 4 meV**. The calculated values from V_1 and V_3 are within experimental error. The value obtained from V_2 is about 20 % less than that of the experimental value.

Shiraishi *et al* [4] studied the spectra of hydrogen atoms in pure and acidic ices from 160 K up to the melting point. They obtained an effective activation energy of 52 meV. This value is over 20 % less than the calculated values from V_1 and V_3 but appears to agree with that calculated from V_2. However, they used polycrystalline samples. It seems that their ESR spectra could be suffering from inhomogeneous broadening. In that case, their activation energy will have to be scaled upwards and would be closer to the values predicted by V_1 and V_3. Fluornoy *et al* [3] have measured the thermal decay of trapped hydrogen atoms in pure ice between 20 and 50 K. Although the activation energy could not easily be determined because of the complexity of the decay curves, they suggested an activation energy of $\simeq$ 109 meV at 50 K. Furthermore, their results showed that diffusion is rapid above 40 K but slow below 20 K. Quantum tunnelling explains the "absence" of localization, *i.e.*, continued slow diffusion, between 50 K and 20 K. At these temperatures, the

calculated results exhibit the characteristic bend-over and reach the temperature independent diffusion rate at $\simeq$ 25 K.

3. Correlation time

The correlation time, τ_c, is the average time spent by the diffusing particle in a crystal site. It is taken as the inverse of the diffusion rate. The experimental values of the correlation function, $f(\tau_c)$:

$$f(\tau_c) = \tau_c [1 + 1/(1 + \omega^2 \tau_c^2)] \qquad (9.1)$$

were extracted from the experimental relaxation rates by dividing them by the theoretical second moment. The results for both H_2O- and D_2O-ices as a function of reciprocal temperature are plotted in Figure IX.6. Shiraishi *et al* [4] calculated the correlation times for diffusing hydrogen atoms in ice. Their data are reproduced in Figure IX.6. Compared to the present data, their results are fractionally higher. This difference between the correlation times of muonium and hydrogen atoms is expected. Since a hydrogen atom is 9 times more massive than muonium, it diffuses slower because of the inverse-root-mass dependence of the oscillator frequency and the higher activation energy.

At 75 K, there is a change of slope for the correlation function in Figure IX.6. Figure IX.7 is the same plot with log(1/T) as its x-axis to give a better view of this "kink".

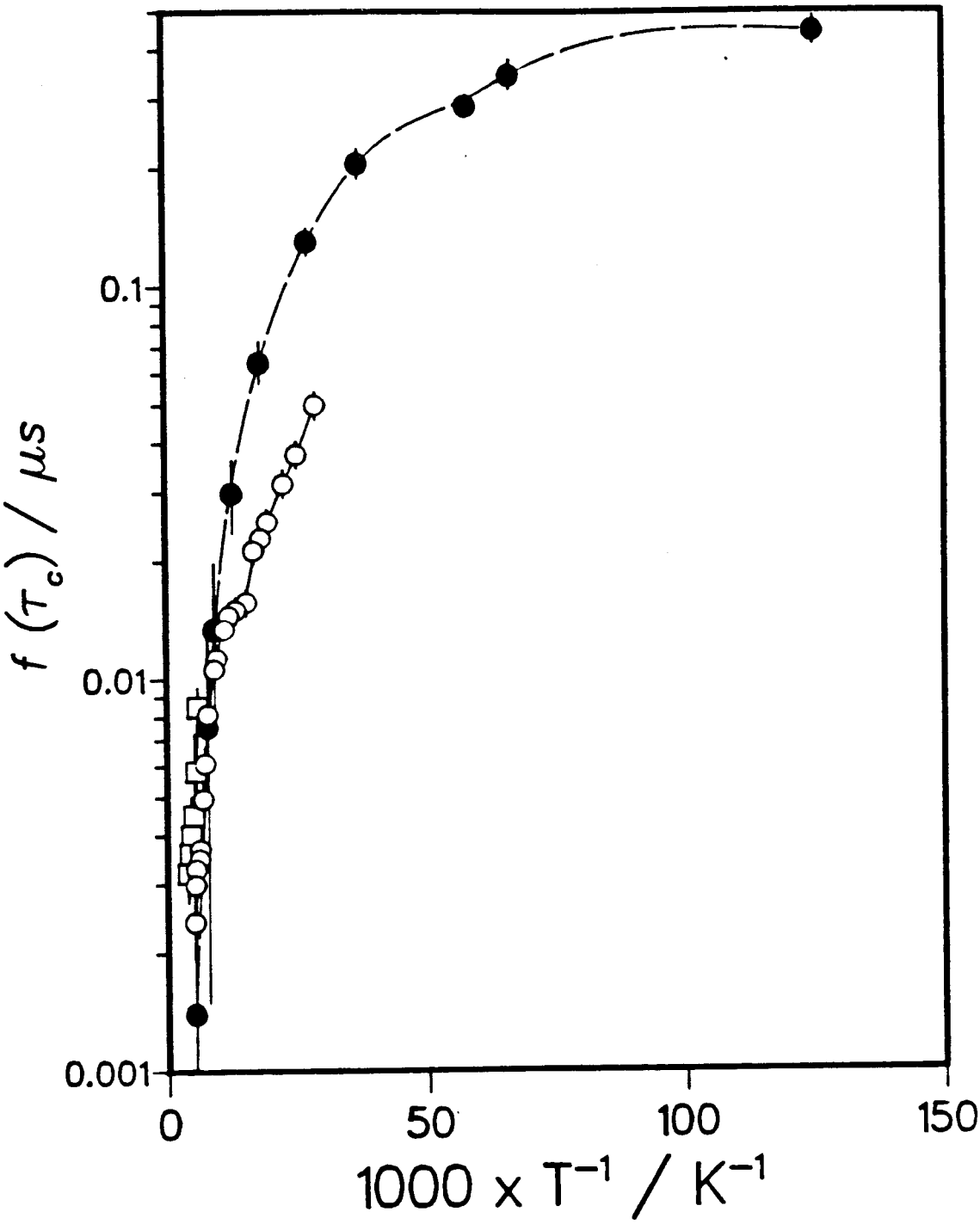

Figure IX.6. The correlation function, $f(\tau_c)$ of muonium in H_2O- (o) ices and D_2O- (•) ices as a function of reciprocal temperature. The data for hydrogen [4] are reproduced (▫).

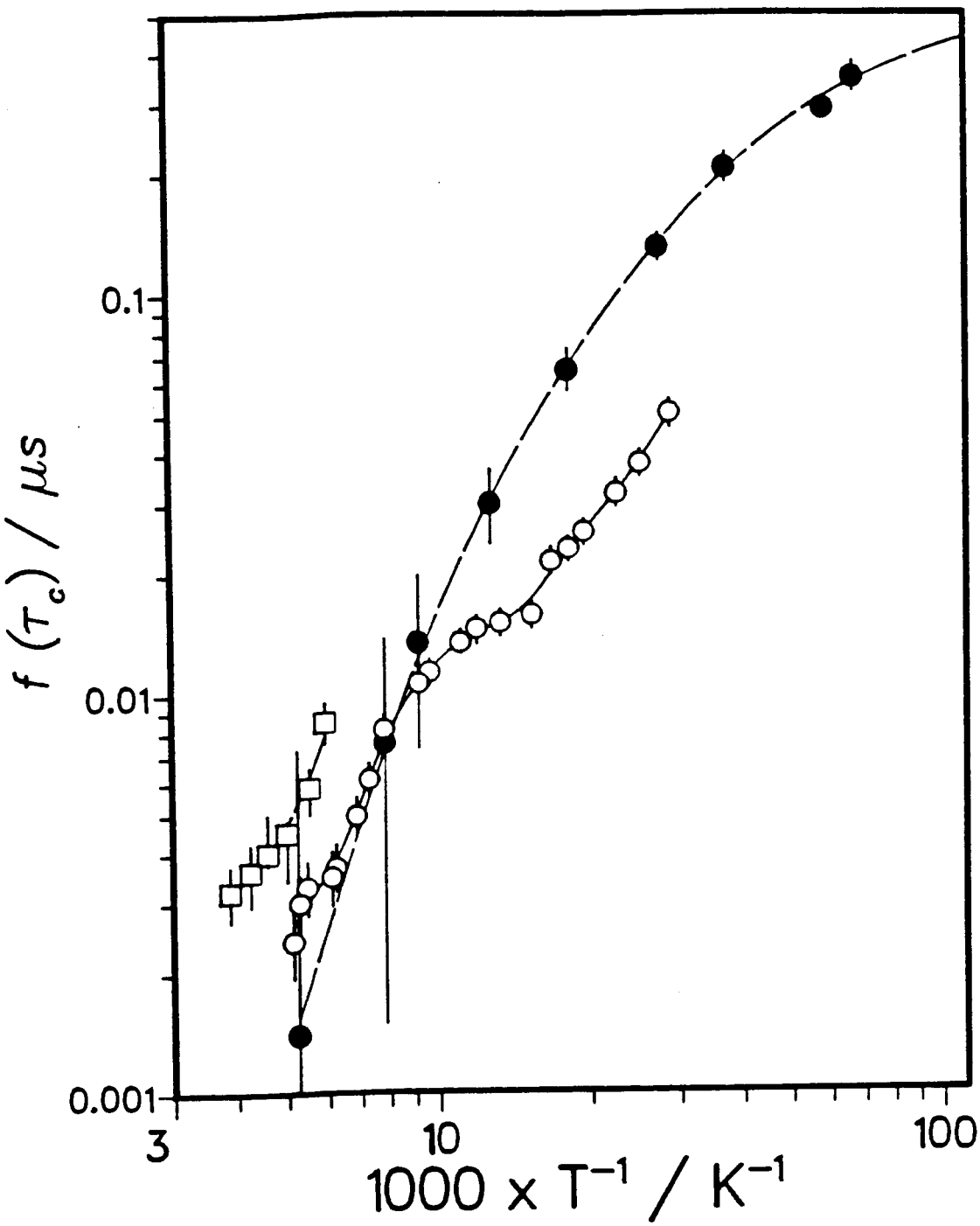

Figure IX.7. The correlation function, $f(\tau_c)$ of muonium in H_2O- (o) ices and D_2O- (•) ices as a function of reciprocal temperature. The data for hydrogen in ice [4] are reproduced (¤). The x-axis scale is logarithmic.

This effect is not observed for D_2O results because of insufficient number of data points. This kink can be explained by the condition that $\omega_M \tau_c \simeq 1$ at 75 K. T_2^{-1} is proportional to $2\tau_c$ ($\omega_M \tau_c << 1$) and τ_c ($\omega_M \tau_c >> 1$) for temperatures above and below respectively. At 37 G, ω_M is 3.25×10^8 s^{-1} which corresponds to $\tau_c = \omega^{-1} = 3.077 \times 10^{-9}$ s. At 75 K, the value of T_2^{-1} is measured to be 4.57 μs^{-1}. From these values of T_2^{-1} and τ_c, the value of the second moment, $<\Delta\omega^2>$, for muonium in H_2O-ice is calculated to be 1.5×10^{15} s^{-2}. This is higher than the value of 3.05×10^{14} s^{-2} obtained theoretically. Therefore, the correlation function shown in Figure IX.6 and IX.7 will have to be scaled downwards. From the second moment, the relaxation rate of muonium at the rigid lattice limit is calculated to be 30 μs^{-1}. The T_2^{-1} measured for muonium in H_2O-ice at 35 K is 15.7 μs^{-1}. This implies that the rigid lattice limit has not been reached at this temperature. The relaxation rate for muonium in D_2O-ice calculated in the same limit is $\simeq$ 12 μs^{-1}. At 8 K, the relaxation rate is measured to be 9.3 μs^{-1}. Since the rigid lattice line-width has not been reached, muonium is not localized in ice at these temperatures. **In other words, muonium is still diffusing in ice at 8 K.**

There is a discrepancy between the correlation times obtained for muonium in H_2O- and D_2O-ices. In the high temperature regime ($\geq$120 K), the correlation time of D_2O-ice is less than that of H_2O-ice while the opposite happens for lower temperatures. As pointed out before, the rigid lattice

line-width is reached at a higher temperature for muonium in H_2O- than for D_2O-ice. As the rigid lattice line-width is approached, the motional narrowing theory breaks down. Therefore, at lower temperatures, the D_2O results will be a better description of the correlation time, since they are farther away from the limit. At higher temperatures, the correlation times for muonium in H_2O ice are probably more reliable because the relaxation rates were determined more accurately.

The predicted variation of τ_c as a function of inverse temperature calculated from the present potentials is plotted in Figure IX.8. There are discrepancies of several orders of magnitude between the theoretical values and the experimental results. Since the activation energies obtained from the potentials are in agreement with the experimental results, the potentials used are thought to be qualitatively correct. The parameter which can cause this difference is the harmonic oscillator frequency. From Figure V.5, it can be seen that the potentials diverge significantly from the simple harmonic oscillator model. The frequency of oscillation obtained from the present H_2O data is 4.5×10^9 s^{-1}. Therefore, it is concluded that the simple harmonic oscillator can not be applied to the present potentials. However, the diffusion parameters can be obtained by working "backwards", *i.e.*, use the experimental oscillator frequency to obtain the diffusion parameter. Since the harmonic oscillator model does not apply, there is no simple

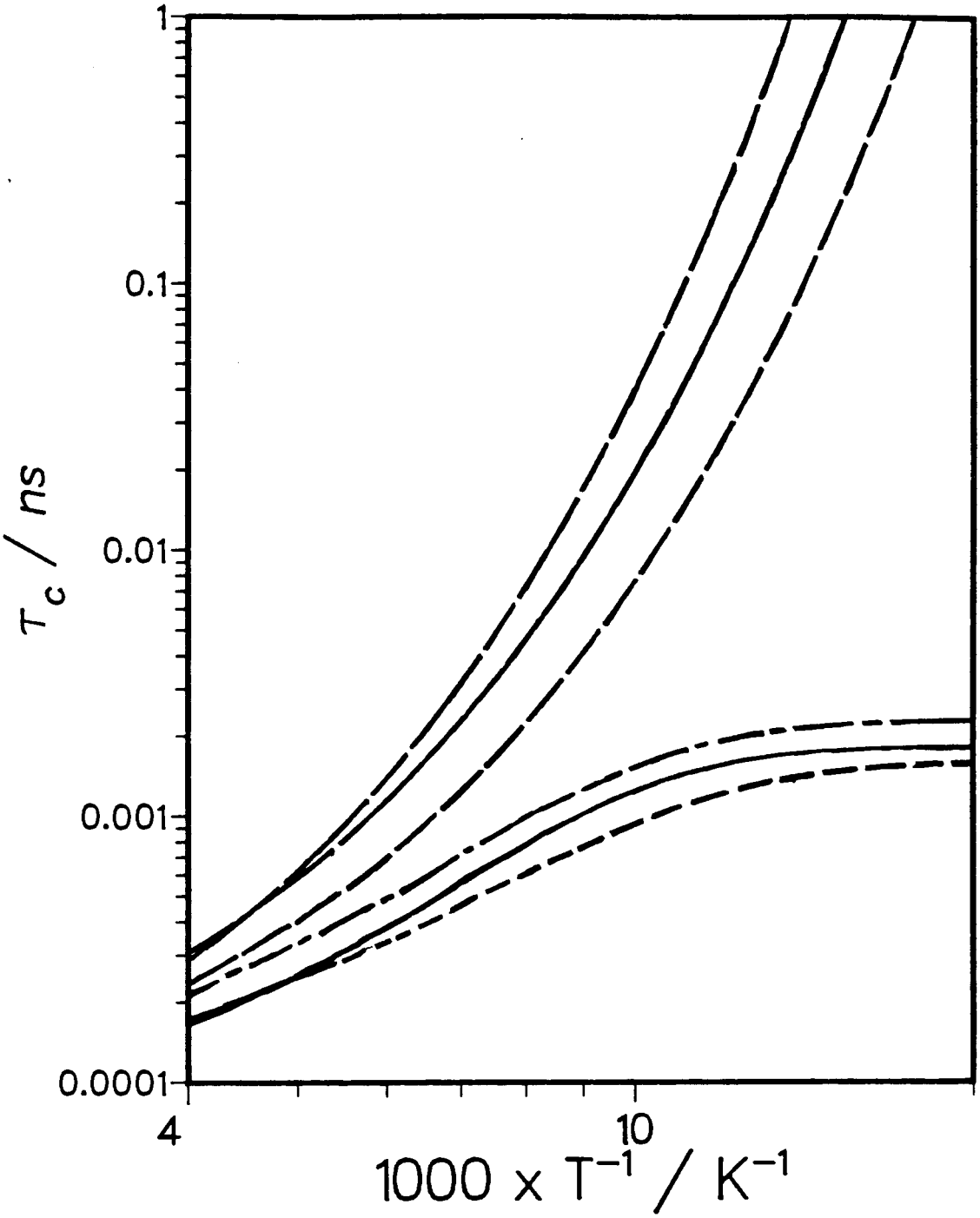

Figure IX.8. Calculated correlation time from V_1 (solid), V_2 (broken), V_3 (chain dashed) are plotted as a function of reciprocal temperature. H atom results are the top three curves while the bottom three are for muonium.

model to estimate the energy of the bound states. Nevertheless, a few features can be inferred qualitatively:

1. the energy levels of the bound particles will be lowered;
2. the activation energies for activated diffusion will be increased;
3. there will be more bound states for muonium/hydrogen in the potentials; and
4. the activated diffusion, the quantum tunnelling and the effective diffusion rates, will be lowered.

However, a thorough investigation into this problem is beyond the scope of the present study and is not attempted.

4. Hyperfine frequencies of muonium in ice

The hyperfine frequency of muonium in H_2O-ice is $\simeq$ 5% higher than the value *in vacuo* while that in D_2O is only marginally higher. These high values of hyperfine frequency for muonium in ice imply the overall interaction of muonium with the lattice nuclei is repulsive. As muonium diffuses in the lattice, its electron cloud is distorted by the environment [79]. If the surroundings exert repulsive forces on muonium, the spherical $1s$ wavefunction of muonium will be "squeezed". As a consequence, the electron density will increase at the nucleus. and the hyperfine frequency will go up. This effect has been observed for hydrogen atoms trapped in rare gas matrices [80,81,82]. An example of relevance to the present research is the hyperfine

frequency of muonium in water. This hyperfine frequency was measured recently by Percival *et al* [85] using high statistics and field variation techniques similar to the methods used here. Their results indicated that the hyperfine frequency of muonium in water is less than the value *in vacuo*. According to Klein *et al* [73], muonium is trapped in water in a clathrate cavity of radius $\simeq$ 4 Å. The intermolecular potentials used here are also applicable for muonium in water. From the present models, 4 Å corresponds to the attractive side of the potentials, and a more diffused electron cloud. Therefore, the hyperfine frequency of muonium in water will be smaller than the value *in vacuo*. The energy levels of muonium in the present calculated potentials are all positive, in agreement with the experimental findings for muonium in H_2O-ice.

The difference between the hyperfine frequencies of muonium in H_2O- and D_2O-ices may be due to the difference in amplitudes of the translational vibrations of the two isotopes in the lattice. The intermolecular potential is dependent on the distance separating the two interacting particles. The vibrational motion of the lattice nuclei will alter the shape of the potential as a function of time. The overall effect of this will be a "fuzziness" of the potential. Since vibrations are inversely proportional to the square root of mass, this "fuzziness" will be more important for H_2O-ice than for D_2O. However, the difference between the r.m.s. amplitudes of the translational vibrations for H in H_2O-ice and D in D_2O-ice is

small (≤0.02 Å) [83,84]. More theoretical studies will have to be undertaken in order to understand this effect. It is not attempted here because of the limited scope of the present research.

5. Validity of the potential functions

As discussed earlier, all three potentials give activation energies close to experimental results. It is also found that the diffusion parameters are quite insensitive to the potentials. Lengthening the *van der Waals* radii of lattice hydrogen by .3 Å (25%) only increases the activation energy by ≃8%. Although potential V_3 has a fallacious origin, because of this insensitivity it also gives results compatible with the experimental data. As for the two potentials derived in the present research, V_1 is probably closer to reality than V_2. This is because the *van der Waals* radii used were derived from SCF calculations whereas those in V_2 were from old crystallographical data of aliphatic compounds. Therefore, V_1 is considered as a closer approximation for the intermolecular potential for muonium/hydrogen in H_2O-ice. For D_2O-ice, it is suggested that the intermolecular potential be re-investigated in view of the difference between the hyperfine frequencies of muonium in H_2O- and D_2O-ices.

6. Summary and conclusions

The transverse relaxation rates of muonium in single crystals of H_2O- and D_2O-ices have been measured from 8 K up to 263 K using the standard muon spin rotation (μSR) technique at TRIUMF. The dominant relaxation mechanism was concluded to be modulation of the dipolar interaction between muonium and the lattice nuclei by diffusion of muonium along channels parallel to the *c*-axis of the crystal. Contrary to previous findings, muonium was found to be diffusing at 77 K. Furthermore, the mobility of muonium is confirmed for temperatures as low as 8 K by considering the temperature dependence of the relaxation rates in D_2O-ice. At these temperatures, it diffuses via quantum tunnelling.

Buckingham potentials were used to represent the intermolecular potential between muonium and the lattice. The *van der Waals* radius of muonium was taken to be 2.1 Å in estimating the minimum of the Buckingham potentials. Two sets of values for the *van der Waals* radii of lattice hydrogen and oxygen were used in the calculation. Both sets of values yielded positive potentials which are in agreement with the experimental findings that the hyperfine frequency of muonium in H_2O-ice is larger than the value *in vacuo* ($\simeq$ 5%). The hyperfine frequency observed for muonium in D_2O-ice is smaller than that in H_2O-ice. This implies that the intermolecular potentials may be different for muonium in H_2O- and D_2O-ices.

Calculations show that muonium diffuses preferentially along channels parallel to the *c*-axis of the crystal. It was found that the diffusion parameters are insensitive to the current potentials. Although Benderskii *et al* [17] derived their potential fallaciously, it gives compatible results because of this insensitivity. The activation energies for muonium from the two potentials were determined to be $\simeq$ 38 and 31 meV. An activation energy of 40 $\pm$ 4 meV was obtained by fitting the experimental relaxation rates to an Arrhenius equation. Curvature of the Arrhenius plot in the low temperature regime was explained by tunnelling, in accord with the prediction that the tunnelling rate exceeds activated diffusion at temperatures below 100 K. Furthermore, the effective activation energies calculated for hydrogen atom diffusion was found to be $\simeq$ 65 and 54 meV. This is also in agreement with previous findings [4].

Theoretical second moments were calculated for the rigid lattice limit. They were found to be smaller than the value obtained from experimental data. The correlation times for muonium in H_2O were found to obey the inverse-root-mass ratio when compared to results from hydrogen data obtained elsewhere [4]. The difference between the correlation times obtained for H_2O- and D_2O-ices was explained by the break-down of the motional narrowing theory. The discrepancy between the experimental correlation times and the theoretical results indicated that the simple harmonic oscillator approximation is not applicable.

In conclusion, the diffusion of muonium in ice has been fully characterized from its melting point to 8 K. It diffuses via thermal activation for temperatures above 50 K and tunnelling for temperatures below. For hydrogen atoms in ice, it is inferred that tunnelling will dominate the diffusion rate for temperatures below 20 K. From these results, the importance of this study should be clear. For a problem not attainable by conventional methods, muonium can be used as an alternative probe. Possible future studies include studies of muonium in acidic ices where different activation energies for hydrogen atoms have been observed.

APPENDIX 1

The following is a summary of the raw experimental data as obtained from analysing the experimental spectra by MINUIT. The values of λ have not been corrected for field inhomogeneity.

H_2O Results

Temp. (K)	Field (G)	Beam † Period	Orient. Deg.	Averaged λ (μs^{-1})
263	10	A	0°	$0.337 \pm {}^{0.050}_{0.047}$
262	10	B	0°	$0.348 \pm {}^{0.029}_{0.028}$
256	10	A	0°	$0.452 \pm {}^{0.067}_{0.057}$
252	10	B	0°	$0.458 \pm {}^{0.054}_{0.032}$
242	10	B	0°	$0.524 \pm {}^{0.039}_{0.037}$
232	10	B	0°	$0.546 \pm {}^{0.046}_{0.043}$
227	10	G	0°	$0.718 \pm {}^{0.036}_{0.034}$
227	10	G	55°	1.302 ± 0.067
227	10	G	90°	$0.934 \pm {}^{0.080}_{0.072}$
227	10	G	30°	$0.935 \pm {}^{0.043}_{0.040}$
227	10	G	70°	$0.971 \pm {}^{0.036}_{0.039}$
223	10	A	0°	$0.754 \pm {}^{0.077}_{0.076}$
223	10	C	55°	$1.37 \pm {}^{0.12}_{0.11}$
220	10	B	0°	$0.904 \pm {}^{0.056}_{0.054}$
211	10	B	0°	$1.068 \pm {}^{0.069}_{0.062}$
200	10	B	0°	$1.417 \pm {}^{0.088}_{0.082}$

200	10	B	55°	$1.274 \pm {}^{0.059}_{0.054}$
200	10	E	0°	$1.476 \pm {}^{0.063}_{0.061}$
197.5	10	C	55°	$2.04 \pm {}^{0.14}_{0.13}$
195	37	F	0°	1.18 ± 0.04
195	10	F	0°	$1.65 \pm {}^{0.07}_{0.06}$
193	10	A	0°	$2.39 \pm {}^{0.28}_{0.22}$
192	70	F	0°	2.03 ± 0.08
190.4	10	F	0°	$1.77 \pm {}^{0.093}_{0.084}$
190	10	B	0°	$1.74 \pm {}^{0.11}_{0.10}$
189.8	10	F	0°	1.84 ± 0.08
189.5	37	F	0°	$1.361 \pm {}^{0.039}_{0.038}$
183	37	G	0°	$1.446 \pm {}^{0.052}_{0.049}$
180	10	B	0°	$1.98 \pm {}^{0.16}_{0.15}$
180	10	E	55°	$1.49 \pm {}^{0.084}_{0.079}$
176	10	A	0°	$2.27 \pm {}^{0.22}_{0.19}$
168.5	10	A	55°	$1.97 \pm {}^{0.10}_{0.092}$
164	10	F	0°	$2.82 \pm {}^{0.12}_{0.11}$
164	10	A	55°	2.82 ± 0.18
164	20	A	55°	$2.71 \pm {}^{0.22}_{0.20}$
164	37	F	0°	1.51 ± 0.06
160.7	37	F	0°	$1.573 \pm {}^{0.047}_{0.044}$
159.8	10	A	55°	$3.65 \pm {}^{0.30}_{0.26}$
158	10	B	55°	$2.10 \pm {}^{0.13}_{0.11}$
156	10	A	55°	$3.86 \pm {}^{0.32}_{0.39}$
153	10	A	0°	$3.37 \pm {}^{0.42}_{0.37}$
150	10	B	55°	$2.97 \pm {}^{0.19}_{0.17}$

146	10	F	0°	$3.54 \pm {}^{0.24}_{0.22}$
146	37	F	0°	1.96 ± 0.06
146	70	F	0°	$2.43 \pm {}^{0.11}_{0.10}$
141	10	A	0°	$3.05 \pm {}^{0.40}_{0.32}$
140.4	10	E	0°	$3.42 \pm {}^{0.17}_{0.16}$
140.4	37	E	0°	$2.317 \pm {}^{0.070}_{0.065}$
139	10	B	55°	$3.43 \pm {}^{0.27}_{0.24}$
137.3	37	F	0°	$2.31 \pm {}^{0.075}_{0.073}$
130	10	A	55°	5.29 ± 0.48
129	10	A	0°	$3.84 \pm {}^{0.62}_{0.50}$
128	10	F	0°	$2.93 \pm {}^{0.10}_{0.09}$
120	10	B	55°	$6.30 \pm {}^{0.81}_{0.68}$
117	10	A	0°	$3.47 \pm {}^{0.67}_{0.48}$
111	10	B	55°	6.78 ± 0.47
110	10	B	55°	6.61 ± 0.64
109	37	F	0°	$3.69 \pm {}^{0.14}_{0.13}$
103.7	37	F	0°	$3.90 \pm {}^{0.16}_{0.15}$
100	10	B	55°	$6.44 \pm {}^{0.75}_{0.65}$
100	10	C	55°	$7.64 \pm {}^{1.10}_{0.86}$
99	10	A	0°	$5.71 \pm {}^{0.67}_{0.58}$
95	10	B	55°	$6.97 \pm {}^{0.74}_{0.65}$
90	10	B	55°	$6.50 \pm {}^{0.75}_{0.69}$
90	20	C	55°	$6.7 \pm {}^{1.1}_{1.0}$
90	37	F	0°	$4.55 \pm {}^{0.18}_{0.17}$
83.6	37	F	0°	$4.86 \pm {}^{0.25}_{0.24}$
77	20	C	55°	7.4 ± 1.6

75	37	F	0°	$5.02 \pm {}^{0.24}_{0.22}$
65	37	F	0°	$5.23 \pm {}^{0.27}_{0.25}$
59.5	37	F	0°	$6.96 \pm {}^{0.41}_{0.36}$
55	37	F	0°	$7.42 \pm {}^{0.39}_{0.37}$
51.3	37	F	0°	$8.13 \pm {}^{0.47}_{0.46}$
44.3	37	F	0°	$10.07 \pm {}^{0.70}_{0.64}$
39.8	37	F	0°	$11.85 \pm {}^{0.78}_{0.73}$
34.8	37	F	0°	$15.7 \pm {}^{1.1}_{1.0}$
35	10	C	55°	$15.9 \pm {}^{2.0}_{1.4}$

D_2O results

Temp. (K)	Field (G)	Beam Period	Orient. Deg.	Averaged λ (μs^{-1})
249	10	B	0°	0.133 ± 0.012
230	10	E	0°	$0.491 \pm {}^{0.027}_{0.026}$
230	20	E	0°	$0.628 \pm {}^{0.033}_{0.032}$
230	37	E	0°	0.783 ± 0.025
209	20	F	0°	$1.231 \pm {}^{0.042}_{0.039}$
209	50	F	0°	$1.449 \pm {}^{0.035}_{0.034}$
209	70	F	0°	$1.571 \pm {}^{0.043}_{0.042}$
209	100	F	0°	1.85 ± 0.11
200	10	B	0°	$0.247 \pm {}^{0.016}_{0.015}$
191	10	F	0°	$0.978 \pm {}^{0.025}_{0.024}$
191	37	F	0°	0.480 ± 0.015
170	10	B	0°	$0.372 \pm {}^{0.022}_{0.021}$

147	10	A	0°	$0.471 \pm {}^{0.044}_{0.041}$
127.6	37	F	0°	0.607 ± 0.022
110	20	D	55°	$2.23 \pm {}^{0.12}_{0.11}$
109.2	37	F	0°	$0.730 \pm {}^{0.025}_{0.024}$
101.6	10	F	0°	$1.210 \pm {}^{0.043}_{0.041}$
101.6	70	F	0°	$1.342 \pm {}^{0.043}_{0.042}$
101.6	100	F	0°	$1.813 \pm {}^{0.050}_{0.049}$
100	10	A	0°	$0.842 \pm {}^{0.052}_{0.046}$
95	10	B	55°	0.580 ± 0.090
90	20	C	55°	$1.99 \pm {}^{0.13}_{0.12}$
86	10	A	0°	$0.870 \pm {}^{0.046}_{0.043}$
78.3	37	F	0°	$1.072 \pm {}^{0.027}_{0.026}$
65	20	C	0°	$2.30 \pm {}^{0.22}_{0.20}$
55	37	F	0°	$1.709 \pm {}^{0.055}_{0.051}$
45	20	C	55°	$2.66 \pm {}^{0.25}_{0.23}$
43.2	37	E	0°	$2.883 \pm {}^{0.069}_{0.059}$
41.4	10	D	55°	$4.06 \pm {}^{0.24}_{0.22}$
41.4	70	D	55°	4.67 ± 0.15
36.5	37	F	0°	$3.18 \pm {}^{0.11}_{0.10}$
30	20	C	55°	$4.29 \pm {}^{0.38}_{0.36}$
26.9	10	F	0°	$4.77 \pm {}^{0.51}_{0.47}$
26.9	37	F	0°	$4.72 \pm {}^{0.28}_{0.25}$
26.9	70	F	0°	4.54 ± 0.21
20	20	C	55°	$6.11 \pm {}^{0.91}_{0.85}$
17.2	37	F	0°	$6.47 \pm {}^{0.28}_{0.27}$
15	37	F	0°	$7.68 \pm {}^{0.53}_{0.49}$

10.9	20	C	55°	$9.70 \pm {}^{0.95}_{0.80}$
8	37	F	0°	$9.77 \pm {}^{0.72}_{0.64}$

† (1). The beam periods are defined as follow:

A = Beam periods before or during December, 1982.

B = Beam period during September, 1983.

C = Beam period during January, 1984.

D = Beam period during May, 1984.

E = Beam period during June, 1984.

F = Beam periods after June, 1984.

G = Beam period during May, 1985 (styrofoam cryostat runs).

(2). For beam periods before 1984, only styrofoam cryostats were used. The helium cryostat was first used in January, 1984.

REFERENCES

1. R. Livingston, H. Zeldes, and E. H. Taylor, Phys. Rev., **94** (1954),725.

2. L. H. Piette, R. C. Rempel, H. E. Weaver, and J. M. Fluornoy, J. Chem. Phys., **30** (1959), 1623.

3. J. M. Fluornoy, L. H. Baum, and S. Siegel, J. Chem. Phys., **36** (1962), 2229.

4. H. Shiraishi, H. Kadoi, Y. Katsumura, Y. Tabata, and K. Oshima, J. Phys. Chem., **80** (1976), 2400.

5. R. W. Fessenden and R. H. Schuler, J. Chem. Phys., **39** (1963), 2147.

6. L. T. Muus, P. W. Atkins, K. A. McLauchlan, and J. B. Pedersen, eds., "Chemically Induced Magnetic Polarization", Reidel, Dordrecht (1977).

7. P. W. Percival, Radiochimica Acta, **26** (1979), 1.

8. A. Schenck, in "Nuclear and Particle Physics at Intermediate Energies", J. B. Warren, ed., Plenum, New York (1976).

9. I. I. Gurevich, E. A. Meleshko, I. A. Muratova, B. A. Nikol'skii, V. S. Roganov, and V. I. Selivanov, Sov. Phys. *JETP* Letts., **18** (1973), 357.

10. P. W. Percival, E. Roduner, H. Fischer, Chem. Phys., **32** (1978), 353.

11. P. W. Percival, J. C. Brodovitch, K. E. Newman, and D. P. Spencer, Chem. Phys. Letts., **93** (1982), 366.

12. J. H. Brewer, D. S. Beder, and D. P. Spencer, Phys. Rev. Letts., **42** (1979), 808.

13. J. H. Brewer, Hyperfine Interaction, **8** (1981), 375.

14. J. H. Brewer, D. P. Spencer, D. G. Fleming, and J. A. R. Coope, Hyperfine Interaction, **8** (1981),405.

15. P. Debye, "Polar Molecules", Reinhold, New York (1929).

16. D. Eisenberg and V. Kauzmann, "The Structure and Properties of Water", Oxford University Press, London (1969).

17. V. A. Benderskii, A. G. Krivenko, and A. N. Rukin, High Energy Chemistry, **14** (1980), 303.

18. K. S. E. Niblaeus, B. O. Roos, and P. E. M. Siegbahn, Chem. Phys., **25** (1977), 207.

19. F. Rinne, *Ber. Verh. Sächs Acad. Wiss.* (Math. Phys. K1), **69** (1917), 57.

20. A. St. John, Proc. natn Acad. Sci. U.S.A., **4** (1918), 193.

21. D. M. Dennison, Phys. Rev., **17** (1921), 20.

22. W. H. Bragg, Proc. Phys. Soc., **34** (1922), 98.

23. P. V. Hobbs, "Ice Physics", Clarendon Press, Oxford (1974).

24. A. Yamashita, in "Proceedings from the International Cloud Physics Conference", London (1972).

25. W. H. Barnes, Proc. R. Soc., **A125** (1929), 670.

26. (a). J. D. Bernal and R. H. Fowler, J. Chem. Phys., 1 (1933), 515.
(b). L. Pauling, J. Am. Chem. Soc., **57** (1935), 2680.

27. R. P. Auty, R. H. Cole, J. Chem. Phys., **20** (1952), 1309.

28. A. van den Beukel, Phys. Status solidi, **28** (1968), 565.

29. J. F. Nagle, J. Math. Phys., 7 (1966), 1484.

30. S. W. Peterson and H. A. Levy, Acta Crystallogr., **10** (1957), 70.

31. D. E. Barnaal and I. J. Lowe, J. Chem. Phys., **46** (1967), 4800.

32. C. A. Coulson and D. Eisenberg, Proc. R. Soc., **A291** (1966), 445.

33. A. O. Weissenberg, "Muons", Amsterdam, North Holland (1967).

34. D. C. Walker, J. Phys. Chem., **85** (1981), 3960.

35. W. Jakubetz, in "Proc. 1st. Int. Topical Meeting on Muon Spin Rotation", Rorschach (1978).

36. P. W. Percival, J. C. Brodovitch, S. K. Leung, and K. E. Newman, Hyperfine Interaction, **17-19** (1984), 543.

37. F. Bloch, Phys. Rev., **70** (1946), 460.

38. I. J. Lowe and R. E. Norberg, Phys. Rev., **107** (1957), 46.

39. C. P. Poole and H. A. Farach, "Relaxation in Magnetic

Resonance", Academic Press, New York (1971).

40. R. K. Harris, "Nuclear Magnetic Resonance Spectroscopy", Pitman, London (1983).

41. A. Abragam, "The Principles of Nuclear Magnetism", Clarendon Press, Oxford (1961).

42. A. F. Kip, "Fundamentals of Electricity and Magnetism", McGraw-Hill, New York (1962).

43. G. C. Maitland, M. Rigby, E. B. Smith, and W. E. Wakeham, "Intermolecular Forces", Clarendon Press, Oxford (1981).

44. F. Z. London, Phys. Chem., **B 11** (1930), 1812.

45. P. K. L. Drude, "The Theory of Optics", Longman, London (1933).

46. K. S. Pitzer and E. Catalano, J. Am. Chem. Soc., 78 (1956), 4844.

47. J. E. Lennard-Jones, Proc. Roy. Soc., **A106** (1924), 441.

48. R. A. Buckingham, Proc. Roy. Soc., **A168** (1938), 264.

49. D. R. Williams, L. J. Schaad, and J. N. Murrel, J. Chem. Phys., **47** (1967), 4916.

50. F. Jona and P. Scherrer, Helv. Phys. Acta, **25** (1952), 35.

51. C. Jaccard, Helv. Phys. Acta, **32** (1959), 89.

52. F. James and M. Roos, written for "Swiss Institute of Nuclear Research (SIN)".

53. R. F. Kiefl, J. B. Warren, G. M. Marshall, and C. J. Oram, J. Chem. Phys., **74** (1981), 308.

54. P. W. Percival, K. M. Adamson-Sharpe, J. C. Brodovitch, S. K. Leung, and K. E. Newman, Chem. Phys., **95** (1985), 321.

55. (a). M. Phipps and D. N. Hume, J. Chem. Educ., **45** (1968), 664.
(b). R. E. Randeau, J. Chem. Eng. Data, **11** (1966), 124.

56. J. B. Hendrickson, J. Am. Chem. Soc., **83** (1961), 4537.

57. G. G. Myasishcheva, Yu. V. Obukhov, V. S. Roganov, and V. G. Firsov, *Zh. Eksp. Teor. Fiz.*, **53** (1967), 451 [English transl. Soviet Phys JETP **26** (1968), 298].

58. W. F. Kuhs and M. Lehmann, J. Phys. Chem., **87** (1983), 4312.

59. K. Nagamine, K. Nishiyama. J. Imazato, H. Nakayama, M. Yoshida, Y. Sakai, H. Sato, and T. Tominaga, Chem. Phys. Letts., 87 (1982), 186.

60. P. Arrighini, 'Intermolecular Forces and Their Evaluation by Perturbation Theory', Springer-Verlag Berlin Heidelberg New York, 1981.

61. P. W. Atkins, 'Molecular Quantum Chemistry', second edition, Oxford University Press, Oxford, 1983.

62. V. Carravetta and E. Clementi, J. Chem. Phys., **81** (1984), 2646.

63. P. Claverie, in "Intermoleculear Interactions: From Diatomics to Biopolymers", B. Pullman ed., Wiley New York, 1978.

64. H. J. Böhm and R. Ahlrichs, J. Chem. Phys., 77 (1982), 2028.

65. J. A. Ketelaar, "Chemical Constitution", Elsevier New York, 1958.

66. W. Kolos and L. Wolniewicz, Chem. Phys. Lett., **24** (1973), 457.

67. A. Bondi, J. Phys. Chem., **68** (1964), 441.

68. R. L. Liboff, "Introductory Quantum Mechanics", Holden-Day, San Francisco, 1980.

69. I. F. Silvera, Rev. Mod. Phys., **52** (1980), 393.

70. H. H. Hyman, ed., "Noble Gas Compounds", University of Chicago Press, Chicago, 1963.

71. J. E. Huheey, "Inorganic Chemistry: Principles of Structures and Reactivity", Harper and Row, New York, 1972.

72. J. S. Tse and M. Klein, J. Phys. Chem., **87** (1983), 5055.

73. B. de Raedt, M. Sprik, and M. Klein, J. Chem. Phys., **80** (1984), 5719.

74. C. A. Wert and C. Zener, Phys. Rev., **76** (1949), 1169.

75. K. Weiser, Phys. Rev., **126** (1962), 1427.

76. R. P. Bell, "The Tunnel Effect in Chemistry", Chapman and Hall, New York, 1980.

77. W. J. Moore, "Physical Chemistry", Prentice-Hall, New Jersey, 1962.

78. M. D. Harmony, Chem. Soc. Rev., **1** (1972), 211.

79. F. J. Adrian, J. Chem. Phys., **32** (1960), 972.

80. C. K. Jen, S. N. Foner, E. L. Cochran, and V. A. Bowers, Phys. Rev., **112** (1958), 1169.

81. S. N. Foner, E. L. Cochran, V. A. Bowers, and C. K. Jen, J. Chem. Phys., **32** (1960),963.

82. E. L. Cochran, V. A. Bowers, S. N. Foner, and C. K. Jen, Phys. Rev. Letts., **2** (1959), 43.

83. A. Zajec, J. Chem. Phys., **29** (1958), 1324.

84. A. J. Leadbetter, Proc. R. Soc., A**287** (1965), 403.

85. P. W. Percival *et al*, unpublished results.

86. K. Kume, J. Phys. Soc. Jpn., **15** (1960), 1493.

87. C. P. Slichter, "Principles of Magnetic Resonance", Harper and Row, New York, 1963.

88. R. J. Le Roy, K. A. Quickert, and D. J. Le Roy, Trans. Faraday Soc., **66** (1970), 2997.